
Ground-based remote sensing of optically thin ice clouds

Petra Hausmann



Munich 2012

Ground-based remote sensing of optically thin ice clouds

Petra Hausmann

**Master Thesis
Faculty of Physics
Ludwig-Maximilians-Universität
Munich**

**Supervisor: Dr. Tobias Zinner
Second Supervisor: Prof. Dr. Bernhard Mayer**

**submitted by
Petra Hausmann**

Munich, December 5, 2012

Abstract

The representation of clouds and their feedbacks on climate change remain the largest uncertainties in climate prediction. Ice clouds play an important, but not completely known role in the Earth's radiation budget. The low optical thickness of cirrus clouds and their complex microphysics, especially the highly variable ice crystal shape, present a challenging task in cloud remote sensing. For a better understanding of the ice cloud radiative impact, more realistic representations in climate models and accurate cloud property retrievals are necessary.

In this study, a new method is introduced to derive optical thickness and effective particle size of optically thin ice clouds from ground-based transmittance measurements. The retrieval relies on the spectral slope of transmittances in 485 - 560 nm, the cloud transmittance at a visible wavelength (550 nm), and a shortwave infrared wavelength (1600 nm). The dual-wavelength technique, commonly used for reflectance-based cloud property retrievals, does not allow for an unambiguous mapping of optical thickness to transmittances. Using the visible spectral slope as third dimension in the lookup table allows for resolving this ambiguity. The lookup tables are the result of extensive radiative transfer simulations applying the software package libRadtran assuming a plane-parallel 1D atmosphere and a typical ice crystal habit mixture.

The proposed retrieval is based on the spectral capabilities of the newly established hyperspectral imaging spectrometer specMACS. It is part of the Munich Aerosol and Cloud Scanner at the Meteorological Institute Munich (MIM) and provides continuous spectral radiance measurements in the range of 400 - 2500 nm. Deploying specMACS in a zenith-looking setup at MIM and at Mount Zugspitze, first transmittance measurements are obtained, which are analyzed with the developed cirrus cloud retrieval method.

The performance of this retrieval method is demonstrated in various sensitivity studies with a vast set of synthetic observations. Major uncertainties are caused by the habit mixture assumption, the applied interpolation techniques, and the aerosol concentration. The retrieval is applicable to cloud optical thickness of 0.2 - 20, effective radius values of 5 - 90 μm and scattering angles (27° - 42° , 50° - 75°) excluding the halo regions. Further efforts have to be made to validate the retrieval results, e.g. with in-situ measurements or satellite retrievals and to provide a more accurate calibration (compared to the current factory calibration). A future exploitation of the full spectral information of specMACS will possibly allow for the retrieval of ice crystal shape, which would reduce retrieval uncertainties significantly.

Contents

1	Introduction	1
2	Theory	4
2.1	Microphysics of cold clouds	4
2.1.1	Thermodynamics of cloud formation	4
2.1.2	Ice particle nucleation	6
2.1.3	Ice crystal growth and ice enhancement	10
2.1.4	Microphysical properties of cirrus clouds	12
2.2	Radiation in the Atmosphere	17
2.2.1	Definition of radiation quantities	17
2.2.2	Interaction of radiation and the atmosphere	19
2.2.3	Radiative transfer equation	28
3	Methods	30
3.1	Hyperspectral imaging spectrometer	30
3.2	Radiative transfer simulation	33
3.2.1	Radiative transfer model	33
3.2.2	Parameterization of ice clouds	34

4	Retrieval development	37
4.1	Simulation of ice cloud transmittance	37
4.1.1	Lookup table generation	37
4.1.2	Simulated transmittance spectra	41
4.2	Retrieval of cloud phase	42
4.3	Retrieval of cloud optical thickness and effective radius	43
5	Applications	49
5.1	Sensitivity studies with synthetic observations	49
5.2	Ground-based measurements using specMACS	61
5.2.1	Measurements at MIM rooftop (Munich)	61
5.2.2	Measurements at UFS (Zugspitze)	65
6	Discussion and outlook	68
	Bibliography	77

Chapter 1

Introduction

“Cirrus clouds are crucially important to global radiative processes and the thermal balance of the Earth; they allow solar heating while reducing infrared radiation cooling to space. Models of climate changes must correctly simulate these clouds to properly account for radiometric effects in the Earth’s energy budget.” (Wylie et al., 1994)

In general, clouds play an important role in our Earth’s energy balance as they interact with solar and terrestrial radiation. The most recent assessment report of the Intergovernmental Panel on Climate Change (IPCC, 2007) states that cloud feedbacks on climate change and aerosol-cloud interactions remain the largest uncertainties in climate prediction. The particular importance of ice clouds in the climate system has been recognized for a long time (Liou, 1986; Stephens et al., 1990), but the coupling between cirrus clouds and the Earth’s radiation budget is still poorly understood (Baran, 2012).

Cirrus clouds are usually optically thin clouds in the upper troposphere composed of ice crystals of various complex shapes. Satellite observations reveal that cirrus clouds cover on average about 20% of the mid-latitude regions (Liou, 1986; Sassen et al., 2008) and more than 50% of the tropics (Wylie et al., 1994). They reflect a part of the incoming solar radiation, which is referred to as solar albedo effect. At the same time these clouds effectively trap a part of the thermal infrared radiation emitted from the Earth’s surface and the lower atmosphere, i.e. the infrared greenhouse effect. The relative contribution of these two competing effects to the net radiative forcing of cirrus clouds is determined by their scattering and absorption characteristics described by the radiative properties of the cloud (Liou, 1986). The net radiative forcing of thin cirrus clouds is expected to be positive, implying a net gain of energy in the atmosphere (Hartmann et al., 1992). For the formation of cirrus, ice nucleation particles are needed, which are a subset of atmospheric aerosol particles meeting certain requirements. The abundance of these particles can alter the cloud albedo effect (Twomey, 1977) and the cloud lifetime (Albrecht, 1989), two examples for indirect aerosol effects. Furthermore, cirrus clouds may be induced by aircraft exhausts and develop from lineshaped contrails to widespread contrail cirrus, which contribute to anthropogenic climate change (e.g. Schumann, 2005). Over central Europe, contrail cirrus coverage reaches up to 10%. The net radiative forcing by contrails and contrail cirrus is estimated to values larger than 0.3 Wm^{-2} over central Europe and to values of 0.0375 Wm^{-2}

on global average (Burkhardt and Kärcher, 2011). This value is small compared to the radiative forcing of $1.66 \pm 0.17 \text{ Wm}^{-2}$ due to the increase in CO_2 concentration since 1750 (IPCC, 2007). Consequently, the radiative forcing by contrails plays a minor role in global climate, but may influence the local climate significantly.

Numerous studies of global circulation models reveal the importance of cirrus clouds in the Earth-atmosphere radiation balance. However, such studies have also demonstrated large uncertainties in the predicted net radiative effect of cirrus clouds (Baran, 2012). For a better understanding of their radiative feedback and a more realistic representation in climate models, accurate ice cloud property retrievals are important (Comstock et al., 2007). The cloud properties required to describe the cloud radiative impact are the effective particle size, i.e. the area weighted mean particle diameter, and the optical thickness, which is a measure for attenuation in the cloud (Baran, 2012). These radiative properties are determined by the ice cloud microphysical properties, such as particle size, shape, and ice water content.

The complexity of microphysical properties, especially of ice crystal shape, and their high spatial and temporal variability present a challenging task in cloud remote sensing. Additionally, remote sensing of ice clouds is complicated by their low optical thickness, which is usually smaller than 5 (Kokhanovsky, 2004). Compared to optically thick clouds, the detection of ice clouds from space is difficult as they reflect only small amounts of solar radiation and only slightly influence thermal radiation. Due to the transparency of optically thin cirrus clouds, their detectability strongly relies on information about the surface albedo and surface emission, especially for satellite based methods (Bugliaro et al., 2012). An example of a cirrus detection algorithm is MeCiDA, which uses the thermal channels of the Spinning Enhanced Visible and Infra-Red Imager (SEVIRI) aboard the geostationary Meteosat Second Generation (Krebs et al., 2007; Ewald et al., 2012). Significant progress in spaceborne cirrus cloud observation has been achieved with the launch of the CloudSat and CALIPSO satellites, which support active remote sensing with radar and lidar and provide detailed profiles of optical properties, especially for cirrus clouds (Sassen et al., 2008). Nonetheless, these two active sensors are limited in their spatial coverage and temporal resolution due to their polar orbit with a repeat cycle of 16 days.

The common retrieval technique to derive effective radius and cloud optical thickness from passive spaceborne measurements uses solar radiation reflected by clouds at two wavelengths (Nakajima and King, 1990). In particular, this approach has been adapted to retrieve ice cloud properties from reflected solar radiation (e.g. King et al., 2004, Eichler et al., 2009). While significant progress in microphysical retrieval algorithms for ice clouds is evident, difficulties remain in characterizing crystal shapes in ice clouds. As only very limited methods for shape determination exist up to now, each ice cloud retrieval is based on assumptions about ice particle shape (Comstock et al., 2007). These assumptions introduce a major uncertainty in ice cloud property retrievals (e.g. Key et al., 2002, Eichler et al., 2009). A recently proposed cirrus retrieval (Kox et al., 2012, in preparation) is based on a neural network combining the global overview of SEVIRI and the high sensitivity to cirrus of the polarization lidar on CALIPSO, which is able to detect clouds with an optical thickness as low as 0.01.

In general, satellite observations have many advantages, such as their global coverage, but they suffer from several uncertainties in quantifying cloud features due to their limited spatial (hundreds of meters to kilometers) and temporal resolution (several minutes to days). More detailed

ground-based cloud remote sensing can be used to verify and improve cloud retrievals which are based on satellite data. Several ground-based techniques exist for the retrieval of cirrus properties using active remote sensing (e.g. Wang, 2002, Szyrmer et al., 2012) as well as passive remote sensing instruments. For example, Barnard et al. (2008) used shortwave broadband irradiances to retrieve ice cloud optical thickness in the range 0.1 - 5. An intercomparison of several ice cloud retrieval algorithms is given in Comstock et al. (2007).

In recent years, hyperspectral instruments have become applicable to atmospheric science and few approaches exist to exploit these novel possibilities in cloud remote sensing. An example for an operational hyperspectral sensor is the Solar Spectral Flux Radiometer SSFR (Pilewskie et al., 2003). For ground-based SSFR measurements, McBride et al. (2011, 2012) presented a method to derive optical thickness and effective radius of liquid water clouds with optical thickness ranging from 5 to 100. The lower limit was chosen due to a decreased sensitivity to effective radius for thin clouds. In contrast to reflectance-based retrievals, there is no unambiguous mapping between transmittance and optical thickness, as transmittances first increase with optical thickness and then decrease if optical thickness exceeds a critical value. McBride et al. (2011) resolved this ambiguity in a transmittance-based retrieval by using the transmittance at a visible wavelength and the spectral slope in the near infrared. Another hyperspectral instrument is the Spectral Modular Airborne Radiation measurement sysTEM (SMART), which was used, for example, by Eichler et al. (2009) to retrieve properties of cirrus clouds with an optical thickness range of 0.1 - 8 from reflected radiances. Hirsch et al. (2012) derive properties of thin water clouds with a lower optical thickness limit of 0.01 from thermal infrared radiances measured with a ground-based hyperspectral radiometer.

A new ground-based remote sensing system is established at the Meteorological Institute of the Ludwig-Maximilians-Universität, Munich. The Munich Aerosol Cloud Scanner (MACS) facilitates a unique combination of passive and active sensors, mainly intended for cloud side remote sensing (Zinner et al., 2008) and observation of cloud-aerosol interactions. A central component of MACS is the hyperspectral imaging spectrometer specMACS providing continuous spectral radiance measurements in the wavelength range 400 - 2500 nm. Additionally, MACS includes a recently installed cloud radar and several long established Lidar instruments. Within the scope of this thesis, the newly established instrument specMACS is deployed for ground-based remote sensing of ice clouds. A new retrieval concept based on the spectral capabilities of specMACS is developed to derive radiative properties of optically thin ice clouds from transmission measurements. The proposed method resolves the above mentioned ambiguity in the relation of transmittance and optical thickness by using the spectral slope in the visible spectrum. The uncertainties of the retrieval are revealed in several sensitivity studies using synthetic observations. In a final step, the retrieval is applied to first ice cloud transmission data, measured with the spectrometer specMACS.

The underlying theory of ice cloud microphysics and radiation in the atmosphere is introduced in section 2. Subsequently, the instrument characteristics of specMACS and the applied methods for radiative transfer simulations are described in section 3. Based on these simulations, a retrieval of cirrus cloud properties is developed in section 4. The uncertainties of the proposed retrieval method are investigated and it is applied to two exemplary specMACS measurements in section 5. Finally, a short summary and outlook to future work is given in section 6.

Chapter 2

Theory

2.1 Microphysics of cold clouds

Microphysical properties of clouds determine their interactions with radiation in the atmosphere and therefore their influence on climate, i.e. the cloud radiative forcing. The presence of aerosols can alter cloud microphysical properties by various indirect aerosol effects. Certain aerosol species initiate nucleation of ice crystals in cold clouds which exhibit especially complex microphysical properties. This complexity of cold cloud microphysics presents a challenge in the determination of their climate impact which still is a topic of current research.

In this section, the basic laws of cloud formation and cloud particle nucleation are introduced mainly following the explanations in Wallace and Hobbs (2006) and Rogers and Yau (1989). The focus is laid on the physics of *cold clouds* which are investigated in this study. In contrast to warm clouds, cold clouds extend to altitudes exhibiting temperatures below 0°C. Cold clouds may entirely consist of ice particles (glaciated cloud) or contain both ice crystals and supercooled water droplets (mixed phase cloud).

2.1.1 Thermodynamics of cloud formation

Water vapor in the atmosphere is the major constituent for cloud formation. The interrelation of water vapor pressure, water vapor density and temperature is described by the *ideal gas law*, which can be applied to each gaseous component of air individually. Therefore, the partial pressure of water vapor in the atmosphere can be expressed as

$$e = \rho_v R_v T \tag{2.1}$$

where ρ_v is the water vapor density, $R_v = 461.51 \text{ JK}^{-1}\text{kg}^{-1}$ the ideal gas constant for water vapor and T its absolute temperature in Kelvin.

The amount of water vapor in a volume of moist air is described by the relative humidity RH . With respect to liquid water the relative humidity is defined as

$$RH = \frac{e}{e_s} 100\% \quad (2.2)$$

with the water vapor pressure e in the air and the saturation vapor pressure e_s defined below.

If the relative humidity of an air parcel equals 100%, its water vapor is saturated. Under this condition the rate of condensation equals the rate of evaporation over a plane surface of pure water at temperature T . The resulting equilibrium water vapor pressure defines the *saturation vapor pressure* e_s . If the water vapor pressure exceeds the saturation pressure, the condensation rate will increase to reduce the water vapor pressure until reaching equilibrium again. Supersaturation is defined as the excess of relative humidity over the equilibrium value of 100%.

Similar to the saturation pressure with respect to liquid water, one can define a saturation pressure with respect to ice e_{si} . In this case, the deposition rate equals the sublimation rate over a plane surface of pure ice. As the bonding of molecules in ice is stronger than in liquid water, the saturation pressure with respect to water is larger than with respect to ice for any given temperature: $e_s(T) > e_{si}(T)$.

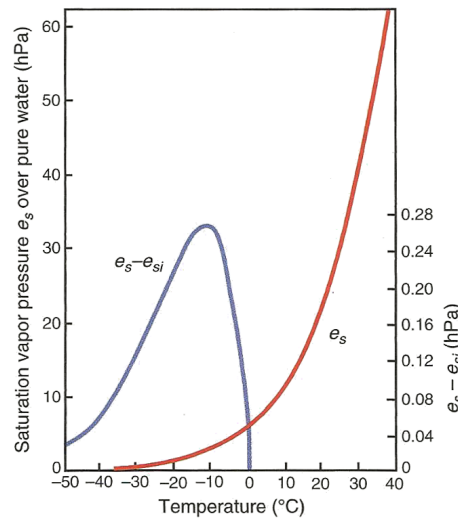


Figure 2.1: Saturation vapor pressure e_s with respect to liquid water as a function of temperature (red) and the difference between $e_s(T)$ and saturation pressure with respect to ice $e_{si}(T)$ (blue). (Wallace and Hobbs, 2006)

Figure 2.1 shows that the difference between $e_s(T)$ and $e_{si}(T)$ is always positive, exhibiting a maximum at about -12°C (Wallace and Hobbs, 2006). This implies that, in water-saturated conditions, the air is supersaturated with respect to ice and water vapor will deposit upon ice particles, which is an important process for the formation of precipitation in cold clouds (see section 2.1.2).

As illustrated in Figure 2.1, saturation vapor pressure varies with temperature and obeys the *Clausius-Clapeyron equation*

$$\frac{de_s}{dT} = \frac{L_v}{T(\alpha_v - \alpha_l)} \quad (2.3)$$

with the latent heat of vaporization $L_v = 2.25 \cdot 10^6 \text{ Jkg}^{-1}$ and the change in specific volume ($\alpha_v - \alpha_l$) of the phase transition.

If an air parcel rises in a hydrostatically balanced environment, it will expand due to the decreasing pressure of the surrounding air and experience *adiabatic cooling*, which implies no heat exchange with the environment. The air parcel's temperature decreases with altitude at the dry adiabatic lapse rate until it reaches its dew point, i.e. the temperature at which the relative humidity equals 100% and water vapor becomes saturated.

Ascent beyond this level leads to water vapor supersaturation, which is necessary for cloud formation. In the atmosphere supersaturation with respect to liquid water or ice is achieved by convective, frontal or orographic lifting of an air parcel. Under these conditions, condensation or deposition of water vapor onto particles in the air may occur and a cloud of small water droplets or ice particles evolves. The involved processes of cloud particle nucleation and growth are described in the following section focusing on the nucleation of ice crystals in cold clouds.

2.1.2 Ice particle nucleation

In the atmosphere two phase transitions are possible which initiate the formation of ice particles in cold clouds: freezing of a liquid cloud droplet or direct deposition of water vapor to the solid phase. In contrast to deposition, for condensation-freezing the existence of supercooled water droplets in the cloud is required. After a short overview of cloud liquid droplet formation in the next paragraph, nucleation of ice particles in clouds is discussed subsequently.

Cloud water droplets in natural clouds form by heterogeneous nucleation, i.e. water vapor condenses onto atmospheric aerosol particles. Without these particles in the air, supersaturation with respect to water of several hundred percent would be necessary for the onset of condensation (Rogers and Yau, 1989). For heterogeneous nucleation of water droplets the required supersaturation is much lower than for homogeneous nucleation in the absence of solid aerosol particles. A droplet, formed by chance collisions of water molecules, is stable and may continue to grow if its size is larger than a critical radius. This radius depends on the temperature, the degree of supersaturation, and the surface tension of the droplet.

Hygroscopic particles, i.e. particles with an affinity for water, can serve as *cloud condensation nuclei* (CCN). As numerous of them are present in the atmosphere, supersaturation with respect to water usually does not exceed a few percent. The formation of water droplets starts almost immediately when the relative humidity exceeds 100% (Gierens et al., 2012). Typically, cloud droplets have radii of about 10 μm and form a cloud with concentrations of some hundred droplets per cubic centimeter (Rogers and Yau, 1989).

If the cloud ascends to higher altitudes in the further development, it eventually reaches temperatures below 0°C . Even under these conditions, cloud water droplets may exist as *supercooled droplets* in cold clouds. Usually, clouds with cloud top temperature between 0°C and -10°C predominantly contain supercooled droplets. The probability of ice occurrence in clouds increases with decreasing temperature. If cloud top temperature decreases below -20°C , almost all clouds contain ice particles and only about 10% of clouds still consist entirely of supercooled droplets. At temperatures below about -40°C supercooled droplets freeze spontaneously to ice particles and clouds become glaciated (Pruppacher and Klett, 1997).

The formation of ice crystals is a very complex process and, in contrast to the water droplet formation, the underlying physical and chemical principles are poorly understood (Cantrell and Heymsfield, 2005). Ice nucleation does not start immediately at ice saturation. Significant supersaturation with respect to ice is frequently observed in the atmosphere. Thus, *ice supersaturation* is a metastable state, which may last for a certain time before returning to equilibrium (Gierens et al., 2012). The conditions under which supercooled droplets or water vapor may nucleate to ice particles are explained in the following paragraphs. Basically, there are two different processes for the formation of ice: homogeneous and heterogeneous nucleation.

Homogeneous nucleation

Homogeneous nucleation is the aggregation of water molecules by chance without the presence of other particles. This process occurs at very low temperatures around -40°C as observed in high clouds, e.g. in the ice anvils of thunderstorms. Homogeneous nucleation, in fact, is the dominant mechanism for the formation of cirrus clouds (Pruppacher and Klett, 1997).

Spontaneous nucleation takes place if the phase transition implicates a decrease in Gibbs free energy of the system. The change in *Gibbs free energy* for phase transitions from liquid water to ice is defined as

$$\Delta E = nV(\mu_i - \mu_l) + A\sigma \quad (2.4)$$

where n is the number of water molecules per unit volume of ice, V and A the volume and surface area of the ice embryo, respectively, $\Delta\mu = \mu_i - \mu_l$ the (negative) change in Gibbs free energy due to the phase transition from liquid to ice and σ the surface energy of ice.

After Eq. 2.4 two opposing parts contribute to the change in Gibbs free energy. The first term decreases free energy due to the transition of molecules into a state of increased molecular order in the crystal. The second term increases the system's free energy as work has to be done for the formation of the surface between ice and liquid phase (Hegg and Baker, 2009). This term acts as an *energy barrier* to nucleation which has to be overcome by a forcing, i.e. a cooling (decrease in thermal energy of the molecules) (Kärcher, 2012). Under supersaturated conditions ΔE may be positive or negative depending on the size of the initial ice cluster formed by random collisions. An ice embryo with an initial radius larger than a critical value is stable and will continue to grow, as its growth is associated with a negative ΔE . Smaller clusters imply an increase of free energy in the system and will consequently break up.

With decreasing temperature the nucleation rate and the size of ice embryos increases rapidly as the magnitude of $\Delta\mu$ increases sharply and therefore the energy barrier to nucleation is diminished. This steep rise of the nucleation rate occurs at a narrow temperature range around the *spontaneous freezing temperature* which depends on the volume of the considered water droplet. Consequently, most drops of comparable sizes freeze at this narrow temperature range (Hegg and Baker, 2009). Various laboratory measurements of homogeneous freezing are shown as blue symbols with a regression line in figure 2.2. As illustrated in this figure, homogeneous freezing occurs already at temperatures of -35°C for droplets larger than $100\ \mu\text{m}$ in diameter. For smaller droplets of $1\ \mu\text{m}$ in diameter homogeneous nucleation starts not before temperature decreases below -41°C (Wallace and Hobbs, 2006).

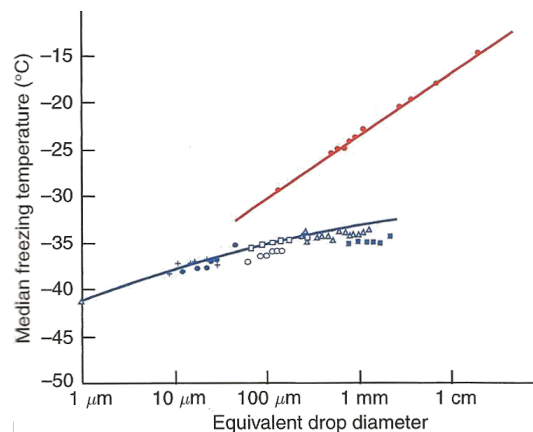


Figure 2.2: Median freezing temperatures of water samples as a function of equivalent drop diameter for homogeneous (blue) and heterogeneous (red) freezing. Different symbols indicate different measurements. (Wallace and Hobbs, 2006)

Heterogeneous nucleation

Remarkably higher freezing temperatures are observed in the presence of certain solid particles, known as *ice nuclei* (IN), which initiate the ice nucleation process. This kind of nucleation process is referred to as heterogeneous nucleation. In this case, the energy barrier to nucleation is reduced substantially compared to homogeneous freezing. Measured freezing temperatures for heterogeneous nucleation as function of droplet diameter are indicated in figure 2.2 (red line). For the largest droplets of about 1 cm in diameter, heterogeneous nucleation occurs at temperatures as high as -15°C , revealing the higher probability for larger droplets to contain a suitable particle for heterogeneous nucleation. Heterogeneous nucleation is suggested to affect the formation of a subset of cirrus clouds, namely cirrus formed by slow, large-scale lifting ($< 10\ \text{cm s}^{-1}$) or small cooling rates (DeMott et al., 2003). Under these conditions, relatively low ice supersaturations are achieved which are not sufficiently for the onset of homogeneous nucleation.

There are four different modes of heterogeneous nucleation: condensation-freezing, immersion, contact nucleation and deposition (Pruppacher and Klett, 1997). If water vapor condensates upon an ice nucleus at temperatures below 0°C and water saturated conditions, subsequent

freezing of the formed droplet is referred to as *condensation-freezing*. Water molecules may form an ice-like structure by collecting upon the particle's surface. If this internal structure grows large enough, it causes the droplet to freeze. In the case of *immersion* nucleation, a water droplet formed heterogeneously at temperatures above 0°C , becomes supercooled and freezing is initiated upon the immersed IN at sufficiently low temperatures. Further, ice nucleation may be initiated by *contact nucleation*, i.e. mechanical contact of a supercooled droplet with an IN causes its subsequent freezing. *Deposition* occurs when water molecules freeze directly on a suitable particle from the vapor phase. For this nucleation process ice supersaturation, but not necessarily water saturation, and temperatures low enough are required.

The relative importance of these different ice nucleation modes in the atmosphere has not yet been finally determined by current research (Broadley et al., 2012). The mode in which a suitable aerosol particle is activated as IN depends on its material, the temperature and the supersaturation conditions of the ambient air, as can be seen in figure 2.3.

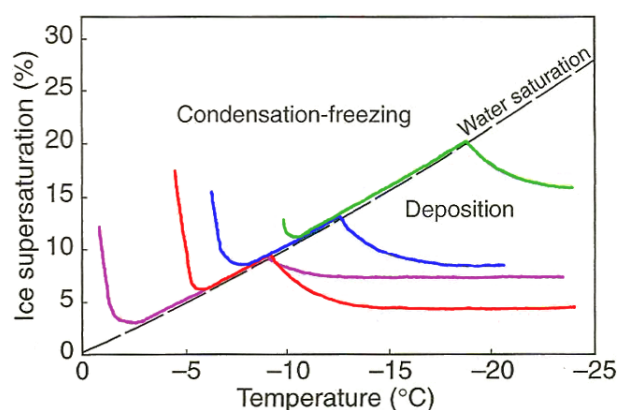


Figure 2.3: Onset of ice nucleation as a function of temperature and ice supersaturation for various materials: silver iodide (red), lead iodide (blue), methaldehyde (violet), and kaolinite (green). Ice nucleation starts above the shown lines. (Wallace and Hobbs, 2006)

The onset of ice nucleation (condensation-freezing) under water-supersaturated conditions occurs at higher temperatures and lower ice supersaturation than under water-subaturated conditions, when only deposition nucleation is possible. Silver iodide, for example, acts as condensation-freezing nucleus at temperatures above -9°C . Below that temperature it may serve as deposition nucleus, if certain ice supersaturation is reached (red line in fig. 2.3). Looking at kaolinite (green line in fig. 2.3), deposition occurs below a temperature of -18°C and even higher critical ice supersaturation (Wallace and Hobbs, 2006).

Only a small number of all tropospheric aerosol particles can serve as IN. This rarity of suitable ice nuclei explains the frequently observed ice supersaturations. The conditions for effective IN are very stringent due to the highly organized, hexagonal ice crystal structure. About one of a million aerosol particles is suitable as IN (Gierens et al., 2012); under most favorable conditions of aerosol composition up to 1 of 1000 particles (DeMott et al., 2003). Most effective IN are characterized by the following properties, among others: insolubility, crystal structures similar to crystalline ice, ability to bind water molecules, and sizes larger than $0.1\ \mu\text{m}$. Examples are inorganic soil particles (mineral dust), organic materials, such as decayed plant leaves or

plankton, as well as anthropogenic aerosols, e.g. soot from aircraft emissions. A typical IN concentration is one per liter of air at a temperature of -20°C (Rogers and Yau, 1989). At any given temperature, increasing ice supersaturation leads to larger numbers of particles active as IN. Generally, IN concentration may vary by several orders of magnitude within a day or less (Pruppacher and Klett, 1997).

2.1.3 Ice crystal growth and ice enhancement

Ice particles, nucleated by the manifold processes described in the last section, grow and eventually reach sizes large enough to precipitate. In this section, the processes of ice particle growth are described: growth by diffusion of water vapor, riming and aggregation. Besides, associated secondary processes of ice formation are introduced, so-called ice enhancement mechanisms.

Water vapor which is close to saturation with respect to water is supersaturated with respect to ice, i.e. the saturation vapor pressure is lower adjacent to an ice particle than to a water droplet. For example, in water saturated conditions water vapor is supersaturated with respect to ice by about 10% at a temperature of -10°C . In turn, vapor pressure in equilibrium with an ice surface is subsaturated with respect to water. In mixed phase clouds, therefore, supercooled droplets will evaporate in the vicinity of an ice particle, which will start to grow due to *diffusion* of water vapor (see fig. 2.4). This way, ice crystals may grow to many tens of micrometers in dimension (Rogers and Yau, 1989). The diffusion growth rate reaches a maximum at a temperature of about -15°C , where the difference in saturation pressure with respect to water and ice shows a maximum (Wallace and Hobbs, 2006).

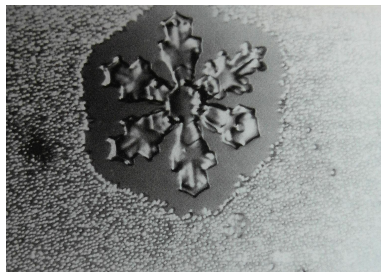


Figure 2.4: Laboratory experiment of ice particle growth by diffusion at the expense of surrounding supercooled water droplets. (Wallace and Hobbs, 2006)

A second process of ice particle growth is referred to as *riming*. Ice crystals falling through a mixed phase cloud may collide with thousands of supercooled water droplets. After the collision the cloud droplet freezes onto the impacting ice crystal (collector), which consequently grows in mass. The products of this growth mechanism are several rimed structures, including graupel, where the primary crystal shape cannot be recognized any more, as well as hailstones, as the result of extreme riming.

Riming might be the most important explanation for *ice enhancement*. Observed cloud ice particle concentrations often exceed IN concentrations by a factor of up to 10^5 . Typically, measured ice particle concentrations vary from 0.01 per liter up to 100 per liter, with high concentrations

typically found in cirrus clouds (Rogers and Yau, 1989). The discrepancy between ice particle and IN concentrations leads to the assumption of secondary processes of ice formation which increase ice particle concentration without the involvement of IN. Freezing of water droplets during the process of riming starts from the outer part of the drop, thereby enclosing water in its interior. If this water freezes, it expands and may cause the rimed particle to break up and splinter in numerous small ice particles.

If falling ice particles collide with other ice particles in the cloud and stick together after the collision, they grow by *aggregation*. Examples of aggregates or snowflakes formed this way are shown in figure 2.5. A necessary condition for aggregation is a difference in fall speed of the ice particles. The terminal fall speed of an ice crystal is determined by its shape, mass, dimension, and the degree of riming. The second condition for aggregation is the adhesion of two colliding ice particles, which depends on temperature and ice particle shape. The probability of adhesion increases with increasing temperature and becomes significant at temperatures higher than -10°C (Rogers and Yau, 1989). Most aggregated crystals have diameters between 2 and 5 mm, but aggregates as large as 15 mm in diameter may occur (Pruppacher and Klett, 1997).

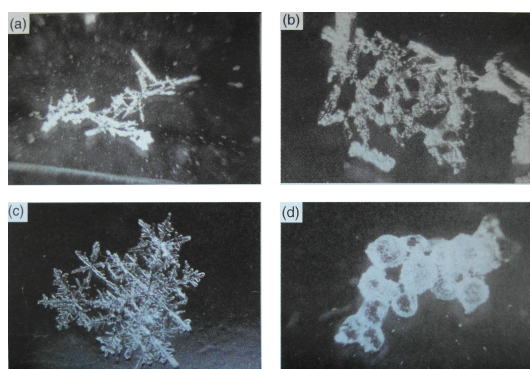


Figure 2.5: Aggregates of rimed needles (a), rimed columns (b), dendrites (c), rimed frozen droplets (d). (Wallace and Hobbs, 2006)

By these growth mechanisms ice particles may be generated which are large enough to precipitate. Cold clouds, in fact, play an important role in the formation of precipitation as has already been pointed out by Franklin (1789): “*It is possible, that in summer, much of what is rain, when it arrives at the surface of the earth, might have been snow, when it began its descent;*”. In the 1930s, Bergeron and Findeisen conducted first quantitative studies on the formation of precipitation in cold clouds. Ice crystals can grow to precipitation-sized particles in reasonable time periods (about 40 min) in the so called *Bergeron-Findeisen process*. According to their theory, ice crystals grow at first by deposition from vapor in mixed phase clouds and then by riming and aggregation up to diameters of 5 to 10 mm. Falling below the 0°C level, they may begin to melt and form raindrops, typically 1 to 2.5 mm in diameter (Pruppacher and Klett, 1997).

2.1.4 Microphysical properties of cirrus clouds

“Ice cloud radiative properties depend on the ice crystal optical properties, which in turn depend on the microphysical properties.” (Key et al., 2002). Consequently, the effect of ice clouds on climate is very sensitive to their microphysical properties, which are described in this section. Namely, microphysical properties characterizing a cloud include cloud phase, particle shape composition, particle size distribution, particle concentration, and ice water content.

The following explanations are focused on the microphysics of midlatitude *cirrus clouds*. These are pure ice clouds formed in the upper troposphere at temperatures ranging from -30°C to -80°C (DeMott et al., 2003). In a review of studies on cirrus clouds Dowling and Radke (1990) determine typical ranges of physical cirrus properties. According to this review cirrus typically exhibit an ice water content of 0.025 gm^{-3} ($10^{-4} - 1.2 \text{ gm}^{-3}$), ice particle maximum dimensions of $250 \mu\text{m}$ ($1 - 8000 \mu\text{m}$), and particle number concentrations of 30 per liter ($10^{-4} - 10^4 \text{ L}^{-1}$). Baum et al. (2005b) shows that there are substantial differences in the bulk scattering properties of ice clouds formed in areas of deep convection and those that exist in areas of much lower updraft velocities. For most synoptically generated midlatitude cirrus, the largest crystal sizes measured are typically less than $1500 \mu\text{m}$. Larger particles tend to settle out quickly because of relatively low updraft velocities (Baum et al., 2005a).

Ice particle shape

Ice particles exhibit a wide diversity of shapes, so called *ice particle habits*. The basic shape of ice crystals is hexagonal, given by the lattice structure of ice. Which habit a single ice crystal assumes is determined by the ice formation process and the ambient conditions, i.e. temperature, pressure and supersaturation.

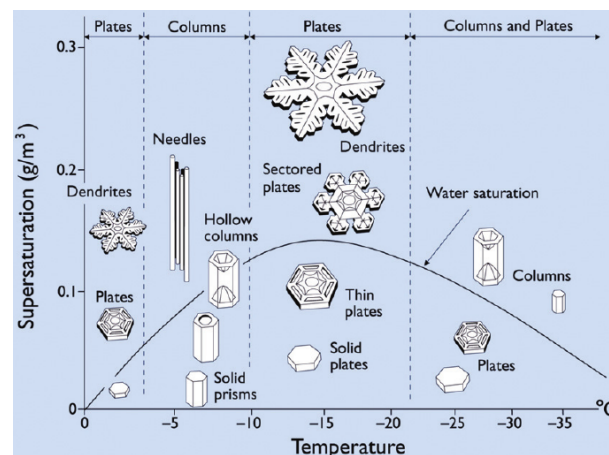


Figure 2.6: Morphology diagram of ice crystal types growing at atmospheric pressure as function of temperature and supersaturation relative to ice. The water saturation line indicates the supersaturation relative to water. Temperature mainly determines whether crystals will grow into plates or columns, while higher supersaturations produce more complex structures. (Libbrecht, 2005)

Figure 2.6 illustrates different regimes of single habit formation as function of temperature and ice supersaturation. Three major changes of ice crystal habit occur at temperatures of -3°C , -9°C and -22°C . At these temperatures, the observed crystal morphology switches between plate-like and column-like particles (Libbrecht, 2005). At temperatures below -20°C Bailey and Hallett (2004) found even more variable ice crystal shapes. According to this study, plate-like polycrystals dominate at temperatures from -20°C to -40°C while columnar polycrystals (e.g. bullet rosettes) dominate at temperatures below -40°C . The particular habit distribution depends thereby on ice supersaturation. With increasing supersaturations crystal structure becomes increasingly complex.

While figure 2.6 reflects typical shapes of single ice crystals, in natural ice clouds also interactions between crystals influence their shape. Therefore, cloud particle shapes are often dominated by polycrystalline forms. Aggregates can display rough surfaces due to coalescence-collision during ice crystal growth (Yang et al., 2000). Usually cirrus clouds contain a mixture of different habits as ambient conditions vary within the cloud especially in the vertical. Typical mixtures of ice particle shapes may be deduced from various in-situ measurements (see e.g. Baum et al. (2005a)). In-situ observations based on airborne two-dimensional optical probes and balloon-borne replicators show that the majority of ice crystals in cirrus clouds are bullet rosettes, solid and hollow columns, plates, and aggregates with sizes ranging from 5 to about $1000\ \mu\text{m}$ (Heymsfield and Platt, 1984).

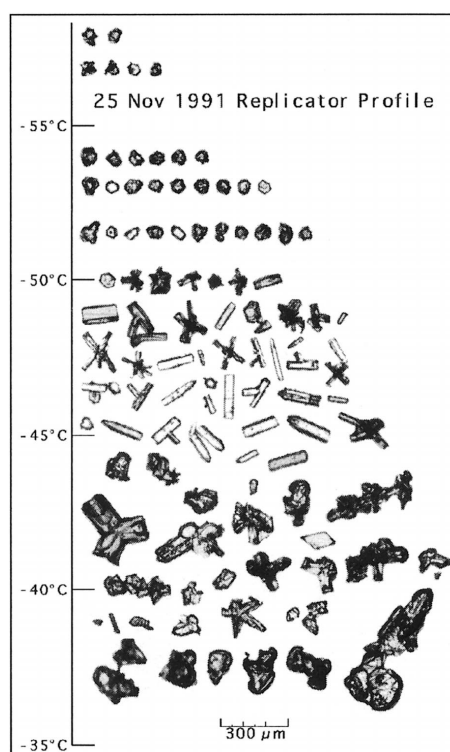


Figure 2.7: Balloon-borne ice crystal replicator data collected on 25 Nov 1991 during the FIRE-II experiment near Coffeyville, Kansas. The approximate temperature at the replicator height is indicated along the ordinate. (Heymsfield and Miloshevich, 2003)

Heymsfield and Miloshevich (2003) studied ice particles in midlatitude, synoptically generated stratiform ice clouds, i.e. ice clouds formed by large-scale ascent as opposed to deep convection. The ice particle population in such cirrus is typically dominated by bullet rosettes, beside less dominant columnar crystals (Heymsfield and Iaquinta, 2000). Balloon-borne ice crystal replicator profiles through these cirrus clouds have shown that particle shapes vary considerably in the vertical under different ambient conditions. As illustrated in figure 2.7 most observations exhibit an increasing particle size with distance to cloud top, while the size distribution broadens. This is consistent with the idea that particles nucleate at cloud top and grow as they fall. Three layers may be distinguished in figure 2.7. The cloud top layer consists of compact, relatively spherical crystal shapes. This region is thought to be highly supersaturated with respect to ice, promoting ice nucleation and early particle development in the active generation phase of cirrus clouds. In midcloud levels the ambient ice supersaturation is lower, and particles grow to more spatial habits, such as rosettes and columns. In the cloud base layer aggregation becomes increasingly important and sublimation tends to round particle surfaces.

Size distribution

Another important microphysical property of a cloud is its *particle size distribution* (PSD). As nonspherical particles do not have a well-defined radius, their size is often described by means of maximum dimension D_{\max} . For reasons of clarity, the maximum dimension of a particle D_{\max} is denoted simply with D in the following. The number of cloud particles with maximum dimension in the range $[D, D + dD]$ per unit volume is given by $n(D)dD$ (Wyser, 1998). Particle size distributions $n(D)$ may be represented by a lognormal or gamma distribution. In this work, PSDs are parameterized as gamma distributions of the form

$$n(D) = N_0 D^\nu e^{-\eta D} \quad (2.5)$$

with the dispersion ν , the slope η of the distribution, and the intercept $N_0 = \eta^{\nu+1}/\Gamma(\nu + 1)$ where Γ is the gamma function (Baum et al., 2005a). The values for the intercept, slope, and dispersion can be derived from measured size distributions (Heymsfield et al., 2002).

On the basis of in-situ PSDs and theoretical scattering calculations, parameterizations of ice cloud particles in radiative transfer simulations can be obtained (see section 3.2.2).

Integrating the PSD over all particle sizes yields the *particle number concentration* N per unit volume

$$N = \int_0^\infty n(D) dD \quad (2.6)$$

The amount of ice per unit volume of air, expressed in grams per cubic meter, is called *ice water content* IWC which is determined as

$$IWC = \rho_i V_{tot} = \rho_i \int_0^\infty n(D) V(D) dD \quad (2.7)$$

with the density of ice $\rho_i = 0.917 \text{ g cm}^{-3}$ and the total volume V_{tot} of particles integrated over the size distribution (Schumann et al., 2011). In general, the condensed water content of a cloud is the sum of its liquid water content LWC and its ice water content IWC.

Characteristics of PSDs vary substantially depending on ice formation processes, development stage of the cirrus, issues of different measurement techniques, and the maximum dimension definition of different shaped crystals. Examples of PSDs obtained in several field campaigns are shown in figure 2.8. It is beyond the scope of this study to go into details of field campaigns or measurement techniques, but it has to be noted here that determining the correct number of small ice particles ($< 100 \mu\text{m}$) with current in-situ sampling techniques is still an issue (Sassen et al., 1989; Baum et al., 2005a; Baran, 2012). Figure 2.8 shows that PSDs from tropical cirrus associated with deep convection (TRMM) are much broader than for midlatitude synoptic cirrus (ARM and FIRE-II). The narrowest size distribution is observed for CRYSTAL FACE, where the coldest cloud was sampled (Baum et al., 2005a).

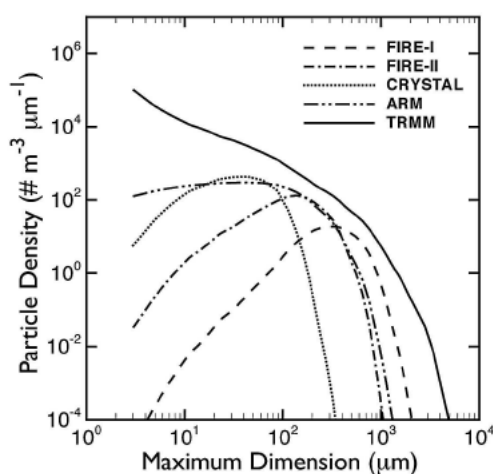


Figure 2.8: Sample of gamma-fit PSDs selected from various field experiments. (Baum et al., 2005a)

Radiative properties of ice clouds

Cloud microphysical properties also determine the interaction of clouds with solar radiation and therefore the radiative properties of clouds. To describe the radiative impact of a cloud, two parameters are necessary which can be retrieved by passive remote sensing and are related to the cloud microphysical properties introduced above: the effective diameter which is an area weighted mean diameter of cloud particles and the cloud optical thickness which is a measure for the attenuation of radiation passing through a cloud (Thomas and Stamnes, 2002).

There are various ways to define the *effective diameter* D_{eff} of nonspherical particles, showing substantial discrepancies between each other (McFarquhar et al., 1998). In general, it is proportional to the ratio of the ice particle volume to its projected cross-sectional area.

After Yang et al. (2000), the effective diameter of a nonspherical ice crystal is defined as

$$D_{\text{eff}} = 2 r_{\text{eff}} = \frac{D_V^3}{D_A^2} = \frac{3}{2} \frac{V}{A} \quad (2.8)$$

where D_V is the diameter of a volume equivalent sphere, D_A the diameter of a sphere with equivalent projected area, V the ice particle volume, and A its projected cross-sectional area.

In contrast to characterizing a single crystal, a *bulk effective diameter* may be defined which is representative for a whole cirrus cloud and is obtained by integrating crystal properties over both size and habit distribution. According to Yang et al. (2005), the bulk effective diameter D_{eff} for a given cloud particle size and habit distribution is determined as

$$D_{\text{eff}} = 2 r_{\text{eff}} = \frac{3}{2} \frac{V_{\text{tot}}}{A_{\text{tot}}} = \frac{3}{2} \frac{\int_{D_{\text{min}}}^{D_{\text{max}}} \left[\sum_{h=1}^M f_h(D) V_h(D) \right] n(D) dD}{\int_{D_{\text{min}}}^{D_{\text{max}}} \left[\sum_{h=1}^M f_h(D) A_h(D) \right] n(D) dD} \quad (2.9)$$

with the ice particle volume $V_h(D)$, the projected cross-sectional area $A_h(D)$, and the particle size distribution $n(D)$. The habit fraction $f_h(D)$ for habit h and size D is defined such that $\sum_{h=1}^M f_h(D) = 1$ for each particle size bin, where M is the total number of habits.

The second important cloud radiative property is the cloud *optical thickness* τ which is approximately determined by

$$\tau \approx \frac{3}{2} \frac{IWC}{\rho_i r_{\text{eff}}} \Delta z \quad (2.10)$$

with the bulk density of ice ρ_i and the geometrical height Δz of the cloud layer.

This relationship, as well as the concept of effective radius, is valid only for short wavelengths or large particles, i.e. in the geometric optics limit with $Q_{\text{ext}} \approx 2$ as explained in section 2.2.2.3 (Hansen and Travis, 1974). This constraint reveals the close relation of cloud microphysical properties, introduced in this chapter, their optical properties, and their consequent effect on radiation. To provide a basis for understanding the involved interactions, the next section gives an overview of the principles of radiation and its interaction with matter in the atmosphere.

2.2 Radiation in the Atmosphere

“*Solar radiation drives weather and climate of the Earth.*” (Mayer, 2009). Energy is redistributed within the atmosphere and exchanged with Earth’s surface mainly by means of radiation, which therefore plays a major role in balancing the Earth’s energy budget.

Solar and terrestrial radiation may also be exploited by *remote sensing* to gain insight into atmospheric composition. On its way through the atmosphere, radiation is modified by various interactions with atmospheric constituents and consequently carries a lot of information about them. By remote sensing of clouds, their microphysical properties (cf. section 2.1) that are relevant for interaction with radiation may be retrieved. The solution of this inverse problem involves the comparison of radiation measurements to radiative transfer simulations (Zdunkowski et al., 2007). In this study, properties of ice clouds are to be deduced from ground-based remote sensing of atmospheric transmission. This section introduces the fundamental physical laws of radiation and radiative transfer, which form the basis of the subsequent discussion.

2.2.1 Definition of radiation quantities

Radiation is the propagation of energy through space or matter in form of energetic particles (photons) or *electromagnetic waves*. The existence of electromagnetic waves as the result of interacting electric and magnetic fields was first formally postulated by Maxwell (1865). The general solution of his fundamental Maxwell equations is a transversal wave with the electric field vector normal to the direction of wave propagation. In vacuum, these waves travel with a characteristic velocity, specifically the speed of light $c = 2.998 \cdot 10^8 \text{ ms}^{-1}$. Another characteristic of electromagnetic waves is their wavelength $\lambda = c/\nu$, where ν is the wave frequency.

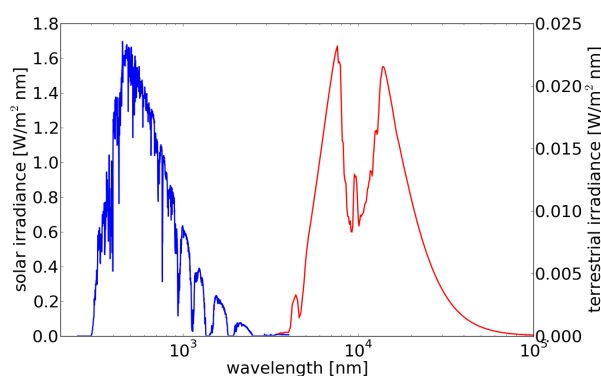


Figure 2.9: Solar and terrestrial spectral downward irradiance at Earth’s surface (simulation for solar zenith angle 30° , cloudless, standard midlatitude summer atmosphere).

The electromagnetic spectrum may be separated in two major wavelength regions (see figure 2.9). *Solar radiation* which is emitted by the sun prevails in the shortwave wavelength region with $\lambda < 4 \mu\text{m}$. In contrast, thermal or *terrestrial radiation* emitted by the Earth and its atmosphere dominates in the longwave spectral region ($\lambda > 4 \mu\text{m}$) (Zdunkowski et al., 2007).

This study focuses on methods using solar radiation separated into visible (0.4 - 0.7 μm), near infrared (0.7 - 1.0 μm) and shortwave infrared (1.0 - 4.0 μm) spectral regions.

Quantity	Symbol	Definition	Unit
Radiant Energy	Q		J
Radiant Power	Φ	$\frac{dQ}{dt}$	W
Irradiance	E	$\frac{d\Phi}{dA}$	Wm^{-2}
Radiance	L	$\frac{d\Phi}{dA \cos \theta d\Omega}$	$\text{Wm}^{-2}\text{sr}^{-1}$
Spectral Radiance	L_λ	$\frac{d\Phi}{dA \cos \theta d\Omega d\lambda}$	$\text{Wm}^{-2}\text{sr}^{-1}\text{nm}^{-1}$

Table 2.1: Definition of radiation quantities. (adopted from Mayer, 2009)

In atmospheric sciences radiation is described by several quantities shown in table 2.1. The radiant energy flux onto a flat surface per unit area and unit time is called the *irradiance* E which is dependent on the orientation of the receiving detector. A second way to quantify radiation is the *radiance* L , which additionally takes into account the direction of light propagation. It is defined as the radiant energy per unit time, per unit area $dA \cos \theta$ (normal to the direction considered) and per unit solid angle $d\Omega = \sin \theta d\phi d\theta$, which has units of steradian [sr]. Radiance is a function of direction expressed in terms of zenith angle θ and azimuth angle ϕ . This geometry is illustrated in figure 2.10.

In general, radiative intensity is described by the Stokes vector providing full information on the polarization of radiation. Polarization effects are neglected in this study and only the first component of Stokes vector, i.e. the unpolarized radiance, is considered.

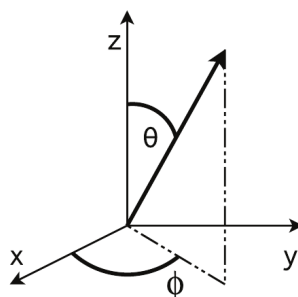


Figure 2.10: Definition of zenith angle θ and azimuth angle ϕ . (adopted from Mayer, 2009)

Since all of the radiation quantities are dependent on wavelength, they can be expressed as spectral quantities. For example, the *spectral radiance* L_λ is the amount of radiance measured in a small wavelength interval $d\lambda$ centered at wavelength λ .

Within the scope of this thesis, spectral radiances are measured by a ground-based sensor, in order to investigate the transmission of ice clouds in the upper troposphere.

In the following, spectral *transmittance* T is defined as

$$T_\lambda = \frac{\pi L_\lambda}{E_{0,\lambda} \cos \theta_0} \quad (2.11)$$

where L_λ is the transmitted spectral radiance, θ_0 the solar zenith angle and $E_{0,\lambda} \cos \theta_0$ is the normal incident extraterrestrial irradiance at top of the atmosphere.

2.2.2 Interaction of radiation and the atmosphere

In the Earth's atmosphere, radiation is affected by emission, absorption and scattering due to gas molecules, aerosols, and cloud water or ice particles. Each of these interactions with atmospheric matter imprints a specific signature on the radiation spectrum, which can be analyzed by remote sensing algorithms. The principles of these processes are explained in the next paragraphs following primarily Petty (2006) and Zdunkowski et al. (2007).

2.2.2.1 Emission

The source of atmospheric radiation is the emission by matter which radiates energy in form of electromagnetic waves depending on its temperature. To describe the characteristics of emission, the concept of a blackbody is considered. This is a body that completely absorbs all incident radiation. In this case, the ratio of absorbed to incident radiation, called absorptivity α_λ , is equal to unity ($\alpha_\lambda = 1$) for all wavelengths λ . The spectral radiance emitted by a blackbody is expressed by *Planck's radiation law*

$$B_\lambda(T) = \frac{2hc^2}{\lambda^5} \frac{1}{\exp(\frac{hc}{\lambda kT}) - 1} \quad (2.12)$$

with Planck's constant $h = 6.626 \cdot 10^{-34}$ Js and Boltzmann constant $k = 1.381 \cdot 10^{-23}$ JK⁻¹.

In contrast, a gray body can also reflect and transmit radiation resulting in an absorptivity smaller than unity ($\alpha_\lambda < 1$). The ability of a body to emit radiation compared to a blackbody is referred to as emissivity ϵ_λ , i.e. the dimensionless ratio of emitted spectral radiance to the spectral blackbody radiance:

$$L_\lambda = \epsilon_\lambda B_\lambda(T) \quad (2.13)$$

According to *Kirchhoff's law*, absorptivity and emissivity for a specific wavelength and direction are equal in thermodynamic equilibrium: $\epsilon_\lambda(\theta, \phi) = \alpha_\lambda(\theta, \phi)$. In local thermodynamic equilibrium, collision between gas molecules are much more frequent than absorption or emission of radiation by the molecules at a considered wavelength. This condition is met in the Earth's atmosphere up to altitudes of around 60 km (Wallace and Hobbs, 2006).

In this case, thermal radiation emitted by an atmospheric layer may be determined by Planck's radiation law (cf. Eq. 2.13) for the according temperature.

The maximum of emitted blackbody radiance shifts to longer wavelengths for lower temperatures of the blackbody. This is stated by *Wien's displacement law*, which determines the wavelength of peak emission for a blackbody of temperature T

$$\lambda_{max} = \frac{2897 \mu\text{m K}}{T} \quad (2.14)$$

Integrating Planck's radiation law over the half space and all wavelengths gives the irradiance emitted by a blackbody of temperature T . This relationship is described by *Stefan-Boltzmann law*

$$E = \sigma T^4 = \pi \int_0^\infty B_\lambda(T) d\lambda \quad (2.15)$$

where $\sigma = 5.67 \cdot 10^{-8} \text{ Wm}^{-2}\text{K}^{-4}$ is the Stefan-Boltzmann constant.

On average, the Earth's radiation budget is balanced by absorption of solar radiation and emission of thermal radiation. Provided that the irradiance emitted by Earth and atmosphere amounts to 235 Wm^{-2} , inverting the Stefan-Boltzmann law yields an effective temperature $T = 255 \text{ K}$ of the Earth, which implies a maximum of emitted intensity at $10 \mu\text{m}$ (Andrews, 2010).

The solar spectrum can closely be approximated by the Planck curve of a blackbody with $T = 5778 \text{ K}$ showing a maximum at 475 nm . On average, the Earth receives 1368 Wm^{-2} from the sun integrated over the whole spectrum. Figure 2.11 shows planck functions integrated over the half space representative of the Earth (red line) and of the sun (blue line). Applying the inverse square law gives the solar spectrum at top of the atmosphere (dotted blue line). As mentioned earlier in section 2.2.1, solar and terrestrial spectra may be separated at a wavelength of around $4 \mu\text{m}$ and terrestrial radiation may be neglected when dealing with solar radiation.

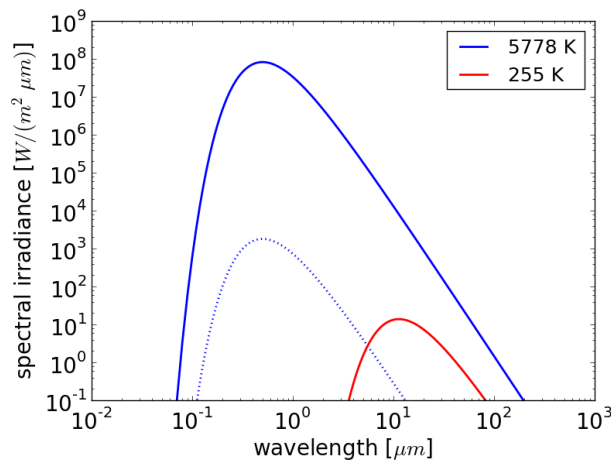


Figure 2.11: Planck functions representative of the sun (blue line) and of the Earth (red line) and for solar irradiance at top of atmosphere (dotted blue line).

After introducing emission as source of radiation, the next section considers an attenuation process, namely the absorption of radiation by atmospheric matter.

2.2.2.2 Absorption

The Earth's atmosphere is almost transparent for radiation in the visible spectral range. In contrast, infrared radiation is partly absorbed by atmospheric gases. The primary absorbing constituent of the atmosphere is water vapor which is present in highly variable concentrations. Beside water vapor (H_2O), several gases in the atmosphere absorb radiation at characteristic *absorption lines*, such as carbon dioxide CO_2 , ozone O_3 , oxygen O_2 , methane CH_4 , and nitrous oxide N_2O . Absorption by these gases is illustrated in figure 2.12 for an altitude of 11 km and at ground level.

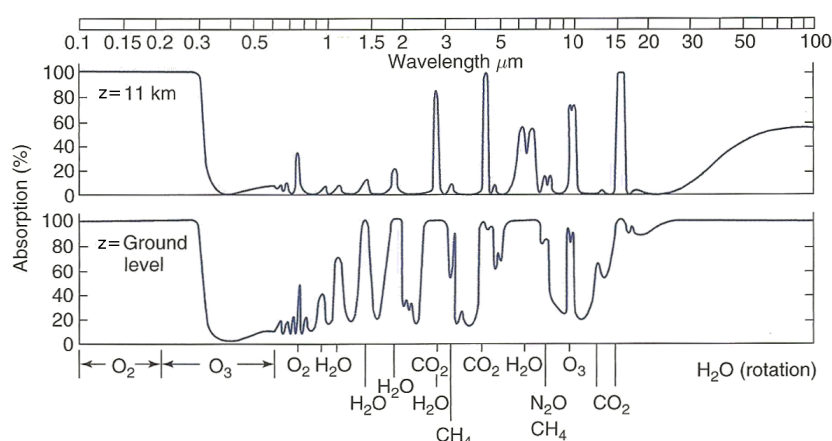


Figure 2.12: Spectral absorption of the atmosphere above 11 km (upper panel) and of the entire atmosphere (lower panel). (Wallace and Hobbs, 2006)

Absorption is the wavelength dependent decline of radiation intensity while passing through a medium. By absorption radiative energy is partly converted to heat or other forms of energy. Contrary to the perception of radiation as electromagnetic waves in section 2.2.1, it is described now as energetic particles, so called *photons*. A photon is characterized by its quantized energy $E = h\nu$ with the frequency ν and the Planck's constant h . Consequently, E is inversely proportional to the wavelength of radiation. This discrete photon energy has to match certain values to be absorbed by a molecule, as only distinct molecular energy levels are permitted by the laws of quantum mechanics. As a result, narrow absorption lines are visible in the spectrum characteristic for certain molecules.

The process of photon absorption implies a discrete energy transition in the internal energy of a molecule, which is composed of its *rotational*, *vibrational* and *electronic* energy. By absorption the molecule reaches an excited state associated with an increase of internal energy by $\Delta E = h\nu$. Transitions in the rotational energy involve the smallest energy change and absorption lines in the far infrared and microwave part of the spectrum. For vibrational energy transitions a larger amount of energy is necessary, causing absorption lines in the shortwave infrared and thermal infrared wavelength range. Most energetic transitions are changes of the electron orbits in a molecule, which result in ultraviolet and visible absorption lines. Translational kinetic energy is associated with random molecular motion and is not quantized in a similar manner (Petty, 2006).

The natural finite, though very small, width of absorption lines has its origin in the Heisenberg uncertainty principle: The finite lifetime of a molecule's excited state implies an uncertainty in the photon energy and therefore absorption is distributed over a narrow frequency interval. This effect is referred to as *natural broadening* of absorption lines, which is negligible compared to the following two broadening mechanisms. *Doppler broadening* occurs due to the Doppler-shift of absorption frequencies relative to the natural line position. This is caused by random thermal motions of air molecules toward or away from the source of radiation. *Pressure broadening* is associated with the collision of molecules in the troposphere and the lower stratosphere, that randomly disrupt natural transitions (Wallace and Hobbs, 2006).

Beside gas molecules, also atmospheric particles, such as aerosols, cloud droplets, and ice crystals contribute to atmospheric absorption. For matter homogeneous on the spatial scale of wavelength, the rate of absorption is determined by the imaginary part of its *refractive index* ($n = n_r + in_i$), which depends on wavelength and on particle phase. This dependency allows to discriminate between cloud liquid and ice water by remote sensing (Kokhanovsky, 2004). The imaginary part of the refractive index for liquid water and ice is indicated in figure 2.13 for the shortwave infrared spectral range. Between 2.1 μm and 2.25 μm , for example, n_i shows little variation for liquid water, but decreases sharply with wavelength for ice. Martins et al. (2011) shows that *phase discrimination* is possible using the ratio of measured radiances reflected from cloud sides at these two wavelengths. This concept is adopted to cloud transmittance in this study (see section 4.2).

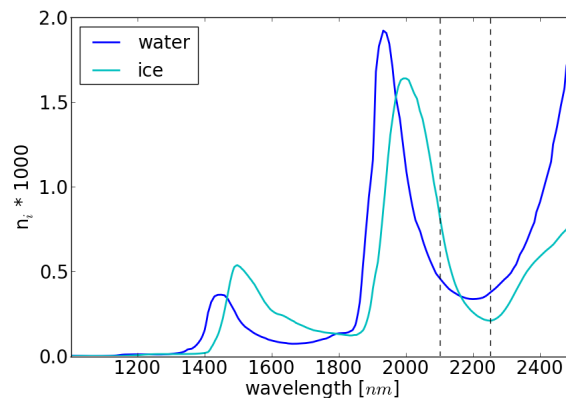


Figure 2.13: Imaginary part of the refractive index for water and ice in the shortwave infrared. (from MIEV0 code by Wiscombe, 1980)

Generally, the cross-sectional area of a particle, that contributes to absorption is called the *absorption cross-section* σ_{abs} [m^2], which is a function of wavelength. The absorption efficiency Q_{abs} is defined as the ratio of absorption cross-section σ_{abs} to the particle's geometric cross-section A . Integrating σ_{abs} over the PSD $n(r)$ of cloud particles yields the rate of attenuation by absorption per unit distance, the so-called *volume absorption coefficient* k_{abs} [m^{-1}]

$$k_{abs} = \int_0^{\infty} \sigma_{abs}(r)n(r) dr = \int_0^{\infty} Q_{abs}(r)A(r)n(r) dr \quad (2.16)$$

Attenuation in the atmosphere occurs not only due to the described process of absorption, but also by scattering of radiation. The principles of scattering are introduced in the next section.

2.2.2.3 Scattering

Scattering particles may change the propagation direction of incident radiation. A scattering particle can be described as an aggregation of a large number of discrete elementary electric charges. The incident plane electromagnetic wave excites these charges to oscillate and thereby radiate secondary electromagnetic waves into all spatial directions. The superposition of these interfering waves yields the total elastically scattered field, i.e. the frequency of scattered radiation is equal to the incident frequency. By this scattering event a part of the energy from the incident beam is extracted and redirected to a new direction (Bohren and Clothiaux, 2006).

Scattering by atmospheric particles depends crucially on the relation between particle size r and the wavelength λ of incident radiation. Therefore, the optical properties of particles and the methods to calculate particle scattering are a function of the *size parameter* x , defined as

$$x = \frac{2\pi r}{\lambda} \quad (2.17)$$

where r the radius of a spherical scattering particle or in case of a nonspherical particle half of its maximum dimension $r = 0.5 \cdot D_{\max}$ (Yang et al., 2005).

Basically, there are three regimes of scattering in the atmosphere as indicated in figure 2.14:

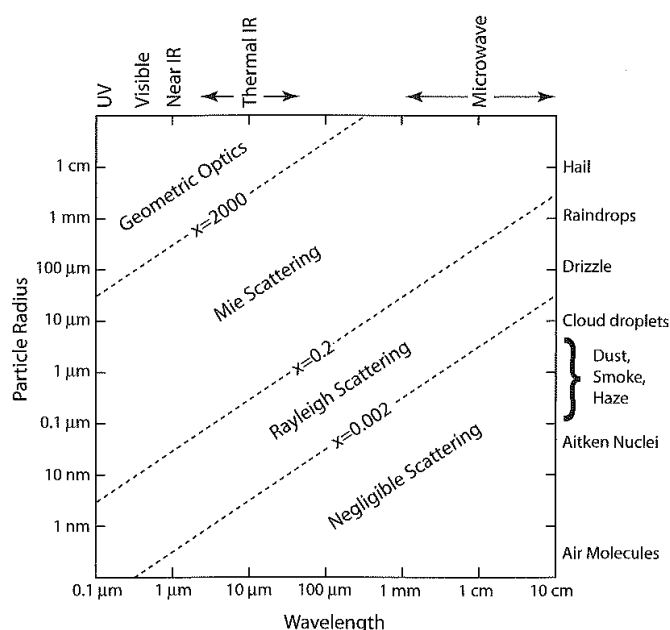


Figure 2.14: Relation between particle size, radiation wavelength and scattering behavior of atmospheric particles: approximate regime boundaries are indicated as dashed lines. (Petty, 2006)

Beside the size parameter x , the real part of the refractive index $n_r = c/v_{ph}$ associated to the scattering particle governs its scattering properties, as it determines the phase speed v_{ph} of electromagnetic waves. Additionally, the particle shape has an influence on the particle's scattering properties. For cloud water droplets, raindrops, and aerosol particles it is convenient to assume spherical particle shape. For nonspherical particles, such as ice crystals or snow flakes, this is not appropriate and, therefore, the calculation of their optical properties is much more complicated (Petty, 2006).

Analogous to the absorption cross-section (c.f. Eq. 2.16) of a particle, its scattering cross-section σ_{sca} is determined as the ratio of radiant power scattered by the particle in all directions to the irradiance of the incident beam (Bohren and Clothiaux, 2006). Integrating σ_{sca} over the size distribution $n(r)$ yields the *volume scattering coefficient* k_{sca} [m^{-1}]

$$k_{\text{sca}} = \int_0^{\infty} \sigma_{\text{sca}}(r)n(r) dr \quad (2.18)$$

The *scattering efficiency* Q_{sca} is defined as σ_{sca} normalized by the particle's geometrical projected cross-section A . The scattering efficiency of nonabsorbing particles as function of size parameter is shown in figure 2.15 for PSDs with different effective variance b . The broader the size distribution, the smoother the curve becomes. Wavelike structures and superimposed resonances associated with single particle sizes disappear due to superimposition of different particle size contributions. Figure 2.15 gives an overview of the different scattering regimes. In the limit of very small size parameters, Q_{sca} is approximated by Rayleigh scattering theory. In the geometric optics limit, for large x , the scattering efficiency approaches $Q_{\text{sca}} \approx 2$, known as extinction paradox (Zdunkowski et al., 2007).

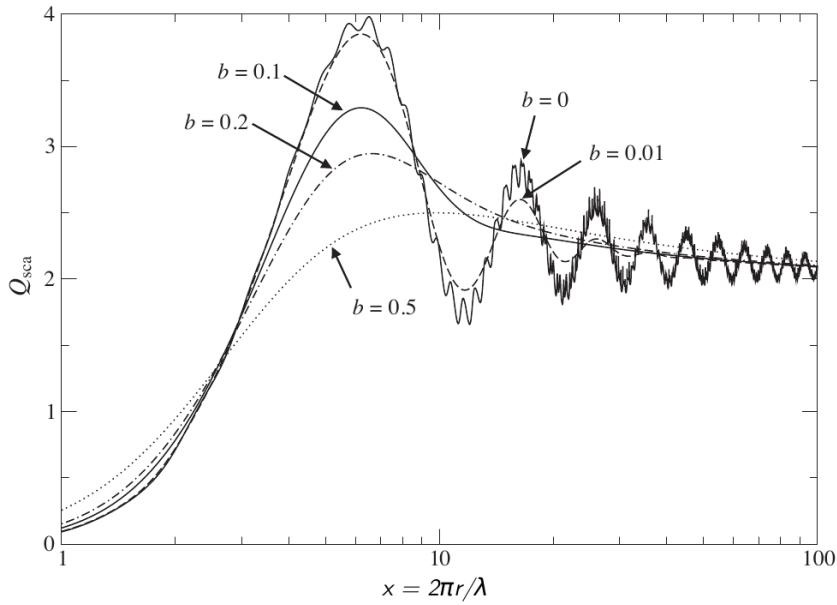


Figure 2.15: Scattering efficiency for size distributions with various effective variances b as function of size parameter x with $r = r_{\text{eff}}$. (Zdunkowski et al., 2007)

Generally, the angular probability distribution of scattering radiation incident from direction $\Omega' = (\theta', \phi')$ into the direction $\Omega = (\theta, \phi)$ is described by the *phase function* $P(\Omega', \Omega)$. The phase function has to be normalized to ensure energy is conserved in the scattering event:

$$\frac{1}{4\pi} \int_{4\pi} P(\Omega', \Omega) d\Omega' = 1 \quad (2.19)$$

where Ω' and Ω are unit vectors of incoming and scattered direction, respectively.

For spherical particles, the phase function depends only on the scattering angle Θ_{sca} and may be written as $P(\cos \Theta_{\text{sca}})$ where $\Theta_{\text{sca}} = \arccos(\boldsymbol{\Omega}' \cdot \boldsymbol{\Omega})$ (Petty, 2006). For randomly orientated nonspherical particles, the same definition is often assumed resulting in phase functions which are rotationally symmetric around the direction of incidence (Zdunkowski et al., 2007).

In the next paragraphs the features of different scattering regimes are explained in more detail.

Molecular scattering - Rayleigh theory

If particle size is very small compared to wavelength ($r \ll \lambda$) which is true for radiation in the visible or UV spectral range incident on air molecules ($r \approx 10^{-4} \mu\text{m}$), the laws of *Rayleigh scattering* apply (Rayleigh, 1899).

The unpolarized phase function for Rayleigh scattering is given by

$$P_{\text{Rayleigh}}(\cos \Theta_{\text{sca}}) = \frac{3}{4}(1 + \cos^2 \Theta_{\text{sca}}) \quad (2.20)$$

with the scattering angle Θ_{sca} . This implies a maximum of scattering probability in the forward and backward direction and a minimum for scattering angles of $\Theta_{\text{sca}} = 90^\circ$ as illustrated by the red curve in figure 2.16.

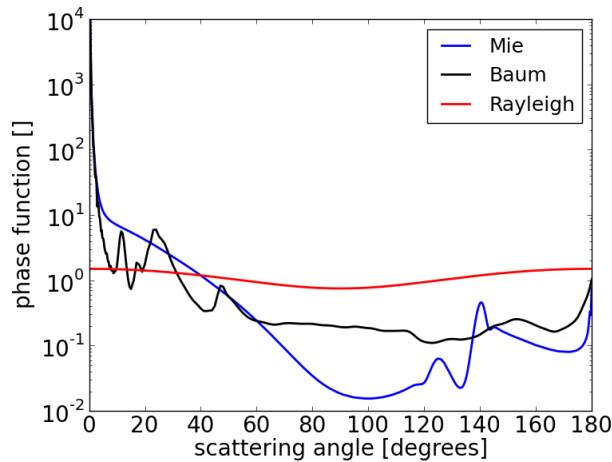


Figure 2.16: Phase functions of Rayleigh scattering (red line), Mie scattering for water droplets (blue line, $b = 0.1$) and ice crystal scattering (black line) for a typical habit mixture (Baum et al., 2005a), calculated for a wavelength of 550 nm and effective radius $r_{\text{eff}} = 25 \mu\text{m}$.

The scattering cross-section σ_{sca} and hence the intensity of Rayleigh scattering is inversely proportional to the 4th power of wavelength ($L \propto \lambda^{-4}$). Consequently, scattering of visible light by air molecules is more efficient at shorter wavelengths resulting in the blue color of the sky and the red colors of sunset. Rayleigh scattering is a special case of Mie scattering, introduced below, in the limit of small particles.

Scattering by spherical particles - Mie theory

When scattering particles are comparable in size to the wavelength of incident radiation ($r \approx \lambda$), the so-called *Mie solution* may be applied to calculate particle optical properties. In 1908, Mie published his exact analytical solution of Maxwells equations for scattering by homogeneous spherical particles. This theory is applicable, for example, to scattering by cloud water droplets and incident radiation in the visible through infrared spectral range.

According to Mie theory, the phase function shows a strong forward peak of scattering probability as indicated in figure 2.16 (blue curve). There are also some secondary features in the backscatter direction, including the cloudbow at 140° scattering angle. The proportion of photons that are scattered in the forward direction relative to photons scattered in the backward direction is given by the *asymmetry parameter* g

$$g = \frac{1}{4\pi} \int_{4\pi} P(\cos \Theta_{\text{sca}}) \cos \Theta_{\text{sca}} d\Omega \quad (2.21)$$

For $g = 1$ only forward scattering occurs, while for $g = -1$ exclusively backward scattering takes place and $g = 0$ is associated with isotropic scattering.

For Mie scattering of solar radiation in clouds, g takes values in the range of 0.8 - 0.9 implying strong forward scattering. This is the result of constructive interference in the forward direction of waves scattered by different parts of the particle, which applies not only to spheres but to all particle shapes (Petty, 2006). In contrast, the asymmetry parameter assumes a value of zero for Rayleigh scattering, i.e. forward and backward scattered components are equal.

Mie theory provides an exact solution for scattering on homogeneous spheres. However, an exact theory for scattering by nonspherical particles covering all size parameters does not exist. Consequently, a combination of different methods, such as finite-difference time domain (FDTD) method and geometric optics, has to be applied (Liou and Takano, 1994).

Geometric optics approximation

For scattering particles much larger in size than the incident wavelength ($r \gg \lambda$), Mie solution converges to the results of *geometric optics approximation* (GOA). In this case, radiation is understood as a collection of independent parallel rays propagating along straight lines. Upon incidence on a particle's surface these rays undergo local reflection and refraction. Scattered light beams are assumed to be incoherent, i.e. there are no systematic phase relations between the waves scattered by individual particles. Therefore, intensities of reflected and refracted rays can be added without regard to phase. The extinction efficiency in geometric optics equals a value of two ($Q_{\text{ext}} = 2$) (Mishchenko et al., 1999). In conventional GOA diffraction and interference effects of light are neglected (Thomas and Stamnes, 2002).

Each ray is traced by applying Snell's law of refraction, which is expressed as follows:

$$n_i(\lambda) \sin \alpha_i = n_r(\lambda) \sin \alpha_r \quad (2.22)$$

with the refractive index (real part) of the medium of incidence n_i and the medium of refraction n_r , and the angle of incidence and refraction α_i and α_r , respectively (Liou and Takano, 1994).

As a major advantage, GOA can be applied to arbitrarily shaped scattering particles (Mishchenko et al., 1999). Examples are scattering of visible radiation by cloud ice crystals with maximum dimensions larger than $50\ \mu\text{m}$ or raindrops ($r > 100\ \mu\text{m}$) (Petty, 2006). As mentioned above, for smaller size parameters ($x < 20$) other methods have to be applied such as FDTD method (Yang and Liou, 1996a).

The geometric optics method can explain optical phenomena visible as sharp features in the phase functions of rain drops and ice crystals. Beside the narrow forward scattering peak of rain drops, their phase function shows characteristic features at 137° and 130° , the primary and secondary rainbow, respectively.

Figure 2.16 (black line) indicates the phase function for a typical habit mixture of ice crystals (see section 3.2.2) which shows two distinct features at scattering angles of about 22° and 46° , the so-called *halos*. A halo may appear as a bright ring around the sun in the presence of a thin cirrostratus cloud layer containing unoriented ice columns, as illustrated in figure 2.17. The reason for these optical phenomenon lies in the hexagonal structure of the scattering ice particles. Radiation is refracted at two faces of the hexagonal column crystal without internal reflection. Rays passing through two crystal side faces inclined by 60° to each other are refracted at angles in the range from 22° up to 50° . Thereby, most rays are deflected by angles near 22° forming the bright inner edge of the halo. The rare 46° halo occurs if the relative angle of the two crystal faces is equal to 90° (side and end face of the column).



Figure 2.17: 22° halo observed on 2012-09-27 at UFS. (courtesy of F. Ewald)

Halos are an example for the dispersion of sunlight. As can be seen in figure 2.17, the inner edge of the halo appears sharp and red becoming diffuse to the white or blueish outer edge. The reason for this is the wavelength dependency of the refractive index which implies that wavelengths associated to blue color are refracted at larger angles than red color.

2.2.3 Radiative transfer equation

In the atmosphere attenuation of radiation is caused by both absorption and scattering as explained in the previous sections. The resulting extinction of a medium implies an exponential decay of intensity while passing the medium. The extinction increment $dL_\lambda(s)$ along an infinitesimal pathlength ds is given by *Lambert-Beer's law* denoted in integrated form as

$$L_\lambda(s) = L_\lambda(0) \exp\left(-\int_0^s k_{\text{ext},\lambda}(s') ds'\right) \quad (2.23)$$

where $L_\lambda(0)$ is the extraterrestrial radiance at $s = 0$ and $k_{\text{ext}}(s)$ the extinction coefficient of the medium as defined below.

The exponent in equation 2.23 defines the *optical thickness* of the medium (cf. section 2.1.4) which is the integral of the extinction coefficient along the path s

$$\tau = \int_0^s k_{\text{ext}}(s') ds' \quad (2.24)$$

A layer of optical thickness $\tau = 1$ corresponds to a decrease of radiance by a factor of e^{-1} .

The extinction of a medium is described by its volume *extinction coefficient* $k_{\text{ext}}(s)$ which generally depends on wavelength and is defined as

$$k_{\text{ext}} = k_{\text{abs}} + k_{\text{sca}} \quad (2.25)$$

where k_{abs} and k_{sca} are the absorption and scattering coefficients of the medium.

The *single scattering albedo* characterizes the relative importance of scattering and absorption in a medium given as the ratio of scattering to extinction coefficient

$$\omega_0 = \frac{k_{\text{sca}}}{k_{\text{ext}}} \quad (2.26)$$

In a nonscattering medium ω_0 equals zero and assumes a value of one in a nonabsorbing medium.

By now, all quantities have been introduced to characterize the optical properties of atmospheric constituents: gas molecules, aerosols, cloud droplets, and ice crystals. Cloud optical properties are described by the volume extinction coefficient k_{ext} , the single scattering albedo ω_0 , and the phase function $P(\Omega', \Omega)$. These properties, in turn, depend on the size parameter x , the complex index of refraction, and the cloud particle phase, composition, and shape.

Putting all contributing processes of interaction between radiation and atmospheric matter together, Chandrasekhar (1960) formulated the *radiative transfer equation* (RTE). It can be written as

$$\frac{dL}{ds} = -k_{\text{ext}}L + \frac{\omega_0 k_{\text{ext}}}{4\pi} \int_{4\pi} P(\Omega', \Omega) L(\Omega') d\Omega' + (1 - \omega_0)k_{\text{ext}}B(T) \quad (2.27)$$

with the extinction coefficient k_{ext} , the single scattering albedo ω_0 , the scattering phase function $P(\Omega', \Omega)$ and the blackbody emission $B(T)$.

Solving this equation, the radiance L can be calculated as a function of location (x,y,z) and direction (θ,ϕ) . The radiative transfer equation describes the change in radiance dL passing a small volume element of length ds by three processes. The first term on the right side of equation 2.27 is associated to the extinction of incident radiance by scattering or absorption. Further, the second term accounts for scattering from different directions Ω' into the considered direction Ω . At last, the thermal source of radiation by blackbody emission of the volume element is expressed by the third term of the right side (Mayer, 2009).

For most applications in the Earth's atmosphere, one has to deal either with thermal or solar radiative transfer, as these consider contributions of different spectral regions (see section 2.2.1). In the following study only solar radiative transfer is discussed and thus the thermal emission term may be neglected.

Equation 2.27 is a linear integro-differential equation, and consequently its solution is difficult. There is no analytical solution if scattering of photons is included. Therefore, several simplifications are applied in order to solve the RTE. The atmosphere is often assumed to be plane-parallel which implies neglecting Earth's curvature and dividing the atmosphere into parallel homogeneous layers. Applying this approximation, the variables in equation 2.27 only depend on the vertical coordinate z and the path element ds is expressed as $dz = \mu ds$. The cosine of zenith angle $\mu = \cos(\theta)$ is negative for downward directed radiances ($\mu < 0$) and positive for upward directed radiances ($\mu > 0$). Consequently, the differential optical thickness may be written as $d\tau = k_{ext}dz$. The *plane-parallel assumption* may be justified as usually the atmosphere is highly stratified and it can be applied to homogeneous stratiform clouds, e.g. cirrostratus (Petty, 2006). For the solution of the radiative transfer equation boundary conditions have to be specified, including surface reflectivity and extraterrestrial solar irradiance E_0 , incident at top of atmosphere.

Generally, solar radiation can be separated in *direct and diffuse radiation*. A photon that is not scattered at all contributes to direct radiation, whereas a photon scattered on its way through a cloud layer contributes to diffuse radiation. Scattering in optically thin media, in which photons are scattered only once, can be described by *single scattering theory*. The number density of scattering particles is assumed to be sufficiently small, that the mean distance between the particles is much larger than the incident wavelength and the particles can be treated as independent scatterers. This is a valid assumption for optically thin cloud layers with $\tau_c < 1$ or strongly absorbing media ($\omega_0 < 1$). In this case, the RTE may be solved along one line of sight, which greatly simplifies the problem. For optically thicker or strongly scattering cloud layers, photons will be scattered more than once and radiative transfer simulations have to account for *multiple scattering* (Petty, 2006).

One adequate method to solve plane-parallel radiative transfer problems is the discrete ordinate method (DOM) which is the method of choice in this study (see following section 3.2.1). In broken cloud cases, however, three-dimensional radiative transfer has to be performed to account for the effects of 3D inhomogeneity (Mayer, 2009).

Chapter 3

Methods

3.1 Hyperspectral imaging spectrometer

A remote sensing device, capable of measuring spectral radiances, is necessary to derive cloud radiative and microphysical characteristics from their radiative transmission. In order to collect these measurements, the newly established hyperspectral imaging spectrometer *specMACS* is used which is part of the Munich Aerosol and Cloud Scanner.

In the current setup, *specMACS* consists of two cameras shown in figure 3.1, applicable in the visible to near infrared spectral range (VNIR) and the shortwave infrared spectral range (SWIR). In combination, the system provides continuous radiance spectra covering wavelengths from 400 to 2500 nm. The hyperspectral cameras are manufactured by SPECIM Ltd. Finland. The detailed specifications for each camera are compiled in table 3.1 and explained in the following.

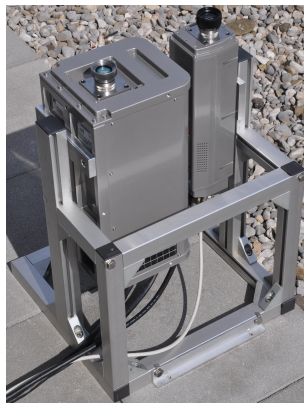


Figure 3.1: First *specMACS* setup with VNIR (right) and SWIR (left) cameras at MIM, June 2012. (courtesy of M. Garhammer)

Each camera contains a two-dimensional detector array with one spatial and one spectral dimension. Adding time as third dimension imaging spectroscopy delivers a three-dimensional data set, called Data Cube. For each spatial pixel, a spectrum of measured radiances is available.

In this context, *hyperspectral imaging* implies that narrow spectral bands are measured over a continuous range of wavelengths. On average, the VNIR camera of specMACS samples spectral radiances every 0.8 nm with a spectral band width of 3.6 nm (full width half maximum). The SWIR camera measures radiances each 6.3 nm with a spectral band width of 11.8 nm. The spatial resolution of the cameras is derived from their field of view (FOV), which is 26° for the VNIR camera and 18° for the SWIR camera. Consequently, the pixel size at 10 km distance from the sensor is approximately 4 m for the VNIR camera and 10 m for the SWIR camera.

specification	VNIR	SWIR
sensor	CMOS (Si-SiO ₂)	CMOS (MCT, cooled to 200K)
pixel (spatial \times spectral)	1312 \times 800	320 \times 256
spectral range	395 - 1020 nm	911 - 2512 nm
spectral sampling	0.78 nm	6.28 nm
spectral band width (FWHM)	3.6 nm	11.8 nm
FOV	26°	18°
focal length	23 mm	30 mm

Table 3.1: Instrument specifications of specMACS for VNIR and SWIR spectrometers.

The principle design of an *imaging spectrograph* can be described as follows: Radiation incident on the spectrometer enters through an entrance slit and a collimating optic produces parallel rays. These fall onto a dispersing element, such as a prism or grating, which separates the radiation spatially by wavelength. After passing a focusing optic the photons fall onto the sensor at a position depending on their frequency and are converted to a voltage.

The basic elements of the spectrometer specMACS are illustrated in figure 3.2. The vision dispersion component applied here is a combination of a transmission volume grating with two almost identical prisms (prism-grating-prism).

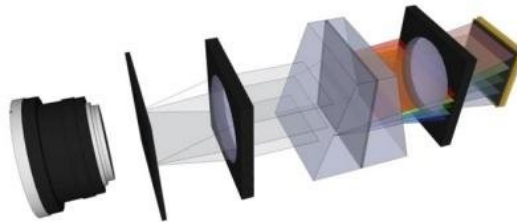


Figure 3.2: Basic concept of a spectrometer with a prism-grating-prism as dispersion element. (adopted from Lambrechts et al., 2011)

This component provides a high diffraction efficiency which is almost independent of polarization and, therefore, constitutes an advantage compared with traditional reflective gratings (Aikio, 2001). Both cameras contain a *CMOS sensor* (complementary metal–oxide–semiconductor) which accumulates signal charges proportional to the local illumination intensity and converts the charges to voltages for each pixel (Litwiller, 2001).

The measured digital numbers are translated to radiances by a *calibration* procedure. Dark current measurements reveal the raw signal originating from thermal emission of sensor electrons, but not from the light source. Therefore, the darkcurrent has to be subtracted from the raw image data. The achieved result is multiplied with calibration factors provided by Specim Ltd. yielding measured radiances in units of $\mu\text{W}/(\text{cm}^2 \text{sr nm})$. The calibration gains for both cameras of specMACS are shown as function of wavelength in the upper panels of figure 3.3. They increase considerably for wavelengths close to the edges of the covered spectral range, probably due to a diminished sensor sensitivity.

As first measurements show, there is an offset between the calibrated VNIR and SWIR spectra. Therefore, it is assumed that the calibration tool of SPECIM Ltd. does not correctly account for the integration time of measurements. The calibrated radiances are multiplied by a factor which accounts for the integration time of the calibration and of the measurements ($t_{\text{int,cal}}/t_{\text{int,meas}}$). This eliminates the overall offset between the two spectral ranges. However, the overlapping parts of the two spectra do still not match exactly. This issue can probably be explained by a decreased quality of the calibration in this spectral range. To mark a wavelength range of reliable data, a threshold of maximum acceptable calibration gain is defined as two times the calibration gain averaged over all spatial pixels and a central wavelength range (VNIR: 600-800 nm, SWIR: 1400-2000 nm). This threshold is depicted as red dashed lines in the upper panels of figure 3.3. In the following, reliable data are assumed to lie within the resulting wavelength ranges of 467 - 917 nm (VNIR) and 1296 - 2419 nm (SWIR).

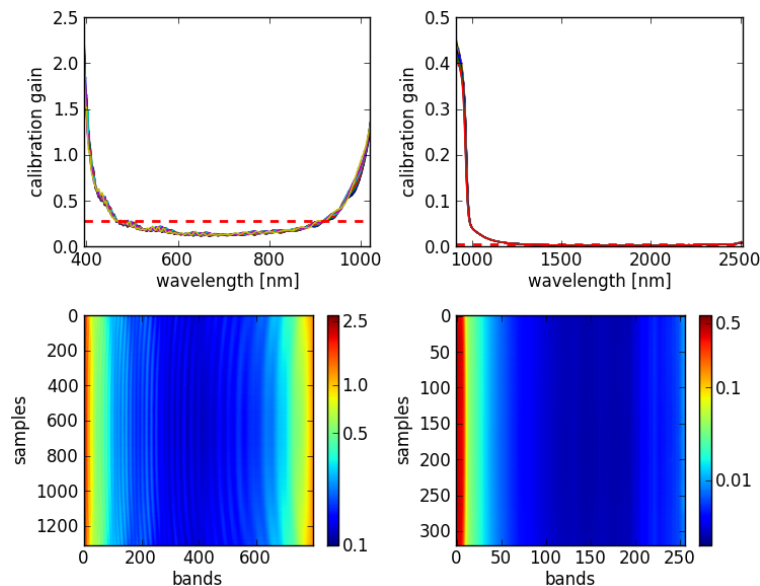


Figure 3.3: Calibration gains for the VNIR camera (**left**) and the SWIR camera (**right**) shown as function of wavelength (**upper panels**) and for the full sensor array (**lower panels**).

The signal accuracy in terms of a *signal-to-noise ratio* $SNR = P_{\text{signal}}/P_{\text{noise}}$ is defined as the ratio of signal power P_{signal} (meaningful information) to background noise power P_{noise} (unwanted). According to Specim Ltd. the signal-to-noise ratio of the SWIR camera is 800:1 at maximum signal level, while no information was provided on the SNR of the VNIR camera.

A very first setup of specMACS is shown in figure 3.1. In this setup, first measurements were obtained at the rooftop of the Meteorological Institute Munich MIM (see section 5.2.1). The cameras were installed on a simple rack looking to the zenith. The vertical adjustment in this case was approximate and not measured by means of a level.

During a measurement campaign at the research station UFS (2650 m a.s.l.) on Mount Zugspitze the system was operated in a more sophisticated setup illustrated in figure 3.4 (courtesy of F. Ewald). The cameras are installed side by side on a telescope mount which allows to scan a wide range of zenith and azimuth angles. For the measurements in this study, the cameras point to the zenith with the spatial line oriented in the principal plane or perpendicular to it. To determine the absolute viewing angle, the mount head is leveled in the horizontal and a relative alignment to the sun position is conducted for each measurement.



Figure 3.4: specMACS setup at UFS, September 2012.

3.2 Radiative transfer simulation

The aim of this study is to derive microphysical properties of optically thin ice clouds from data measured with the spectrometer specMACS introduced in the last section. To provide a basis for such a retrieval, atmospheric radiative transfer through these clouds has to be simulated. The employed models, methods and parameterizations of atmospheric radiative transfer are explained in the following paragraphs.

3.2.1 Radiative transfer model

Radiative transfer was simulated using *libRadtran* - a library of radiative transfer programs (Mayer and Kylling, 2005). This software package contains a selection of codes adequate to solve the radiative transfer equation (see eq. 2.27) for various problems. Besides, libRadtran includes databases for atmospheric absorption and routines to calculate cloud optical properties.

One of the radiative transfer solvers included in libRadtran is the well-tested code DISORT developed by Stamnes et al. (1988, 2000). It allows numerically stable calculations of radiance, irradiance, and actinic flux. The *discrete ordinate technique* (DISORT) is applicable for

one-dimensional plane-parallel radiative transfer simulations. Within this study, this is a valid approximation as horizontally rather homogeneous, thin cirrus clouds are the subject of investigation. DISORT solves the RTE by expansion of the phase function in Legendre series, a Fourier expansion of the radiance field and approximation of the scattering integral by a sum over discrete angles (discrete ordinates). Thereby, the RTE is transformed into a system of linear differential equations, which may be solved numerically (Stamnes et al., 1988). The number of streams impacts the quality of approximation of the phase function (default in DISORT: sixteen streams). In libRadtran, a C-code version of DISORT 2.0 is implemented providing higher computational efficiency and equal or greater accuracy than the original (Buras et al., 2011).

Radiative transfer simulations have to include absorption by gas molecules in the atmosphere. Spectrally resolved (line-by-line) calculations, which account for every single absorption line, are very time-consuming for wavelengths above 500 nm where trace gases show various narrow absorption lines. Molecular absorption can be parameterized using the LOWTRAN band model (Pierluissi and Peng, 1985) adopted from the SBDART code (Ricchiuzzi et al., 1998). This model allows *pseudo-spectral* calculations, i.e. radiation may be calculated at any wavelength, but the gas absorption is provided only at limited resolution (Mayer et al., 2012). LOWTRAN band models include effects of all atmospheric molecules relevant for radiative transfer with a resolution of about 0.5 nm in the visible spectral range. A comparison of LOWTRAN and line-by-line simulations in section 4.1.1 shows that the LOWTRAN parameterization is a valid approximation in this study.

3.2.2 Parameterization of ice clouds

To perform realistic radiative transfer calculations in a cloudy atmosphere, models of cloud bulk microphysical and optical properties are essential. In the following paragraphs ice cloud parameterizations are described which are applied in this study.

Parameterization by Baum et al. (2005a)

Based on aircraft in-situ data obtained from several field campaigns in midlatitudes and tropics, Baum et al. (2005a) developed bulk scattering models of ice clouds for application in remote sensing. Measured particle size distributions are filtered for cloud temperatures below -25°C to ensure the existence of ice phase. The resulting 1117 particle size distributions cover particle maximum dimensions ranging from 2 to 9500 μm divided into 45 size bins. The measured PSDs are parameterized as gamma distributions defined in equation 2.5.

Scattering properties are calculated for several idealized ice crystal shapes shown in figure 3.5: quasi-spherical droxtals, solid and hollow hexagonal columns, hexagonal plates, 3D bullet rosettes, and aggregates of hexagonal columns (two to eight randomly attached columns). The methods to generate this single-scattering library involve a combination of the improved geometric optics approach for large particles (size parameter $x > 30$) and the finite-difference time domain method for $x < 30$ (Yang and Liou, 1996a,b).

The values of ice water content and median mass diameter derived from the in-situ measurements and those calculated from the modeled ice particles are compared in Baum et al. (2005a). Best agreements in this comparison are achieved by assuming a mixture of particle shapes. For this mixture, a library of bulk single-scattering properties (scattering phase function, single-scattering albedo, extinction and scattering cross sections, extinction efficiency, asymmetry parameter) is provided and the information on IWC and particle size (volume, projected area, effective diameter). All properties are averaged over a random particle orientation.

The developed particle-size-dependent habit mixture (“*Baum mixture*”) is defined in four bins of particle maximum dimension D_{\max} :

- $D_{\max} < 60 \mu\text{m}$: 100% droxtals
- $60 \mu\text{m} < D_{\max} < 1000 \mu\text{m}$: 50% solid columns, 35% plates, 15% 3D bullet rosettes
- $1000 \mu\text{m} < D_{\max} < 2000 \mu\text{m}$: 45% hollow columns, 45% solid columns, 10% aggregates
- $2000 \mu\text{m} < D_{\max}$: 97% 3D bullet rosettes, 3% aggregates

The bulk scattering properties of this habit mixture are available for 144 wavelengths in the range from 0.4 - 2.2 μm and for effective diameter from 10 - 180 μm . The resulting phase function of the Baum mixture is indicated in figure 3.6 as dashed black line.

HEY parameterization

In addition to calculations applying the Baum mixture, radiative transfer is simulated for ice clouds consisting of a single habit in order to quantify the effect of different ice particle habits. Bulk optical properties of single habits have been calculated by Claudia Emde (personal communication). These are based on single-scattering property data generated by Hong Gang using the algorithms for single-scattering calculations by Ping Yang (Yang et al., 2000). This parameterization, referred to as “*HEY parameterization*” in the following, covers effective radius values from 5 - 90 μm and wavelengths in the range 0.2 - 5.0 μm . It includes single-scattering properties for six habits: solid columns, hollow columns, six-branch rosettes, plates, droxtals, and roughened aggregates (see figure 3.5). The phase functions for these habits are illustrated in figure 3.6 as colored lines.

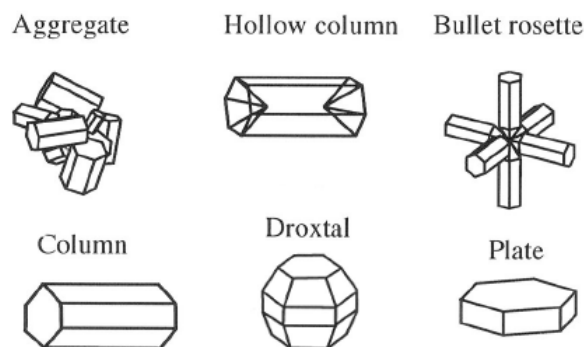


Figure 3.5: Ice crystal habits for scattering calculations. (adopted from Yang et al., 2005)

Similar to the Baum mixture, size distributions are assumed to follow a gamma distribution (cf. equation 2.5) with $\nu = (1/b - 3)$, $\eta = (b r_{\text{eff}})^{-1}$, and $b = 0.25$ (in this study). For spherical particles, r_{eff} is the effective radius and b the effective variance of the size distribution, but for aspherical ice crystals this relations do not hold anymore.

Modified Baum mixture

Unfortunately, the spectral range of the parameterization by Baum et al. does not fully cover the spectral range of the spectrometer specMACS (0.4 - 2.5 μm). Therefore, the bulk optical properties of the Baum mixture are approximated (“*Baum-modified*”) for this study using the single-scattering properties of the HEY parameterization, which cover the full required spectral range. As the dispersion ν of the gamma distribution in the Baum mixture is not known, a value of $\nu = 2$ is assumed. The original Baum mixture changes its composition abruptly at three boundaries in maximum dimension (see above). Consequently some parameters - such as effective radius, projected area, and volume - do not always increase at these boundaries with increasing maximum dimension, as would be expected.

To avoid such physically unrealistic behaviour, the mixture composition is iteratively modified until the monotony criteria are met at each boundary while keeping deviations from the original Baum mixture as small as possible. For each habit, 1% of its contribution to the mixture is iteratively exchanged between two adjacent bins of the 45 particle size bins until all discontinuities in the mentioned parameters are eliminated (Bernhard Reinhardt, personal communication). An example of a resulting phase function is shown in figure 3.6 as solid black line. It closely reproduces the one of the original Baum mixture (dashed solid line).

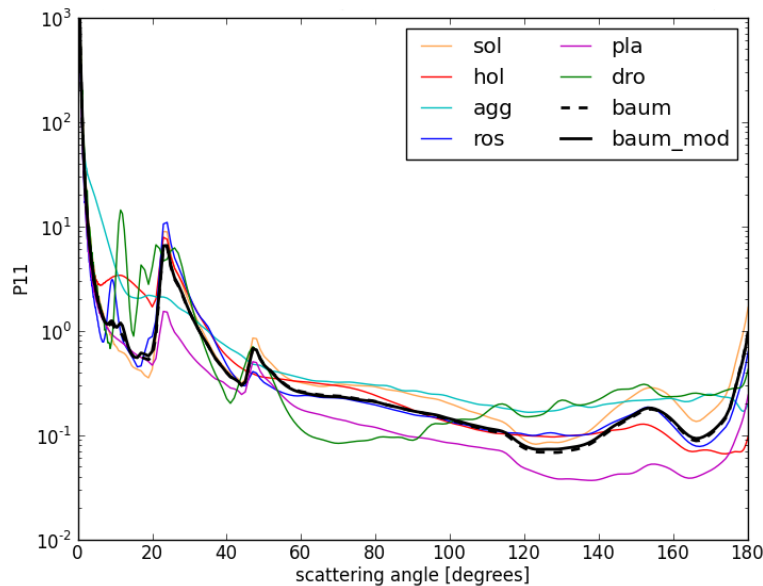


Figure 3.6: Phase functions for HEY parameterization (colored lines), Baum mixture (dashed black line), and Baum-modified parameterization (solid black line) with $r_{\text{eff}} = 50 \mu\text{m}$ and $\lambda = 550 \text{ nm}$.

Chapter 4

Retrieval development

To understand the characteristics of transmission of solar radiation through ice clouds, spectral transmittances - as observable by specMACS - are simulated in this section applying the radiative transfer model libRadtran. After an overview of the chosen atmospheric model settings, the simulated spectra are introduced in section 4.1. The obtained set of simulations is the basis for developing a cloud retrieval in the subsequent sections 4.2 and 4.3.

4.1 Simulation of ice cloud transmittance

4.1.1 Lookup table generation

A common way to retrieve cloud properties from remote sensing data is to compare measurements to simulations of the measured quantity for a set of different model clouds. These simulations may be arranged in so-called lookup tables (LUT). The cloud properties used to simulate the lookup table element closest to the measured value reveal the “true” properties of the measured cloud. In this section, the simulations to set up such a lookup table for ice cloud transmittances are described.

The model atmosphere applied in this study is the *standard summer mid-latitude atmosphere* by Anderson et al. (1986) with an ozone column scaled to 300 DU. The extraterrestrial solar spectrum is taken from Kurucz (1992). Within this atmospheric setting, a horizontally homogeneous *ice cloud layer* is placed at 9 km altitude with 1 km geometrical thickness. The properties of this ice cloud are varied as follows:

- 18 effective radius values ranging from 5 - 90 μm (in 5 μm increments)
- 28 optical depth values ranging from 0 - 20 ($\Delta\tau = 0.5$ for $\tau < 10$, $\Delta\tau = 2.0$ for $\tau > 10$)
- 2 habit mixtures: Baum / Baum-modified; 6 single habits: solid column, hollow column, six-branch rosette, plate, droxtal, roughened aggregate (HEY parameterization)

In libRadtran, the cloud ice water content IWC is scaled according to r_{eff} and τ of the cloud.

The simulation geometry of sun, cloud, and sensor is illustrated in figure 4.1. Simulated *solar zenith angles* θ_0 range from 24° to 60° in increments of 4° . According to specMACS' field of view FOV, *viewing zenith angles* θ_v in the range from 0° - 8° in increments of 2° are computed. The central pixel of the sensor looks to the zenith ($\theta_v = 0^\circ$). Dividing the FOV by the number of spatial pixels of specMACS yields the viewing zenith angle increment observed by a single pixel: $\Delta\theta_v = 0.0196^\circ$ for VNIR and $\Delta\theta_v = 0.0563^\circ$ for SWIR.

Three *relative azimuth angles* $\phi_{rel} = \phi_v - \phi_0$ are taken into account: the sensor's spatial line is either orientated in the principal plane ($\phi_{rel} = 0^\circ, 180^\circ$) or perpendicular to it ($\phi_{rel} = 90^\circ$). As one-dimensional horizontal homogeneous radiative transfer is considered in this study, the absolute solar azimuth angle does not matter and the specification of ϕ_{rel} is sufficient. In the case of $\phi_{rel} = 180^\circ$, the scattering angle is obtained as $\Theta_{sca} = \theta_v + \theta_0$.

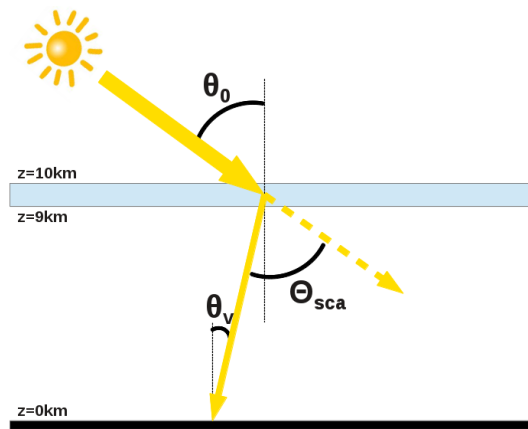


Figure 4.1: Schematic display of sun - cloud - sensor geometry with solar zenith angle θ_0 , viewing zenith angle θ_v , and scattering angle Θ_{sca} for a relative azimuth angle $\phi_{rel} = 180^\circ$.

Two *aerosol* settings are considered for the location in Munich: one case without aerosol and one case assuming continental-average aerosol with 0.2 aerosol optical depth at 550 nm. Aerosol properties are taken from the OPAC aerosol optical properties library (Hess et al., 1998) provided in libRadtran. Aerosol concentration may be neglected in the case of Mount Zugspitze due to the elevated location above the boundary layer where most aerosol is concentrated.

The *surface albedo* has a significant influence on radiances transmitted by thin ice clouds, especially in the VNIR spectral region. Radiation, transmitted by the cloud and reflected at the Earth's surface, is partly re-reflected at cloud bottom and consequently increases the downward radiance incident at ground level. To account for this wavelength dependent effect, a spectrally resolved surface albedo is necessary for hyperspectral transmittance simulations.

Therefore, the ASTER spectral library (Baldrige et al., 2009) is employed to interpolate the MODIS albedo product MOD43B3 (Strahler et al., 1999) which is available at discrete wavelength channels centered at 466, 554, 646, 857, 1242, 1629, and 2114 nm. The MODIS white-sky albedo (WSA) product assumes completely diffuse illumination of the Earth's surface and is derived by integrating the surface's BRDF over the entire solar and viewing hemisphere (bi-hemispherical reflectance). The WSA product is chosen as the diffuse part of illumination is dominant over direct illumination for a wide spread cirrus cloud.

To obtain spectral albedo data representative for the two measurement sites in Munich and on Mount Zugspitze, MODIS WSA data are averaged over an area of 20×20 km surrounding the these locations (see fig. 4.2a and 4.3a). This surface area accounts for more than 50% of the irradiance incident at cloud bottom in 9 km height after Lambertian reflection at ground level. This irradiance can be calculated by integrating the upward radiance weighted with the cosine of viewing zenith angle over all viewing zenith angles. The upper integration limit that yields half of the total irradiance reveals the surface area which has to be taken into account for averaging.

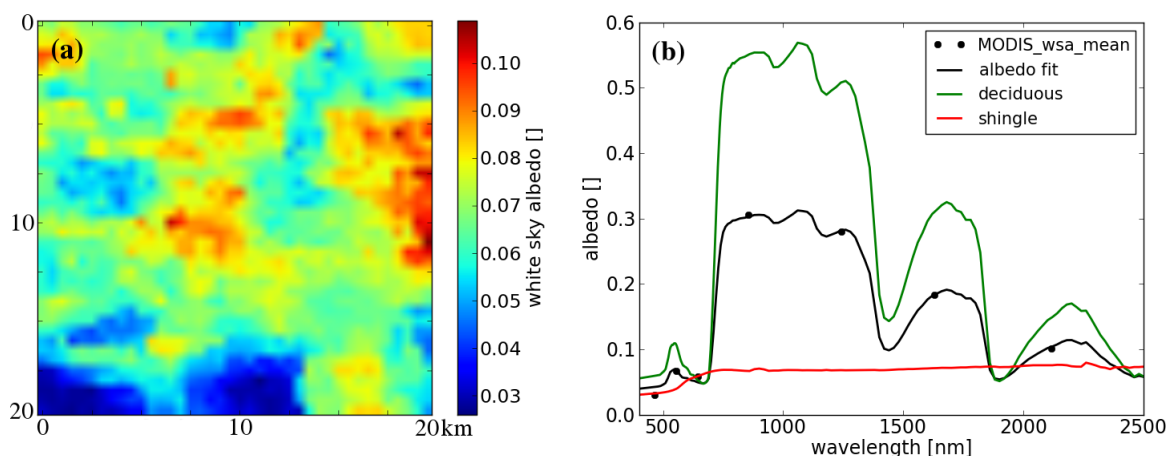


Figure 4.2: (a) MODIS white sky albedo (554 nm) for an area of 20×20 km around MIM, Munich and (b) interpolation of averaged MODIS albedo with $A = (0.5 \cdot A_{\text{deciduous}} + 0.4 \cdot A_{\text{shingle}})$.

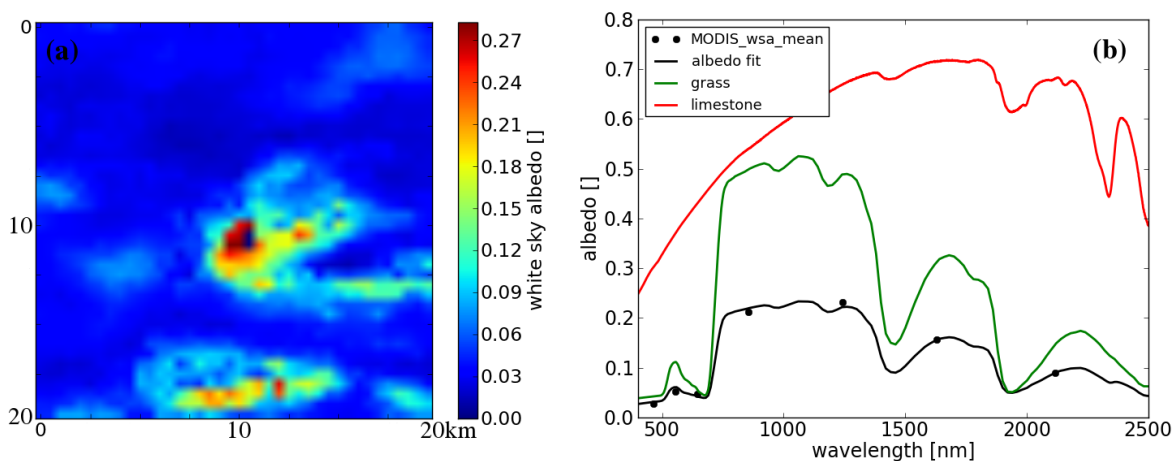


Figure 4.3: (a) MODIS white sky albedo (554 nm) for an area of 20×20 km around UFS, Zugspitze and (b) interpolation of averaged MODIS albedo with $A = (0.39 \cdot A_{\text{grass}} + 0.05 \cdot A_{\text{limestone}})$.

The resulting discrete points of averaged MODIS WSA are interpolated by fitting a linear combination of ASTER spectral albedos to the data: $A = c_1 \cdot A_1 + c_2 \cdot A_2$. The smallest residuals in the least-square-fit are obtained by combining the spectral albedo of deciduous trees and shingles for Munich (fig. 4.2b) and by combining grass and limestone albedos for Mount Zugspitze (fig. 4.3b). The coefficients do not add up to 1, as could be expected, which is probably caused by absolute differences between the 16-day-average MODIS data and the specific conditions

for ASTER albedos. MODIS data acquired in summer 2011 (18th June - 3rd July) are used to represent typical summer conditions in Munich. For Mount Zugspitze a 16-day-period (5th - 21st Sept. 2012) is chosen matching the time period of the measurement campaign.

Another component to be considered in radiative transfer simulations is the *absorption by atmospheric molecules*, which is parameterized with the LOWTRAN band model (cf. section 3.2.1) in this study. To validate this approximation, LOWTRAN simulations are compared to exact line-by-line simulations for an exemplary ice cloud with an optical thickness of $\tau = 1$, an effective radius of $r_{\text{eff}} = 40 \mu\text{m}$, and the Baum habit mixture (the surface albedo is set to 0.2). The molecular absorption coefficients for the line-by-line simulation are generated with the ARTS model (Eriksson et al., 2011) for 10^4 grid points per 100 nm equally spaced in frequency. The simulation results are illustrated for VNIR in figure 4.4 and for SWIR in figure 4.5. The upper panel in each figure shows the line-by-line simulation in full resolution (red line) and averaged to the spectral sampling intervals of specMACS (black line). The lower panels compare these averaged line-by-line simulations with the corresponding LOWTRAN calculations averaged to the same spectral resolution. Apart from the bias in the range 550 - 650 nm (LOWTRAN accounts for Chappuis bands of ozone, in contrast to the line-by-line model), a good agreement between the LOWTRAN and the line-by-line simulations is observed, particularly for the wavelengths (dashed black lines) that are used in the retrieval developed in this study.

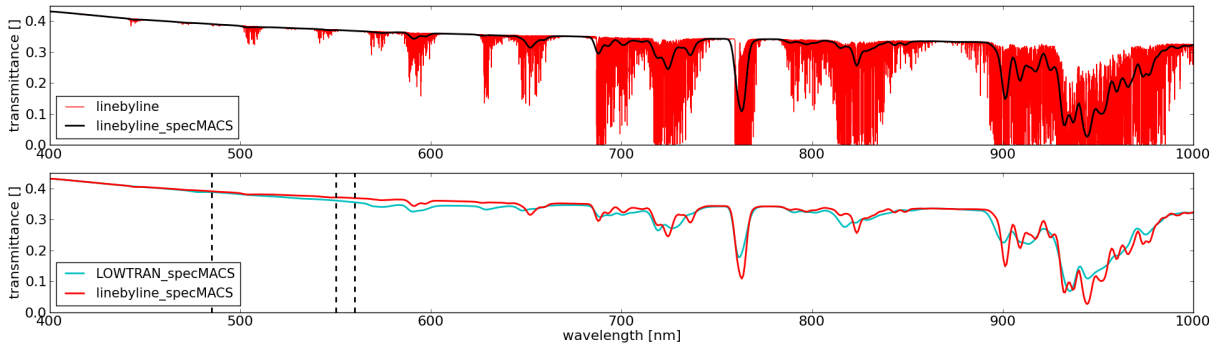


Figure 4.4: Upper panel: Line-by-line simulation in VNIR ($\theta_0 = 30^\circ$, $\theta_v = 0^\circ$, $\tau = 1$, $r_{\text{eff}} = 40 \mu\text{m}$, Baum mixture). **Lower panel:** Comparison of line-by-line (red) and LOWTRAN (blue) simulations averaged to the spectral sampling of specMACS.

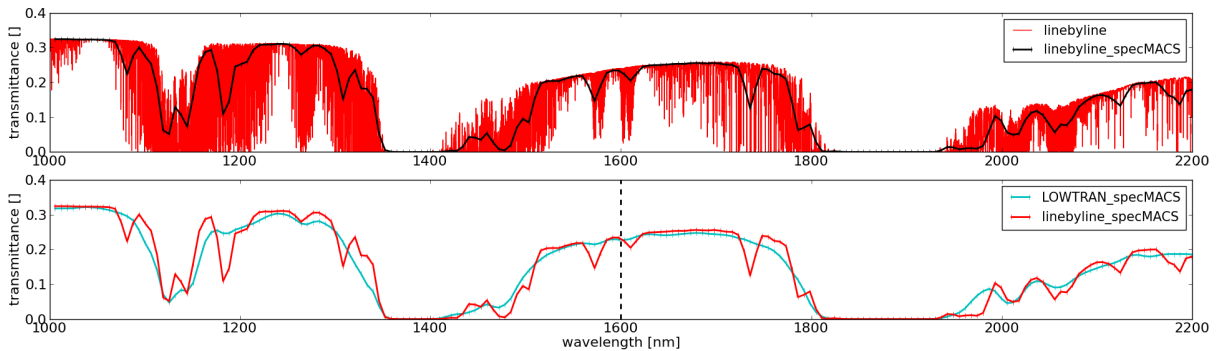


Figure 4.5: Line-by-line (**upper panel**) and LOWTRAN simulation (**lower panel**) in the SWIR spectral range (details as in Fig. 4.4).

4.1.2 Simulated transmittance spectra

The transmittance spectra, resulting from the simulations described in the previous section, exhibit the same spectral sampling interval as the applied extraterrestrial spectrum (0.1 nm in VNIR, 1.0 nm in SWIR). To be able to compare these simulations with measurement data, the simulated spectra are averaged to the wavelength bands sampled by specMACS. Thereby, each band's spectral response function $G(\lambda)$ has to be taken into account. According to Spectim Ltd., a good estimate for the shape of $G(\lambda)$ is a Gaussian curve centered at wavelength λ_0 with a given full width half maximum FWHM and a corresponding variance $\sigma = \text{FWHM}/(2\sqrt{2\ln 2})$.

$$G(\lambda) = \frac{1}{\sqrt{2\pi\sigma^2}} \exp\left(-\frac{(\lambda - \lambda_0)^2}{2\sigma^2}\right) \quad (4.1)$$

Consequently, the transmittance at a considered spectral band is obtained by integrating transmittance spectra weighted with the according Gaussian curve over the surrounding wavelengths:

$$T_{\text{meas}}(\lambda) = \frac{\int_0^\infty G(\lambda - \lambda') T(\lambda') d\lambda'}{\int_0^\infty G(\lambda - \lambda') d\lambda'} \quad (4.2)$$

Figure 4.6 shows simulated spectra averaged to specMACS' spectral bands for various ice clouds. In the visible spectral range transmittances are dominated by scattering of clouds, aerosols, and gas molecules and by Earth's surface reflection. In the near and shortwave infrared absorption occurs in discrete vibrational bands for various species, e.g. H₂O, O₂, and CO₂ (Thomas and Stamnes, 2002). A distinct oxygen absorption line is visible at 760 nm which corresponds to the O₂A-band. Prevalent are the absorption bands for water vapor around 935 nm, 1130 nm, 1400 nm (+ CO₂), 1900 nm (+ CO₂), and 2500 nm (Andrews, 2010).

As illustrated in figure 4.6a, the presence of an optically thin cloud increases transmittances over the whole spectral range compared to the clear sky case with $\tau=0$ (for all viewing angles differing from the direct sun direction).

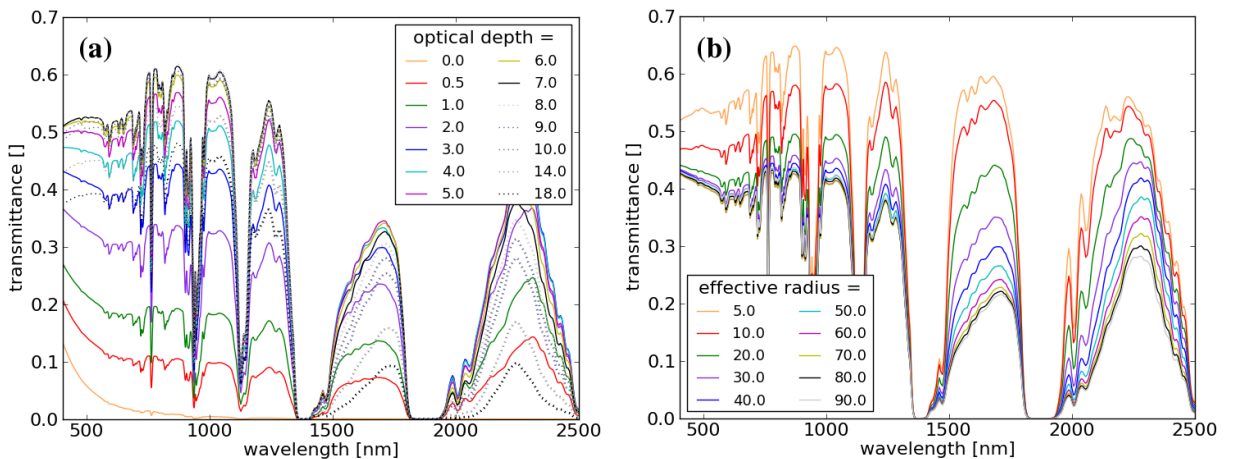


Figure 4.6: Ice cloud transmittance simulations for $\theta_0=36^\circ$, $\theta_v=0^\circ$, $\phi_{\text{rel}}=180^\circ$, and Baum-modified mixture: Variation of (a) optical thickness ($r_{\text{eff}} = 40 \mu\text{m}$) and (b) effective radius values ($\tau = 3.0$).

The reason for this effect is the scattering by cloud particles that increases the diffuse radiation. Successive increase of ice cloud optical thickness leads to even more scattering and increasing transmittances, but also to a growing degree of cloud reflection and absorption. For an optical thickness exceeding a critical value, transmittances decrease again (dashed lines in fig. 4.6a), as soon as the influence of cloud reflection and absorption (especially in the SWIR) becomes dominant. Furthermore, the simulations show that transmittances are especially sensitive to cloud optical thickness in the visible spectral range (fig. 4.6a) and to effective radius in the SWIR spectral region (fig. 4.6b). This correlation may be exploited to retrieve ice cloud properties from measured spectra. The introduced collection of simulated transmittance spectra forms a lookup table used as basis for the cloud retrieval developed in the next sections.

4.2 Retrieval of cloud phase

Detection of the cloud thermodynamic phase is the first step in every cloud property retrieval. Optical properties are considerably different for water and ice particles, which is in particular true for their absorption characteristics. This fact can be used to retrieve cloud thermodynamic phase by remote sensing (Kokhanovsky, 2004).

For cloud side remote sensing, Zinner et al. (2008) and Martins et al. (2011) proposed to use the ratio of reflectances in narrow spectral regions at 2.1 and 2.25 μm to separate between ice and liquid water. Ice phase is detected when this ratio is smaller than 0.6 and water phase for a ratio larger than 0.75. For ground-based remote sensing of cloud phase, Ehrlich et al. (2008) used the slope of the spectrum in the near infrared range between 1.55 μm and 1.7 μm . These examples of phase detection methods are based on the fact that the imaginary part of the complex refractive index n_i depends on wavelength and phase (see fig. 2.13). As n_i determines particle absorption, liquid droplets and ice crystals exhibit different absorption coefficients.

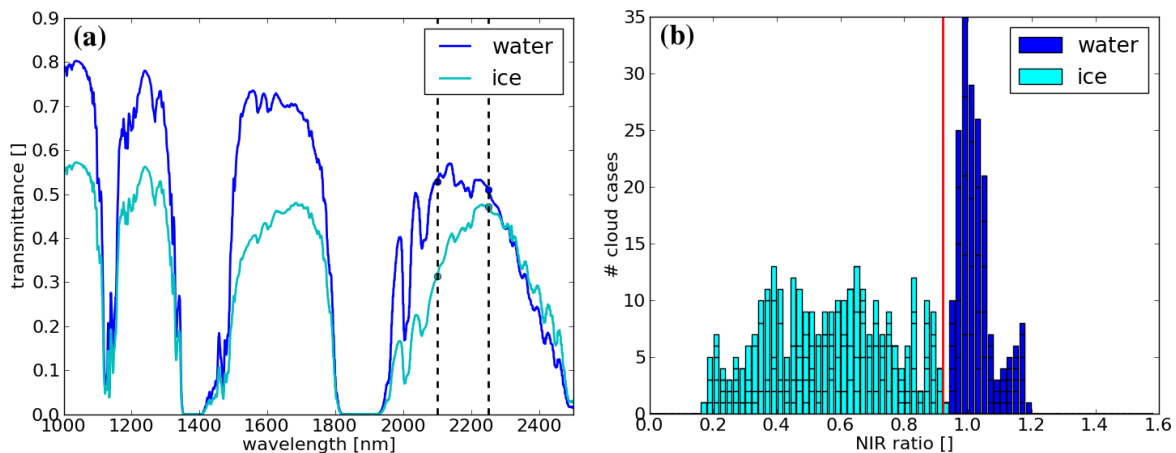


Figure 4.7: (a) Transmittance of a water and an ice cloud with $\tau = 3.0$, $r_{\text{eff}} = 25 \mu\text{m}$, and $\Delta z = 1 \text{ km}$ for $\theta_v = 0^\circ$. (b) NIR ratio for various water ($r_{\text{eff}}: 5 - 30 \mu\text{m}$) and ice ($r_{\text{eff}}: 5 - 90 \mu\text{m}$) clouds with $\tau = 0.5 - 10.0$ and $\theta_v = 0^\circ - 8^\circ$ (all simulations for $\theta_0 = 32^\circ$, $\phi_{\text{rel}} = 180^\circ$, Baum-modified mixture).

Figure 4.7a shows an example of cloud transmittances for liquid and solid phase clouds in the SWIR spectral range. The transmittance of ice particles rises strongly from 2.1 to 2.25 μm , as absorption decreases in this spectral range. In contrast, the water cloud transmittance changes only slightly due to a nearly constant absorption coefficient in the same spectral range.

This example leads to the assumption that the same phase detection approach as proposed by Martins et al. (2011) for reflectances may be applied to cloud transmittances. Consequently, a *NIR ratio* is defined as the ratio of the transmittance at 2.1 μm to the transmittance at 2.25 μm : $I_{\text{NIR}} = T_{2.1\mu\text{m}}/T_{2.25\mu\text{m}}$. Figure 4.7b shows NIR ratios computed for an exemplary collection of water and ice clouds (optical depths in range 0.5 - 10.0, effective radii of 5 - 30 μm for water droplets and 5 - 90 μm for ice particles in Baum-modified mixture). As can be seen in this figure, the NIR ratio is generally smaller for ice clouds than for water clouds.

A phase distinction seems to be possible applying a NIR ratio threshold of 0.92. For $I_{\text{NIR}} < 0.92$ an ice cloud is detected while for $I_{\text{NIR}} \geq 0.92$ a water cloud is detected. Certainly, this threshold varies with the assumed ice particle habit and viewing geometry. Several examples show a good performance of this method with the chosen threshold, also for different habits. False phase detection occurs primarily for cases with small cloud optical thickness ($\tau < 1$).

4.3 Retrieval of cloud optical thickness and effective radius

Nakajima-King retrieval

The retrieval of ice cloud radiative properties developed in this study is based on the well established cloud retrieval of Nakajima and King (1990). According to this fundamental work, water cloud optical thickness and effective radius can be derived simultaneously from satellite data. For this purpose, the information content of reflectances at two wavelength bands is combined: a band in the VNIR spectral region (usually 0.66 or 0.75 μm) and a band in the shortwave infrared region (e.g. 1.6, 2.1, or 3.7 μm). The former is dominated by cloud particle scattering and is mainly sensitive to cloud optical thickness. In contrast, the latter is also influenced by cloud particle absorption and contains information on particle size. This relation is caused by the fact that the SWIR reflection function strongly depends on the photon absorption probability for a cloud droplet, which is in turn proportional to the droplet effective radius (Kokhanovsky, 2004). This method is referred to as *Nakajima-King retrieval* in the following. Figure 4.8a shows the diagram established by Nakajima and King which allows a widely unambiguous assignment of τ and r_{eff} to a bi-spectral reflected radiance pair. By radiative transfer simulations a lookup table (LUT) of cloud reflectances and corresponding cloud properties can be generated and the comparison to measured reflectances reveals the retrieved optical thickness and particle size.

In this study, the Nakajima-King retrieval introduced above is adapted to ground-based measurements of ice cloud transmittance. Remote sensing of radiative properties of ice clouds is complicated due to their low optical thickness (usually smaller than 5), the nonspherical particle shape and the possible horizontal particle orientation (Kokhanovsky, 2004). Particle orientation is not considered here and randomly orientated particles are assumed in this study.

The dependency of ice cloud transmittance on optical thickness is illustrated in figure 4.6a while in figure 4.6b the dependency on effective particle size is shown. Similar to the case of reflectances explained above, transmittances are most sensitive to optical thickness in the visible spectral region and to effective particle size in the SWIR spectral region. Figure 4.8b indicates that a combination of transmittances at 550 nm and 1600 nm allows to draw a diagram analogous to the one of Nakajima and King. In the case of transmittances, a wide range of the diagram is not unambiguous anymore as transmittances first increase and then decrease with increasing optical thickness. This ambiguity, introduced by applying a Nakajima-King-like method to transmittances, has to be accounted for in the ice cloud retrieval as explained below.

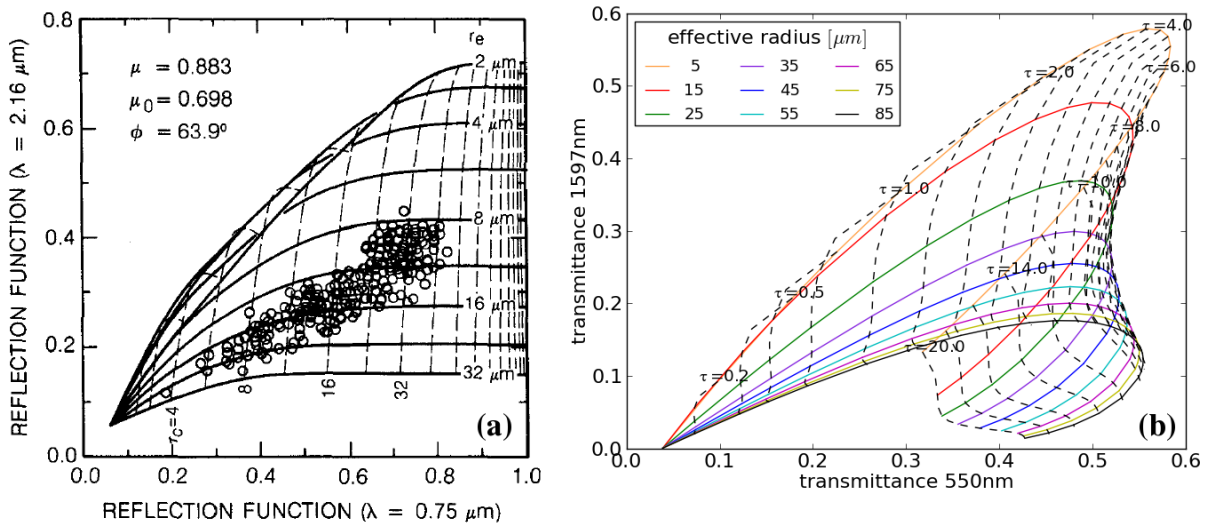


Figure 4.8: Qualitative comparison of lookup tables for reflectances and transmittances: **(a)** LUT for reflectances (Nakajima and King, 1990), **(b)** LUT for transmittances at 550 and 1600 nm simulated for $\theta_0 = 36^\circ$, $\theta_v = 0^\circ$, $\phi_{rel} = 180^\circ$, and Baum-modified mixture.

VIS-slope method

A criterion has to be found to separate the overlapping regimes of optical thickness in figure 4.8b and consequently resolve the inherent ambiguity. An important factor in distinguishing cloud optical thickness is color. As optically thin clouds are quite transparent, the dominance of short-wave “blue” components of Rayleigh scattering is visible through them. In contrast, optically thicker clouds are more opaque implying a “grey” spectrally invariant appearance. An objective measure for this color is the slope of transmittance spectra in the visible spectral range. Small optical thickness is associated to a negative slope (high fraction of blue), while larger optical thickness exhibits a neutral or positive slope (low fraction of blue).

Figure 4.9a indicates these spectral slopes as thick lines in the transmittance spectra for several values of optical thickness. This spectral slope in the visible spectral range allows to separate the overlapping parts in figure 4.8b resulting in two widely unambiguous parts of the lookup table shown in figure 4.9b. Consequently, a bi-spectral transmittance pair can be related to a single combination of τ and r_{eff} after splitting the lookup table by the described approach, referred to as *VIS-slope method* in the following.

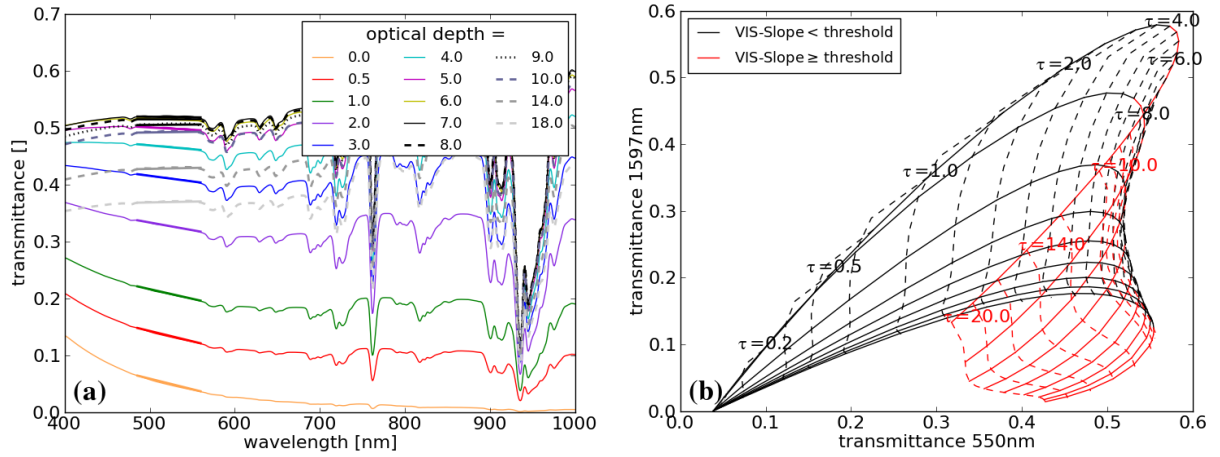


Figure 4.9: (a) VNIR transmittance spectra for various τ , thick lines show linear regression for S_{VIS} in 485 - 560 nm ($r_{\text{eff}} = 30 \mu\text{m}$). (b) Separation of optical thickness regimes by VIS-slope method (simulated for $\theta_0 = 36^\circ$, $\theta_v = 0^\circ$, $\phi_{\text{rel}} = 180^\circ$, and Baum-modified mixture).

The criterion used for splitting the lookup table is the spectral slope S_{VIS} in the range of 485 nm to 560 nm. For each simulated or measured spectrum S_{VIS} is obtained according to the formula

$$S_{\text{VIS}} = \frac{100}{T(550\text{nm})} \cdot \left. \frac{dT(\lambda)}{d\lambda} \right|_{\lambda_a}^{\lambda_b} \quad (4.3)$$

where the derivative of transmittance is computed by linear regression from $\lambda_a = 485 \text{ nm}$ to $\lambda_b = 560 \text{ nm}$ normalized by the transmittance at 550 nm. The wavelength range for the calculation of S_{VIS} is chosen because (1) it is part of the visible spectrum which is sensitive to optical thickness, (2) it exhibits a smooth spectral dependence which allows the determination of a slope, and (3) it is not too close to the lower boundary of spectral sensitivity of specMACS (see discussion in section 3.1).

To separate the two ambiguous optical thickness regimes by the suggested VIS-slope method, it would be necessary to find a spectral slope threshold S_{crit} . For spectra with $S_{\text{VIS}} < S_{\text{crit}}$ transmittances increase with increasing optical thickness (low τ regime), while for $S_{\text{VIS}} \geq S_{\text{crit}}$ transmittances decrease with optical thickness (high τ regime). Generally, S_{crit} would be a function of the sensor-sun-cloud geometry, the particle habit, and the effective size.

In a first approach to find such a threshold, the turning point of the transmittance trend could be determined as the maximum of $T(550\text{nm})$ for clouds with varying optical thickness for a given geometry, habit and effective radius. Then, the slope $S_{\text{VIS}}(r_{\text{eff}})$ of the corresponding spectrum would be computed as function of the considered effective radius. As r_{eff} is not known in advance, these thresholds had to be averaged over all simulated effective radius values. Finally, a threshold S_{crit} could be obtained for each considered θ_0 , θ_v , ϕ_{rel} , and habit assumption which separates the corresponding lookup table in two almost unambiguous parts (cf. figure 4.9b). To illustrate the characteristics of these thresholds, figure 4.10 shows spectral slopes for various solar zenith angles, effective radius and optical thickness values. The threshold S_{crit} averaged over all effective radii, determined as explained above, is indicated as red line in each case.

As can be seen in figure 4.10, S_{VIS} stays nearly constant with increasing effective radius at a certain optical thickness for $r_{\text{eff}} > 20 \mu\text{m}$. In contrast, S_{VIS} changes sharply with decreasing effective radius for $r_{\text{eff}} < 20 \mu\text{m}$ in most displayed cases. Due to this effect, the threshold S_{crit} (red lines) separates the two optical thickness regimes accurately for large effective radii, while problems occur for $r_{\text{eff}} < 20 \mu\text{m}$. The different behavior of S_{VIS} for $r_{\text{eff}} < 20 \mu\text{m}$ can be explained by the small size parameter x corresponding to these r_{eff} values in the considered wavelength range (400 - 2500 nm). For size parameters of $x > 30$ ($r_{\text{eff}} > 15 \mu\text{m}$) the extinction efficiency may be approximated by $Q_{\text{ext}} \approx 2$. In contrast, Q_{ext} cannot be assumed constant for smaller x (see fig. 2.15), implying that extinction varies with size parameter. Additionally, this threshold method is problematic for scattering angles near the halo, as can be seen in fig. 4.10 for $\theta_0 = 44^\circ$ (close to the 46° halo). It follows that the described approach to separate the two optical thickness regimes by determining a threshold S_{crit} suffers from several issues. Therefore, a different approach is introduced in the next section, which avoids these issues.

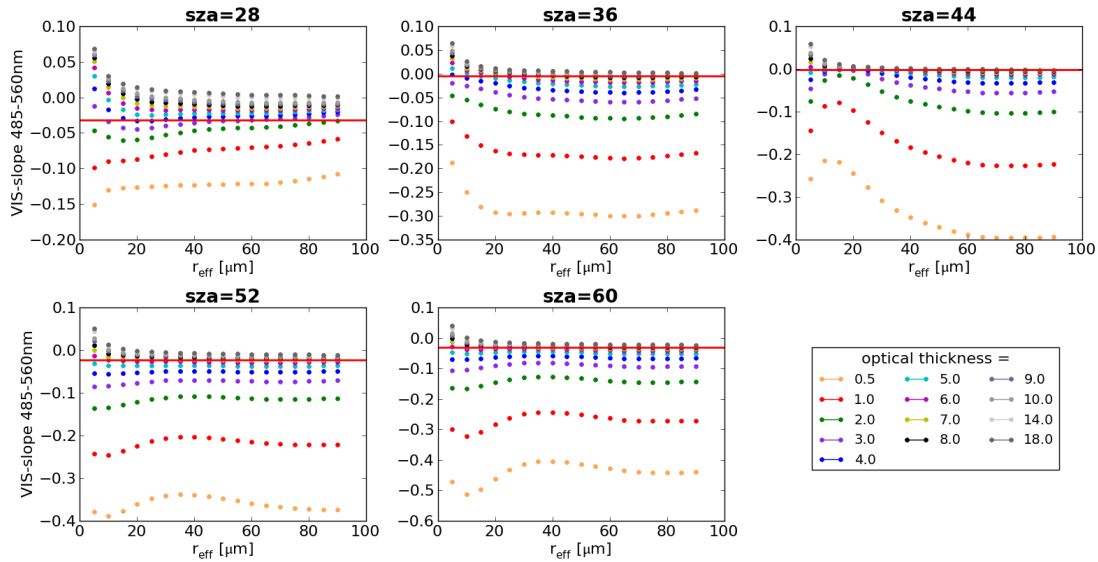


Figure 4.10: S_{VIS} for various r_{eff} , τ , and solar zenith angles ($\text{sza} \equiv \theta_0$). Thresholds S_{crit} averaged over effective radii marked as red lines ($\theta_v = 0^\circ$, $\phi_{\text{rel}} = 180^\circ$, Baum-modified mixture).

3D retrieval method

An alternative to the threshold method, discussed above, exploits the information of the spectral slope S_{VIS} without setting a threshold S_{crit} . This can be achieved by adding a third dimension to the lookup table which contains the information about the visible spectral slope S_{VIS} computed for each simulated spectrum in the lookup table. Figure 4.11 illustrates this 3D approach, which resolves the ambiguity in the conventional transmittance-based 2D lookup table. The transmittances at 550 nm and 1600 nm are plotted on the x-axis and the y-axis as before, and now additionally the spectral slope S_{VIS} is plotted on the z-axis. In this 3D diagram the simulated points span a nonintersecting surface, as points associated to larger optical thickness values are shifted to larger spectral slope values along the z-axis. Consequently, it is possible to unambiguously match a pair of optical thickness and effective radius to a measured transmittance spectrum in

the 3D lookuptable. As most realistic guess for the ice crystal shape the Baum-modified habit mixture is assumed. The 3D retrieval method is performed in the following three steps:

1. Determination of the distance to all points in the lookup table
2. Selection of a subset of close points in the lookup table
3. Calculation of a weighted average over the points in this subset

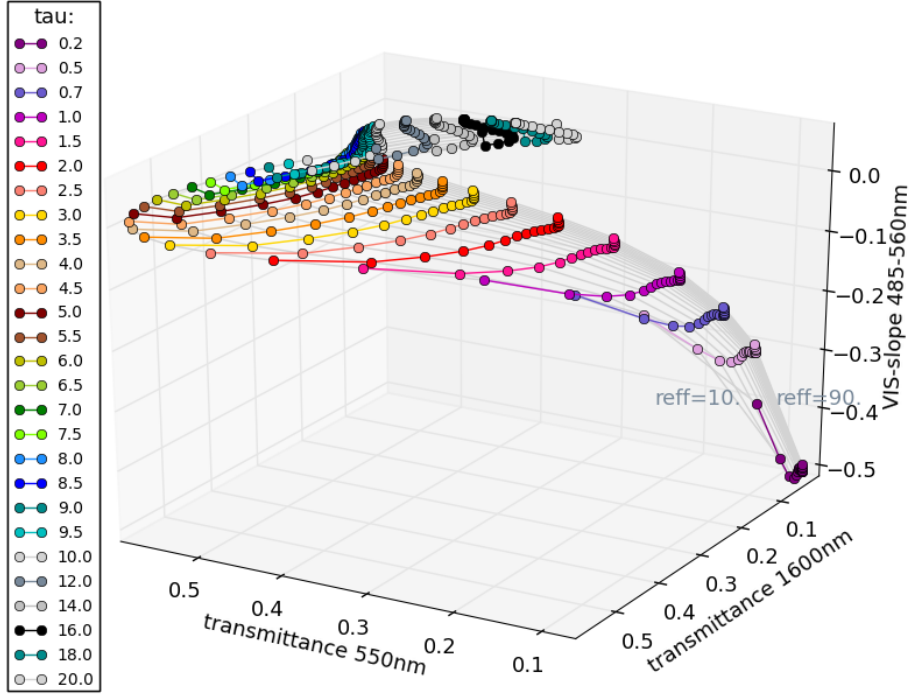


Figure 4.11: 3D lookup table using transmittances at 550 nm and 1600 nm and the spectral slope S_{VIS} in 485 - 560 nm (simulation for $\theta_0 = 36^\circ$, $\theta_v = 0^\circ$, $\phi_{rel} = 180^\circ$, and Baum-modified mixture).

In the first retrieval step, the distance $R_{LUT,i}$ to point i in the lookup table is calculated as

$$R_{LUT,i} = \sqrt{(T_{550} - T_{550,i})^2 + (T_{1600} - T_{1600,i})^2 + (S_{VIS} - S_{VIS,i})^2} \quad (4.4)$$

with the transmittance T_{550} at 550 nm, the transmittance T_{1600} at 1600 nm, and the visible spectral slope S_{VIS} , each for the input data as well as for point $i = 1, \dots, M$ in the lookup table.

In the second step, a subset of the whole lookup table is chosen including only points with a distance $R_{LUT,i} < 0.2$. This is equivalent to assigning a weight $w_i = 0$ to points with $R_{LUT,i} \geq 0.2$ in the further analysis. In the third step, the effective radius is retrieved by taking a weighted average over N points in the chosen lookup table subset:

$$r_{\text{eff,ret}} = \frac{\sum_{i=0}^N w_i r_{\text{eff},i}}{\sum_{i=0}^N w_i} \quad \text{with } w_i = \begin{cases} 1/R_{LUT,i}^4 & \text{if } R_{LUT,i} < 0.2 \\ 0 & \text{if } R_{LUT,i} \geq 0.2 \end{cases} \quad (4.5)$$

Similarly, the optical thickness is derived as

$$\tau_{ret} = \frac{\sum_{i=0}^N w_i \tau_i}{\sum_{i=0}^N w_i} \quad \text{with } w_i \text{ as in eq. 4.5} \quad (4.6)$$

The weighting factors of $1/R_{LUT}^4$ can be understood by considering a 3D space filled with uniformly distributed points. The number of points, contributing to the weighted average, increases proportional to the infinitesimal volume element $dV = 4\pi R_{LUT}^2 dR_{LUT}$ with increasing distance dR_{LUT} . To account for this factor of R_{LUT}^2 , the weight for each point has to be at least $1/R_{LUT}^3$. For even more emphasis on close points a weight of $w = 1/R_{LUT}^4$ is chosen for points with a distance $R_{LUT} < 0.2$. In the case considered here, the points are not uniformly distributed, but approximately span a 2D area, which could introduce a bias in the weighted average to areas with larger point density in the lookup table.

The described 3D retrieval relies on a lookup table appropriate for the analyzed data. For measurements with solar and viewing zenith angles that are not included in the simulated lookup tables, this appropriate lookup table results from the interpolation of lookup tables for the closest simulated solar zenith angles θ_0 and viewing zenith angles θ_v . The elements of these ‘‘closest’’ lookup tables (T_{550} , T_{1600} , and S_{VIS}) are interpolated with respect to scattering angle. Therefore, the scattering angles are computed for the measurement and the closest two simulated θ_0 and four θ_v included in the lookup tables. Then, the Lagrange interpolation polynomial is calculated through the points of two 1-D arrays, i.e. the scattering angle and the transmittance or spectral slope. Consequently, an interpolated lookup table is obtained which is appropriate for the given θ_v , θ_0 and ϕ_{rel} of the measurement. In this interpolated 3D lookup table the retrieval procedure is performed as explained above. The number of four θ_v for interpolation is chosen to obtain smooth retrieval results in the application to a whole measurement scene (e.g. figure 5.15). If only two θ_v are considered in the interpolation, sharp boundaries occur in the retrieved scene at certain scattering angles.

Two possible conditions lead to an abort of the retrieval algorithm: either a measurement is classified as liquid phase cloud by the NIR-ratio method (see section 4.2) or not enough points are found in the lookup table to compute a meaningful weighted average. The latter case occurs by definition if only one or no point with a distance smaller than 0.2 is found in the searched lookup table, referred to as ‘‘lack of points’’ in the subsequent analysis. The former case is either a correct detection of a liquid water cloud pixel in the measurement or a shortcoming of the applied phase detection method and therefore a misclassification of the considered spectrum, referred to as ‘‘water detection’’ in the following. In both of these cases, the concerned retrieval instance is excluded from sensitivity studies or marked as invalid pixel in the retrieval application to measurements.

In the following chapter, the developed retrieval method is applied to synthetic observations in order to test the method and reveal its sensitivity to various uncertainties (section 5.1). In a final step, first cirrus transmittance measurements with the spectrometer specMACS are analyzed in section 5.2 using the proposed retrieval algorithm.

Chapter 5

Applications

5.1 Sensitivity studies with synthetic observations

In order to learn more about the uncertainties inherent to the newly developed retrieval method, test cases of simulated cirrus transmittance spectra are utilized as input to the retrieval. In contrast to real measurements, for these *synthetic observations* the underlying cloud parameters are known and represent the “true” cloud properties, i.e. the desired retrieval result. Consequently, the retrieved quantities and the corresponding cloud parameters of the input spectra may directly be compared to quantify the retrieval error.

A usual way to specify the retrieval error is the *bias* B which is defined as the mean difference between the retrieved quantity x_{ret} and the “true” input quantity x_{true} :

$$B_x = \langle x_{\text{ret}} - x_{\text{true}} \rangle \quad (5.1)$$

Here $\langle \dots \rangle$ indicates the average over all performed retrieval instances and x represents either the cloud optical thickness τ or the effective radius r_{eff} resulting in a bias B_τ or B_r , respectively.

Another way to quantify the retrieval accuracy is by means of the *root mean square error* R

$$R_x = \sqrt{\langle (x_{\text{ret}} - x_{\text{true}})^2 \rangle} \quad (5.2)$$

where x again stands either for τ or for r_{eff} yielding a root mean square error R_τ for the optical thickness or R_r for the effective radius. For unbiased data, R is the square root of the variance, equivalent to the standard deviation.

A third measure of retrieval performance applied in the following analysis is the *false detection rate* F . It is defined as the percentage of “errors” in the total number of performed retrievals. A retrieval case is perceived as “error” if the deviation between retrieved and true quantity is larger than a critical value ($|\Delta r_{\text{eff}}| > 5 \mu\text{m}$, $|\Delta\tau| > 1$) corresponding to the lookup table resolution.

In the following sections, the introduced measures of retrieval error are used to determine the retrieval sensitivity to the employed interpolation methods, the scattering angle, the assumption of ice crystal habit and aerosol concentration, the instrument noise, and the uncertainty in determining the viewing zenith angle during measurements.

5.1.1 Test spectra included in the lookup table

As a first function test of the retrieval, it is applied to spectra which are part of the lookup table for the Baum-modified habit mixture (clear sky case $\tau = 0$ is excluded). In this case, the retrieval exactly reproduces the cloud properties used for the simulation of these lookup table spectra. Consequently, the bias, the root mean square error (RMSE) and the false detection rate assume a value of zero as illustrated in figure 5.1. The cloud phase determination method (cf. section 4.2) correctly detects ice clouds in most cases but misclassifies 113 of 48600 test spectra as liquid phase clouds.

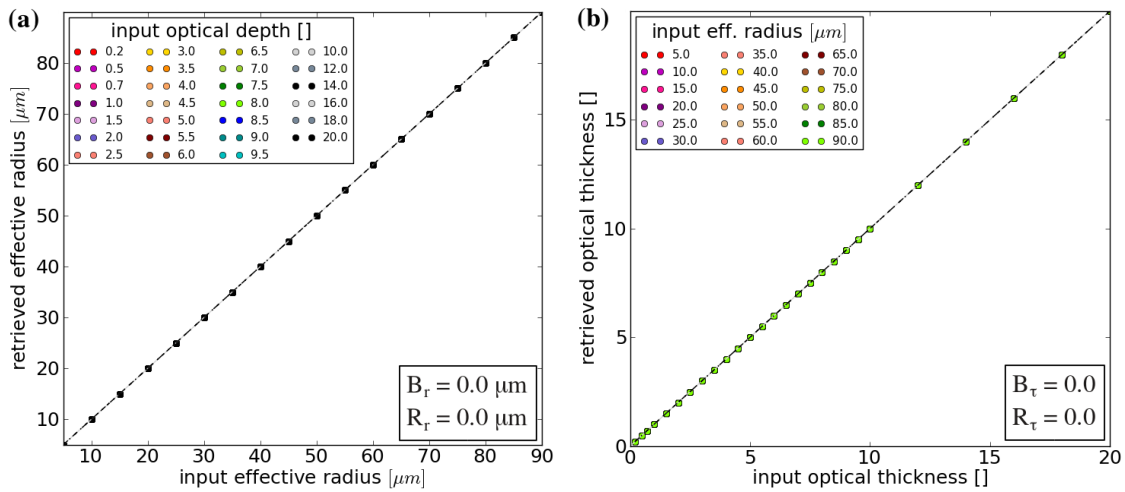


Figure 5.1: Retrieval test with input spectra included in the lookup table for Baum-modified mixture. Scatterplot for (a) the effective radius retrieval and (b) the optical thickness retrieval.

As in figure 5.1, the retrieval performance in each of the following sensitivity studies is illustrated in terms of a scatterplot. These scatterplots show the “true” versus the retrieved effective radius (left panels) and optical thickness (right panels). If the points lie exactly on the diagonal as in figure 5.1 the retrieval resembles the truth of the test spectra accurately. If, on average, the points deviate from the diagonal in a certain direction, the retrieval bias is nonzero. The dashed line in the scatterplots indicates the bias as function of the particular test quantity while the surrounding dotted lines indicate the corresponding root mean square errors (not visible in fig. 5.1). Bias and RMSE calculated for the whole set of test cases are presented in a text box for each scatterplot. For reasons of clarity, the colored points are not shown for the entire set of test cases, but only for an exemplary subset as described in each of the following tests. The points’ color gives information either about the input optical thickness value or the input effective radius value.

Beside RMSE, bias, and false detection rate, two further parameters explained in the previous section are discussed in the following: the frequency of water detection, when a test case is misclassified as liquid phase spectrum and the frequency of cases where not enough points are found in the lookup table (lack of points).

5.1.2 Sensitivity to the interpolation of r_{eff} and τ in the lookup table

In a second step of retrieval testing, the test spectra are simulated for values of effective radius and cloud optical depth that are not part of the lookup tables. In this case, the retrieval result is obtained by interpolation between points in the lookup table which introduces a degree of uncertainty in the retrieval. To quantify this uncertainty, the retrieval is applied to a set of simulated spectra for 23 randomly chosen τ in the range 0.1 - 19.2 and 18 randomly chosen r_{eff} in the range 6 - 89 μm assuming the Baum-modified habit mixture. This set is simulated for 20 geometries that are included in the lookup tables, i.e. solar zenith angles $\theta_0 = [32^\circ, 40^\circ]$, relative azimuth angles $\phi_{\text{rel}} = [0^\circ, 180^\circ]$, and viewing zenith angles $\theta_v = [0^\circ, 2^\circ, 4^\circ, 6^\circ, 8^\circ]$. For the described sample of 8280 test clouds the retrieval performance is illustrated in figure 5.2 with colored points exemplarily depicted for $\theta_0 = 32^\circ$, $\theta_v = 0^\circ$, and $\phi_{\text{rel}} = 180^\circ$.

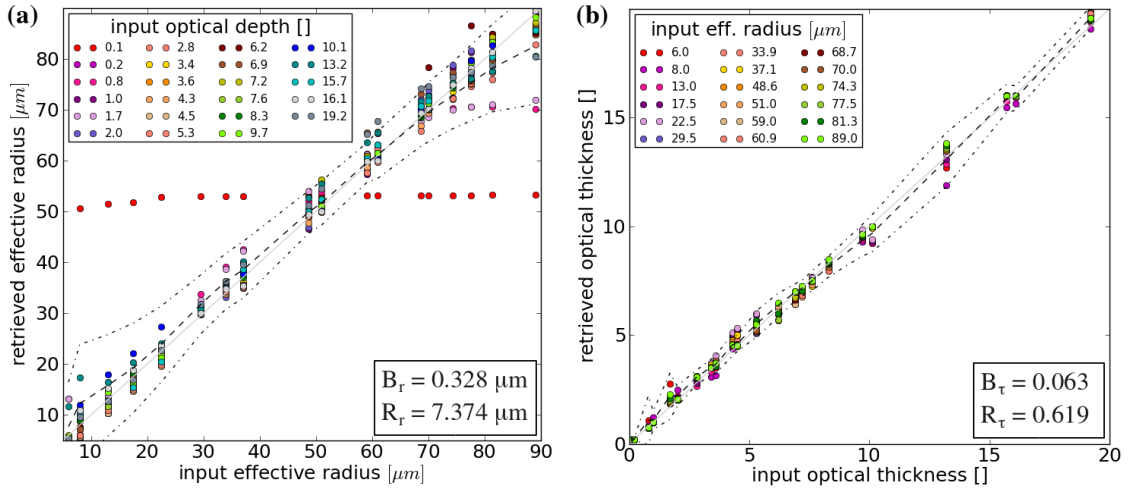


Figure 5.2: Sensitivity to interpolation in the LUT: test spectra for randomly chosen values of r_{eff} (6 - 89 μm) and τ (0.1 - 19.2) for Baum-modified mixture. Scatterplot for (a) the effective radius retrieval and (b) the optical thickness retrieval with points shown for $\theta_0 = 32^\circ$, $\theta_v = 0^\circ$, $\phi_{\text{rel}} = 180^\circ$.

In this case, the retrieval performs as follows:

- effective radius retrieval: $B_r = 0.328 \mu\text{m}$, $R_r = 7.374 \mu\text{m}$
- optical thickness retrieval: $B_\tau = 0.063$, $R_\tau = 0.619$
- false detection rate: $F = 16.98\%$ (1398 in 8233 test cases)
- water detection: 45 cases
- lack of points: 2 cases

Figure 5.2 shows large deviations in the retrieved effective radius values for synthetic observations with $\tau = 0.1$. This optical thickness is smaller than the lowest value $\tau_{\text{min}} = 0.2$ in the lookup table and therefore the interpolation between points in the lookup table is incorrect. To retrieve properties for clouds with $\tau < 0.2$, the lookup tables would have to be extended to smaller optical depths, but the sensitivity to aerosol would grow significantly. In the following studies test spectra with $\tau = 0.1$ are excluded and 22 cases of optical thickness in the range of 0.2 - 19.2 remain for testing.

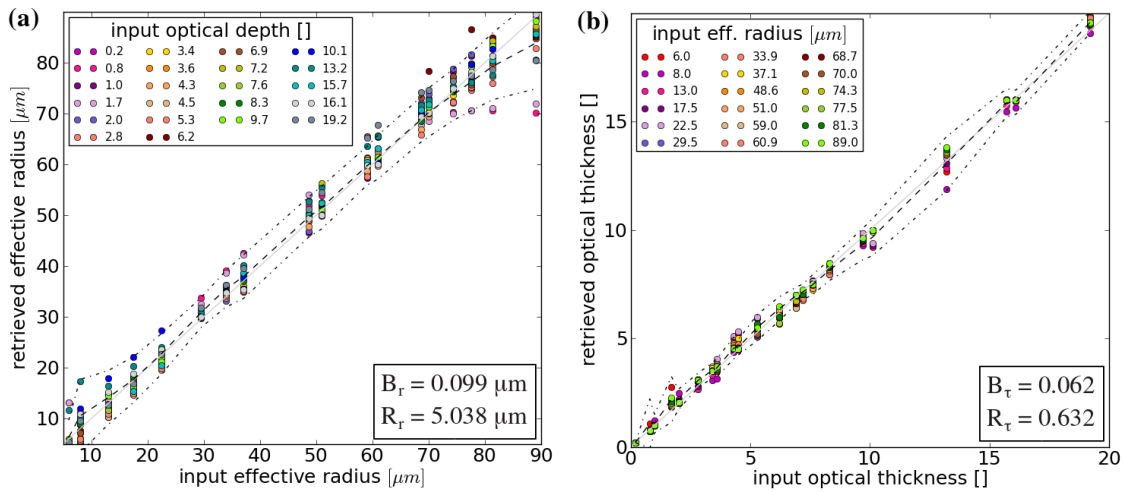


Figure 5.3: Sensitivity to interpolation in the LUT: details as in figure 5.2, but $\tau = 0.1$ excluded.

Compared to the results including $\tau = 0.1$ shown above, now for the remaining 7920 cases the resulting errors are smaller (see figure 5.3):

- effective radius retrieval: $B_r = 0.099 \mu\text{m}$, $R_r = 5.038 \mu\text{m}$
- optical thickness retrieval: $B_\tau = 0.062$, $R_\tau = 0.632$
- false detection rate: $F = 13.91\%$ (1099 in 7900 test cases)
- water detection: 20 cases, lack of points: 0 cases

The interpolation of effective radius and optical thickness in a lookup table introduces a very small bias in the retrieval which increases for small and large effective radius values as can be seen in figure 5.3. Small r_{eff} tend to be overestimated while large r_{eff} tend to be underestimated. The optical thickness retrieval likewise shows a very small bias. The calculated RMSE R_r and R_τ are comparable in size to the resolution of the lookup table.

5.1.3 Sensitivity to the interpolation of θ_0 and θ_v

Beside the interpolation of r_{eff} and τ within a lookup table, interpolation is necessary between different lookup tables if the test case geometry is not included in the simulations. As explained in section 4.3, the lookup table points are interpolated to the scattering angle associated with θ_0 , θ_v , and ϕ_{rel} of the test case.

To examine the uncertainties introduced by this interpolation, the retrieval is applied to test spectra simulated for seven solar zenith angles in the range $25^\circ - 57^\circ$, five viewing zenith angles in the range $1.5^\circ - 6.2^\circ$, and two relative azimuth angles (0° , 180°). Cloud parameters are chosen as described in the previous test (22 τ , 18 r_{eff} , Baum-modified mixture). For these 27720 test cases the retrieval results are summarized in the left column of table 5.1 and illustrated in figure 5.4, where colored points are shown for an exemplary geometry of $\theta_0 = 31.0^\circ$, $\theta_v = 1.5^\circ$, and $\phi_{\text{rel}} = 180^\circ$. Now the retrieval uncertainties are caused by the interpolation between lookup tables as well as by the weighted average in the interpolated lookup table.

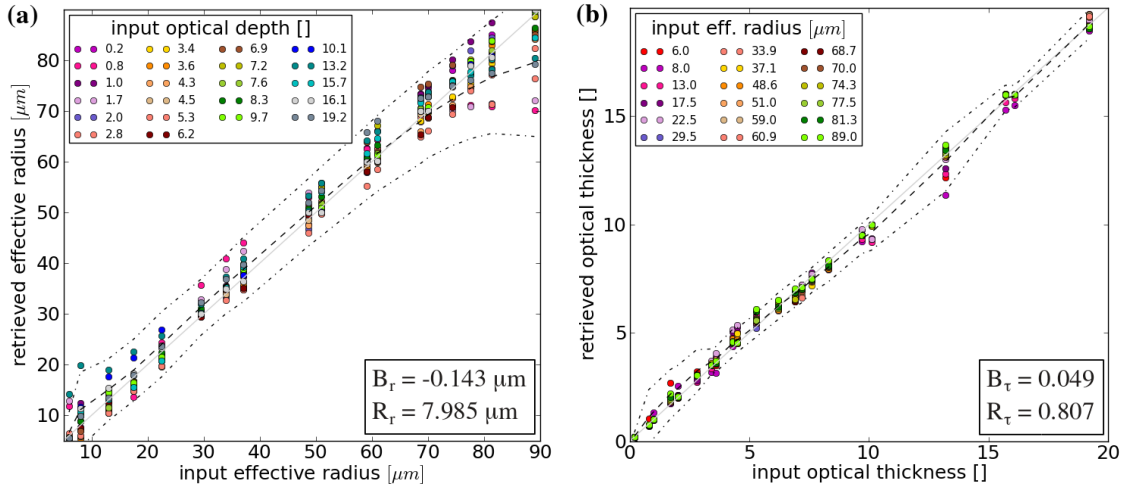


Figure 5.4: Sensitivity to interpolation of θ_0 and θ_v (ϕ_{rel} given): test values of θ_0 , θ_v , r_{eff} , and τ are not part of the lookup table (Baum-modified mixture). Scatterplot for (a) the effective radius retrieval and (b) the optical thickness retrieval with points shown for $\theta_0=31^\circ$, $\theta_v=1.5^\circ$, and $\phi_{\text{rel}}=180^\circ$.

	all scattering angles	halo region excluded
B_r, R_r [μm]	-0.143, 7.985	0.254, 5.513
B_τ, R_τ []	0.049, 0.807	0.034, 0.463
F [%]	28.29%	19.04%
water detection	20 cases	20 cases
lack of points	67 cases	0 cases

Table 5.1: Retrieval performance for a test with (left column) all scattering angles included and (right column) only test cases with scattering angles outside of the halo region (17° - 27° , 42° - 50°) included (θ_0 , θ_v , r_{eff} , and τ are not part of the lookup table, Baum-modified mixture).

Compared to the previous test (cf. figure 5.3), the bias and RMSE of the effective radius retrieval are increased and now the underestimation of large test r_{eff} values is dominant (negative bias). For the optical thickness retrieval only the RMSE is slightly increased. In several cases not enough points are found in the interpolated lookup table to calculate a weighted average. For certain θ_0 - θ_v - ϕ_{rel} combinations the quality of lookup table interpolation seems to be decreased, especially for small solar zenith angles and corresponding small scattering angles. This implies that the uncertainties caused by the lookup table interpolation are dependent on the considered scattering angle. Figure 5.5 shows the absolute retrieval error in r_{eff} and τ as function of scattering angle for an example of $r_{\text{eff,true}} = 37.1 \mu\text{m}$ and $\tau_{\text{true}} = 3.6$.

Two ranges of scattering angles exhibit relatively large absolute errors which correspond to the regions surrounding the 22° and 46° halo. For scattering angles close to these sharp features in the phase function the interpolation in scattering angle might involve large errors. If scattering angles in these ranges (17° - 27° , 42° - 50°) are excluded from the retrieval test cases, the RMSE and the false detection rate are significantly reduced as compiled in the right column of table 5.1. In contrast, the bias in the effective radius retrieval is increased and shows a trend to slightly overestimate effective radius. For scattering angles outside of the halo region, there is no significant increase of bias and RMSE in this test (interpolation within and between lookup tables) compared to the test in section 5.1.2 (only interpolation within a lookup table).

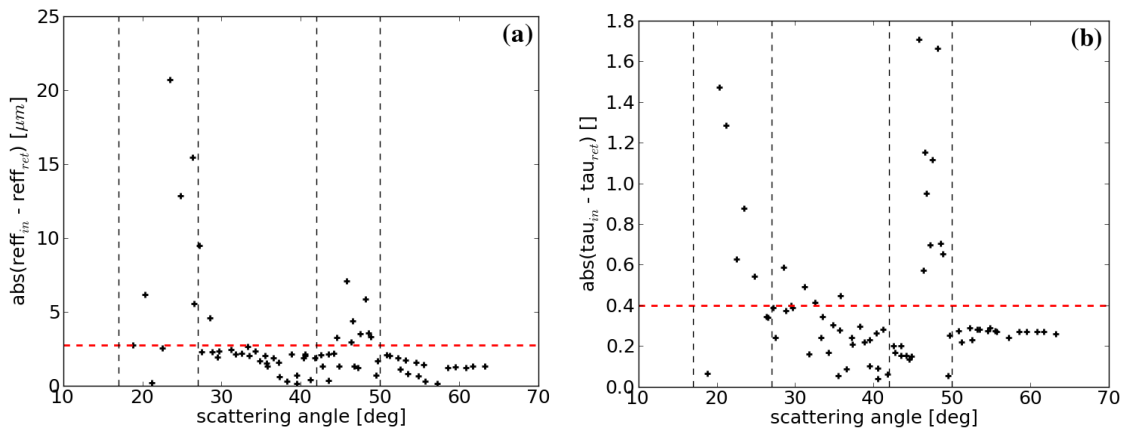


Figure 5.5: Sensitivity to scattering angle: Absolute deviations in the retrieval of (a) effective radius $|r_{eff,true} - r_{eff,ret}|$ and (b) optical thickness $|\tau_{true} - \tau_{ret}|$ as function of Θ_{sca} for $r_{eff,true} = 37.1 \mu m$, $\tau_{true} = 3.6$, and Baum-modified mixture. The red lines indicate the mean absolute deviation.

5.1.4 Sensitivity to the habit assumption

Each ice cloud retrieval is based on various assumptions about particle shape, as only very limited methods for shape determination exist up to now (Comstock et al., 2007). These assumptions introduce a major uncertainty in all ice cloud property retrievals. For example, Key et al. (2002) found differences in the retrieved cirrus optical thickness of more than 50% for various habit assumptions using cloud reflectances measured by satellite sensors. Eichler et al. (2009) studied the influence of shape assumption on the cirrus property retrieval from airborne spectral reflection measurements and determined relative differences of up to 70% in retrieved optical thickness and up to 20% in retrieved effective radius.

A similar analysis is accomplished in this paragraph. The retrieval method is tested for the case that the assumed habit in the retrieval does not match the habit used to simulate the test spectra. To illustrate the arising issues, the retrieval (based on the Baum-modified habit mixture) is applied to test spectra included in the lookup table for 3D bullet rosettes of the HEY parameterization. In this test study, consequently, the only source of retrieval error is the incorrect habit assumption (no interpolation of r_{eff} , τ or Θ_{sca} necessary).

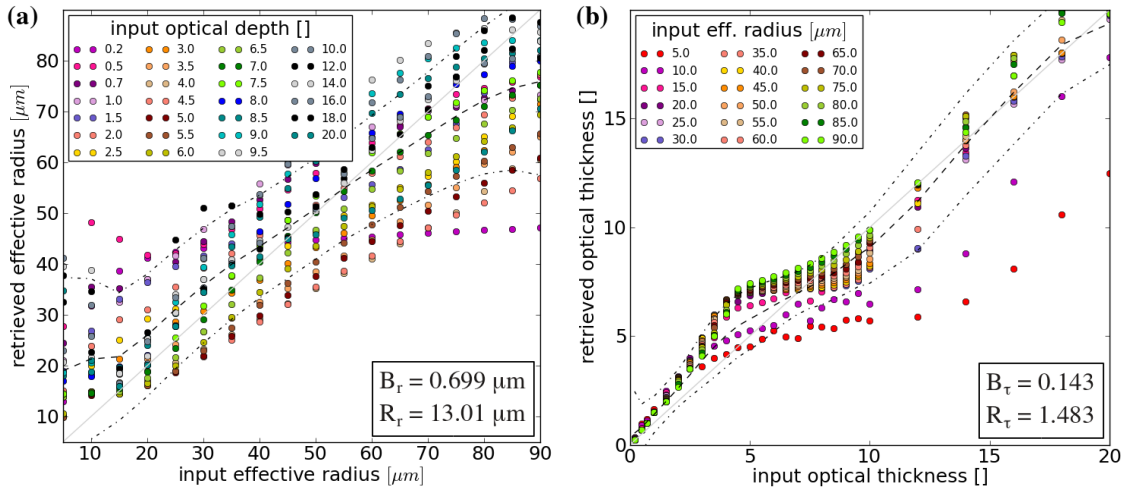


Figure 5.6: Sensitivity to ice crystal habit: test spectra are part of the LUT for bullet rosettes (HEY parameterization), the retrieval assumes the Baum-modified habit mixture. Scatterplot for (a) the effective radius retrieval and (b) the optical thickness retrieval with points shown for $\theta_0 = 36^\circ$, $\theta_v = 0^\circ$, and $\phi_{\text{rel}} = 180^\circ$ (as before dotted lines indicate bias and RMSE calculated for all test cases).

The results are shown in figure 5.6 which can be summarized as follows:

- effective radius retrieval: $B_r = 0.699 \mu\text{m}$, $R_r = 13.006 \mu\text{m}$
- optical thickness retrieval: $B_\tau = 0.143$, $R_\tau = 1.483$
- false detection rate: $F = 62.43\%$ (29594 in 47402 test cases)
- water detection: 588 cases, lack of points: 610 cases

These numbers demonstrate the large uncertainty introduced by a “wrong” habit assumption. The calculated numbers have to be considered as maximum values, as a real cloud usually does not entirely consist of a single habit. Therefore, the retrieval errors due to the habit assumption can be expected to be smaller than the maximum values shown above.

In a next step, the retrieval is applied to the same 27720 test cases as in section 5.1.3, but now they are simulated for each of the six single habits of the HEY parameterization. The Baum-modified habit mixture is assumed in the retrieval as before. In these tests all simulated scattering angles (with the halo region) are included. Now the retrieval uncertainties are caused by three factors: the interpolation of lookup tables to the considered scattering angle, the calculation of a weighted average in the interpolated lookup table, and the habit assumption.

Table 5.2 summarizes the retrieval performance analyzed for the six different habits of the HEY parameterization. As an example, the results for bullet rosettes are shown in figure 5.7 with colored points indicated for an exemplary geometry, while lines represent the bias and RMSE calculated for all 27720 test cases. Compared to the results in section 5.1.3 (see table 5.1, left column), the uncertainties are strongly increased due to the mismatch of habits. The effective radius retrieval exhibits a negative bias in all six tests while the optical thickness retrieval is characterized by a small positive bias in most cases. The negative bias in effective radius is caused by an underestimation of large $r_{\text{eff,true}}$ which dominates over the positive bias (overestimation) for small $r_{\text{eff,true}}$. This effect may be explained by the lower sensitivity to larger effective radius values, i.e. large r_{eff} values are not well separated in the lookup table compared

to smaller ones. Consequently, a small drift in r_{eff} due to taking a weighted average implies a rather large error in retrieved effective radius for large $r_{\text{eff,true}}$ values compared to a smaller error for small $r_{\text{eff,true}}$ values. Especially, large bias occurs in the rough-aggregate case which can be explained by the small contribution of rough-aggregates to the Baum-modified habit mixture. The false detection rates range from 66% to 90% in this habit sensitivity study. Again these numbers are upper limits for the errors, because a real cloud rarely consists exclusively of a single habit, as assumed for the presented simulations.

	B_r, R_r [μm]	B_τ, R_τ []	F [%]
HEY solid column	-5.561, 16.039	1.034, 2.306	82.27
HEY hollow column	-3.653, 15.803	0.400, 1.763	69.35
HEY rough-aggregate	-10.002, 23.237	1.590, 2.987	89.85
HEY bullet rosette	-0.051, 14.433	0.213, 1.815	66.46
HEY plate	-6.669, 25.298	0.229, 3.972	85.77
HEY droxtal	-8.028, 18.222	-0.261, 2.118	66.59

Table 5.2: Bias and RMSE for the retrieval of effective radius (B_r, R_r) and optical thickness (B_τ, R_τ), and false detection rate F in dependence on simulated habit.

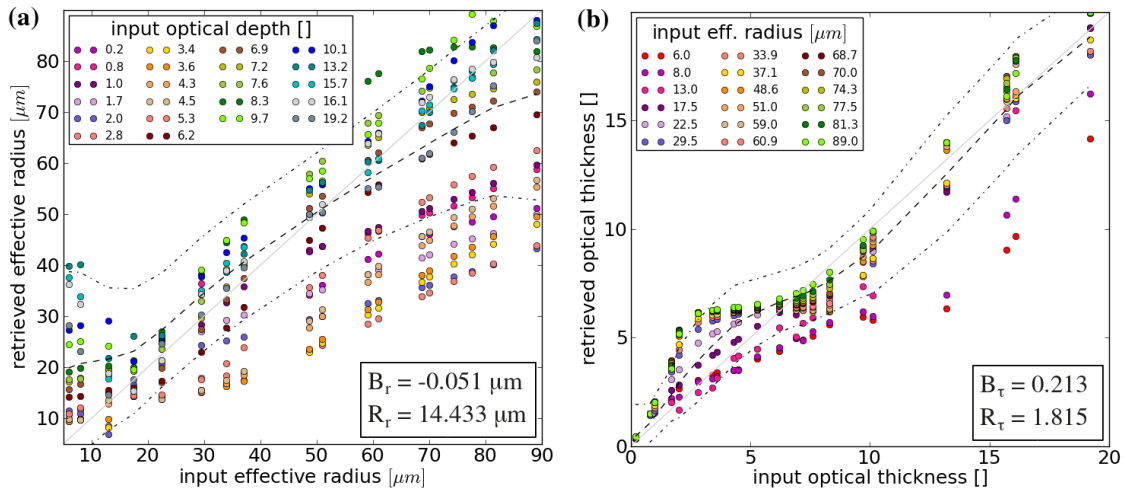


Figure 5.7: Sensitivity to ice crystal habit: test spectra are simulated for HEY bullet rosettes for τ , r_{eff} , θ_0 , θ_v not in LUT; the retrieval assumes the Baum-modified habit mixture. Scatterplot for (a) the effective radius retrieval and (b) the optical thickness retrieval with points shown for $\theta_0 = 31^\circ$, $\theta_v = 1.5^\circ$, $\phi_{\text{rel}} = 180^\circ$ (as before dotted lines indicate bias and RMSE calculated for all test cases).

5.1.5 Sensitivity to the aerosol concentration

Measured transmittance spectra are influenced by the aerosol present at measurement time. This is especially true for measurements and simulations at the location in Munich. In contrast, for measurements at Mount Zugspitze the aerosol concentration may be neglected due to the location above the boundary layer where most aerosol is concentrated.

In order to estimate the retrieval uncertainty evolving from the aerosol concentration, the retrieval is applied to test spectra simulated for continental average aerosol with an aerosol optical thickness of 0.2 at 550 nm, which is a good estimation of the mean AOD in Munich (C. Emde, pers. comm.). Aerosol optical properties are taken from the OPAC library included in libRadtran (Hess et al., 1998). In contrast to the test spectra, the retrieval uses the lookup tables simulated for AOD = 0 in this sensitivity study. The difference in transmittances between these two aerosol cases (AOD = 0.2 versus AOD = 0.0) relative to the no-aerosol case is illustrated in figure 5.8 as function of effective radius and optical thickness for various viewing zenith angles. Generally, the aerosol influence is stronger in the VNIR (solid lines in the figure) than in the SWIR (dashed lines). The depicted difference is particularly large for small τ which limits the retrieval applicability for low τ .

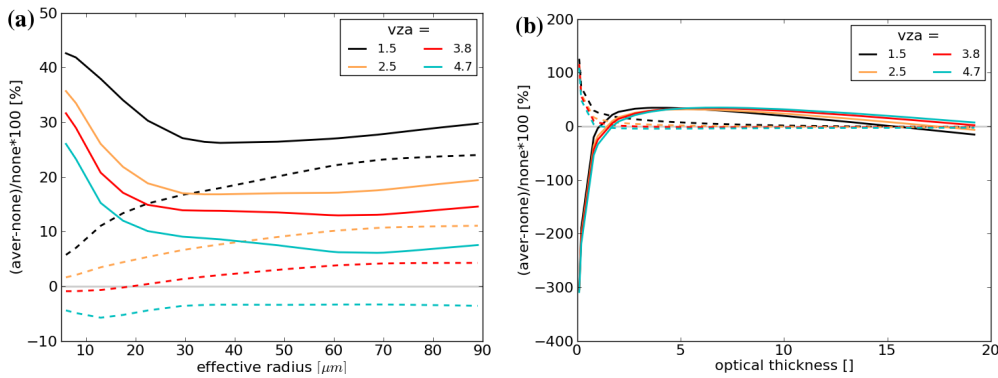


Figure 5.8: Transmittance change [%] due to continental-average aerosol with AOD = 0.2 compared to AOD = 0.0 at 550 nm (solid lines) and 1600 nm (dashed lines). Dependency on (a) effective radius and (b) optical thickness for varying $\theta_v \equiv \text{vza}$, $\theta_0 = 31^\circ$, $\phi_{\text{rel}} = 180^\circ$, and Baum-modified mixture.

In this test, the retrieval is applied to the same 27720 test cases as in section 5.1.3 (τ , r_{eff} , θ_0 , and θ_v are not part of the lookup table; halo region is included), but now they are simulated for an AOD = 0.2. In contrast, the retrieval is based on lookup tables for an AOD = 0.0. The results of this aerosol sensitivity study are illustrated in figure 5.9 and summarized below:

- effective radius retrieval: $B_r = -1.989 \mu\text{m}$, $R_r = 12.737 \mu\text{m}$
- optical thickness retrieval: $B_\tau = 0.573$, $R_\tau = 1.397$
- false detection rate: $F = 52.27\%$ (14276 in 27314 test cases)
- water detection: 61 cases, lack of points: 345 cases

Compared to table 5.1 (left column), all numbers have increased due to the “wrong” aerosol assumption. B_τ is expected to increase by at least 0.2 (offset in AOD). The actual increase is

greater (about 0.5), which is possibly caused by additional uncertainties arising from interpolation and the aerosol influence on the spectral slope S_{VIS} . Large errors in the retrieved effective radius occur especially for small values of τ and r_{eff} (see figure 5.9a), as the influence of the aerosol concentration becomes predominant. Accordingly, bias and RMSE in the optical thickness retrieval increase for small τ_{true} (see figure 5.9b).

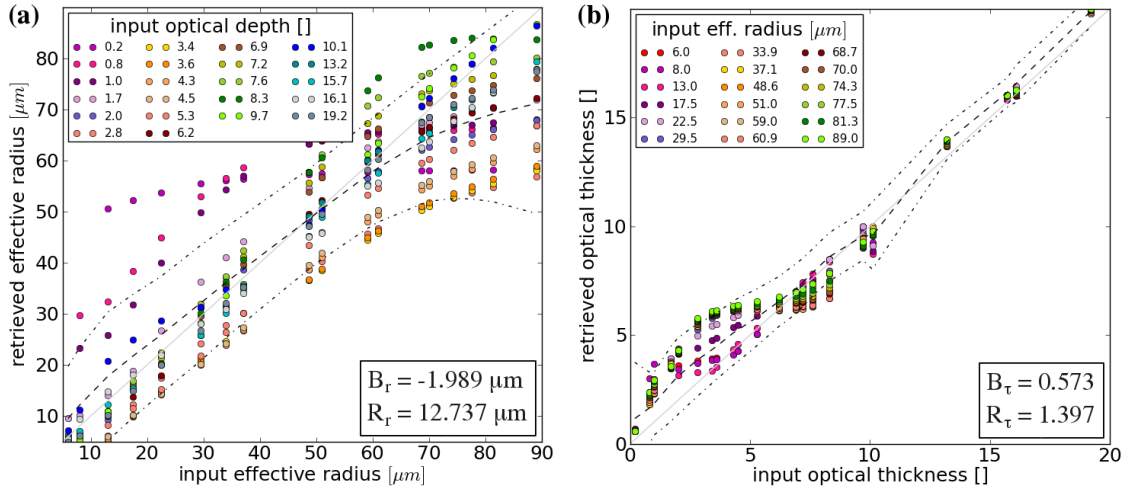


Figure 5.9: Sensitivity to aerosol: test spectra are simulated for continental-average aerosol with AOD=0.2 (τ , r_{eff} , θ_0 , θ_v not in LUT, Baum-modified mixture); retrieval assumes AOD=0.0. Scatter-plot for (a) the effective radius retrieval and (b) the optical thickness retrieval with points shown for $\theta_0 = 31^\circ$, $\theta_v = 1.5^\circ$, $\phi_{rel} = 180^\circ$ (dotted lines indicate bias and RMSE calculated for all test cases).

5.1.6 Sensitivity to instrument noise

Another factor that influences the retrieval is the instrument noise. At maximum signal level the SNR is 800:1 for the SWIR camera of specMACS, while no information on the SNR is provided for the VNIR camera (cf. section 3.1). In order to study the retrieval sensitivity to noise, random noise is added to the spectra with a maximum magnitude of 0.25% of the signal, i.e. for each wavelength a noise between -0.25% and +0.25% is randomly chosen. This corresponds to a SNR of 400:1, which is chosen to estimate the maximum occurring noise influence (SNR at lower signal levels can be larger than at maximum signal level).

The same test as in section 5.1.1 is repeated with test spectra contained in the lookup table but now noise is added as explained above. The resulting error characteristics are as follows:

- effective radius retrieval: $B_r = 0.012 \mu\text{m}$, $R_r = 1.148 \mu\text{m}$
- optical thickness retrieval: $B_\tau = -0.0$, $R_\tau = 0.088$
- false detection rate: $F = 0.98\%$ (473 in 48487 test cases)
- water detection: 113 cases, lack of points: 0 cases

The introduced bias is negligible, but a small RMSE is introduced in the retrieval by the added noise. Quite a large number of cases are detected as water clouds, which could possibly be

avoided by considering a small number of wavelength bands in the NIR-ratio calculation for phase detection (cf. section 4.2).

Repeating the test in section 5.1.3 with noise added to the 27720 test spectra (not part of the lookup table, halo region included) yields the following retrieval errors (see figure 5.10):

- effective radius retrieval: $B_r = -0.142 \mu\text{m}$, $R_r = 8.016 \mu\text{m}$
- optical thickness retrieval: $B_\tau = 0.049$, $R_\tau = 0.808$
- false detection rate: $F = 28.95\%$ (7997 in 27627 test cases)
- water detection: 24 cases, lack of points: 69 cases

The results are illustrated in figure 5.10 with points shown for a geometry of $\theta_0 = 31^\circ$, $\theta_v = 1.5^\circ$, and $\phi_{\text{rel}} = 180^\circ$, while dashed and dotted lines indicate the bias and RMSE for all tested spectra. Compared to the results in section 5.1.3 (table 5.1, left column), the retrieval bias remains unchanged, which is expected as random noise is added. RMSE and false detection rate are increased by a hardly visible amount of $\Delta R_r = 0.031 \mu\text{m}$, $\Delta R_\tau = 0.001$, and $\Delta F = 0.66\%$.

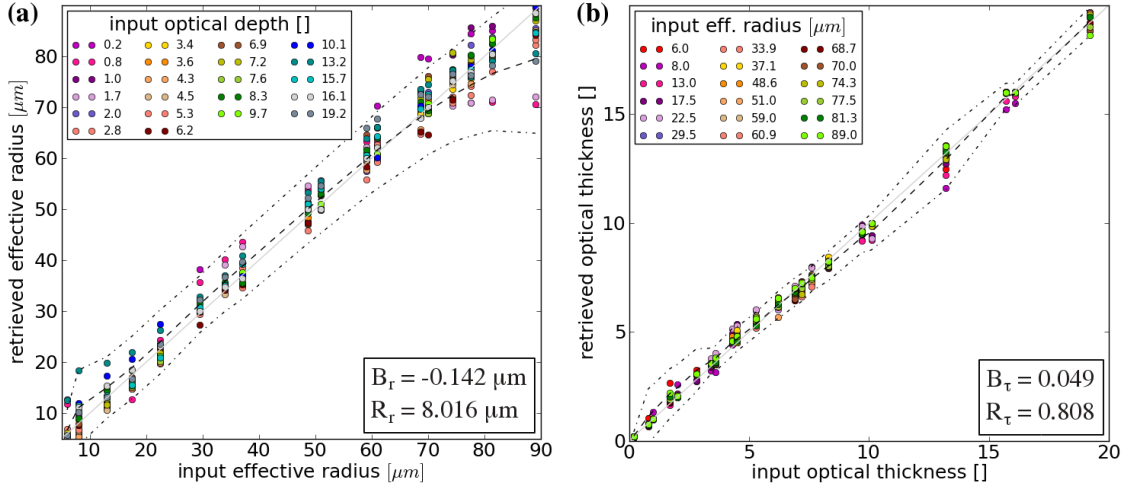


Figure 5.10: Sensitivity to instrument noise: test spectra not included in the LUT with randomly added noise for Baum-modified mixture. Scatterplot for (a) the effective radius retrieval and (b) the optical thickness retrieval with points shown for $\theta_0 = 31^\circ$, $\theta_v = 1.5^\circ$, and $\phi_{\text{rel}} = 180^\circ$.

5.1.7 Viewing angle uncertainty

Measurements in the current setup of specMACS involve the determination of the viewing zenith angle by manual alignment to the sun. From the relative alignment the absolute viewing angle can be determined as the sensor platform is horizontally justified and the absolute sun position may be calculated, e.g. with the zenith tool in libRadtran. This relative alignment introduces another source of uncertainty in the retrieval due to the following aspects:

- error in sun alignment $\Delta\Phi = \pm 0.1^\circ$
- error in determination of alignment time $\Delta\Phi = \pm 0.1^\circ$
- encoder accuracy $\Delta\Phi = \pm 0.01^\circ$

- accuracy of horizontal adjustment of the sensor mount $\Delta\Phi = \pm 0.5^\circ$
- error in determination of the zenith (with water level) $\Delta\Phi = \pm 0.2^\circ$

All these errors contribute to the viewing angle uncertainty which amounts to a maximum value of $\Delta\Phi_{\max} = \pm 1.0^\circ$. This value will usually be smaller, approximately one third of the maximum ($\Delta\Phi_{\max} = \pm 0.3^\circ$). This uncertainty influences the zenith viewing angle θ_v as well as the azimuth viewing angle and therefore ϕ_{rel} of the sensor. Additionally, an error is introduced in the retrieval due to the movement of the sun during the measurement which could probably be accounted for by a changing solar zenith angle with measurement time in the retrieval.

Beside the uncertainties discussed in the presented sensitivities studies, transmittance spectra are influenced by the water vapor concentration in the atmosphere. For the wavelengths used in the proposed retrieval, it can be shown that the transmittances change by less than 5% due to water vapor column variations (5 - 50 kgm^{-2}). Therefore, in this retrieval the water vapor influence may be neglected, but probably this is not true when exploiting the full spectral information. As well, the influence of cloud height and cloud geometrical thickness may be neglected as shown in further simulations.

In the next section the retrieval is applied to first measurements with specMACS. Two measurement examples are analyzed to learn about the retrieval performance when applied to “real” measured data.

5.2 Ground-based measurements using specMACS

In a final step, the developed retrieval is applied to first measurements with the newly established spectrometer specMACS (cf. section 3.1). A very first dataset of cirrus cloud transmission was obtained at the Meteorological Institute Munich (MIM) in June 2012 which is analyzed in section 5.2.1. During a measurement campaign at the research station “Umweltforschungsstation Schneefernerhaus” (UFS) on Mount Zugspitze in September 2012 further data were collected. One selected case from UFS is analyzed with the proposed cirrus cloud retrieval in section 5.2.2.

5.2.1 Measurements at MIM rooftop (Munich)

In this section the retrieval is applied to a measurement of cirrus cloud transmission obtained on 15th June 2012 at 14:30 UTC at the rooftop of the Meteorological Institute in Munich (geographical coordinates: 48.15° N, 11.57° E). The spectrometer is placed zenith-looking (cf. figure 3.1) and its spatial line is oriented in the principal plane implying relative azimuth angles of $\phi_{\text{rel}} = 0^\circ$ and 180° . At the beginning of the measurement, the sun position is determined to be $\theta_0 = 45.76^\circ$ and $\phi_0 = 75.03^\circ$. The sensor is operated at a frame rate of 20 Hz and an integration time of 30 ms for the VNIR and 8 ms for the SWIR camera.

The radiances measured with specMACS at a wavelength of 550 nm are shown in figure 5.11a. A row in the image corresponds to the spatial dimension of the VNIR sensor with 1312 pixel and the y-axis shows the evolution in time. The allsky image in figure 5.11b illustrates the observed scene of a thin relatively homogeneous cirrus cloud which passes over the sensor. The cloud bottom altitude is estimated to about 7.5 km a.g.l. from ceilometer data (see figure 5.12), which implies a cloud temperature of approximately -25°C . Consequently, the observed cloud is expected to consist of ice particles, but supercooled droplets could be contained as well.

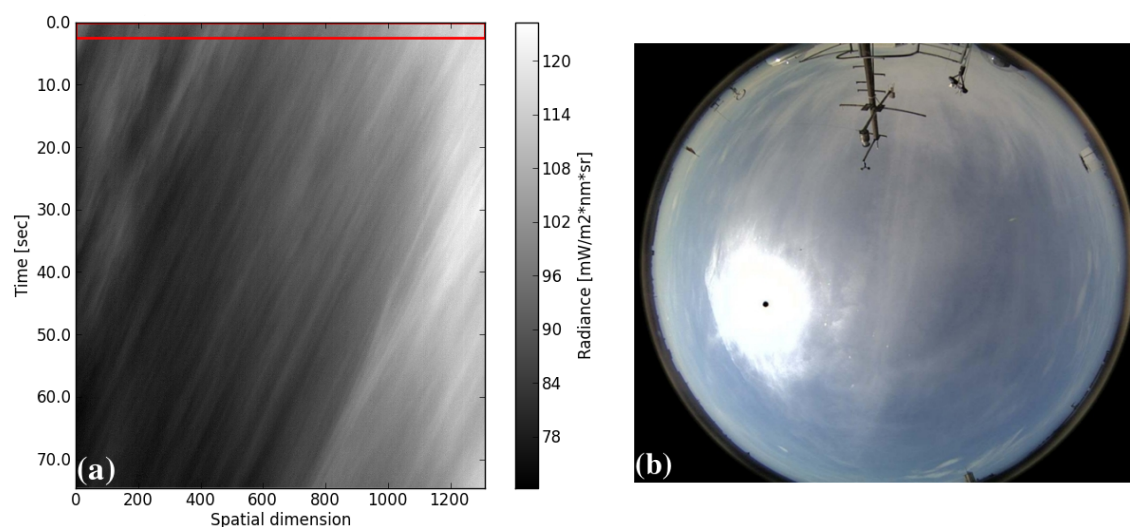


Figure 5.11: Measurement at MIM on 2012-06-15 14:30 UTC: (a) measured radiances at 550 nm for the 1312 spatial VNIR pixel of specMACS and (b) an allsky image for comparison.

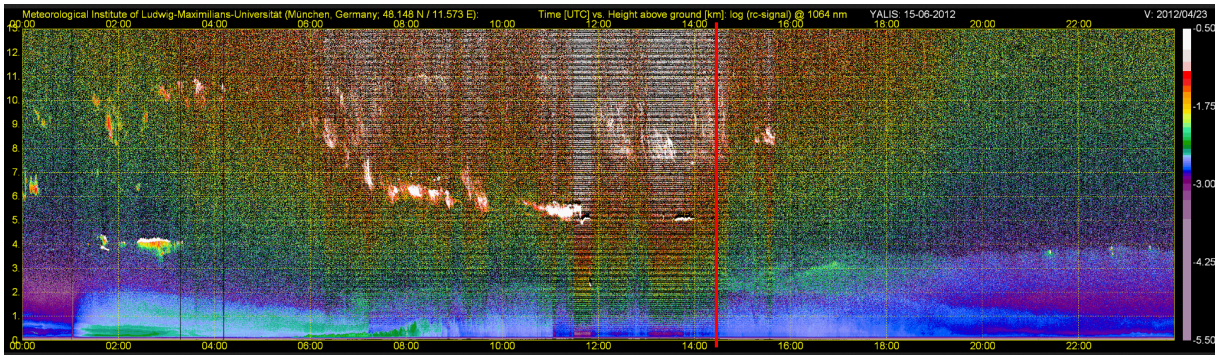


Figure 5.12: Time-height cross-section of attenuated backscatter on 2012-06-15 from ceilometer measurements at MIM. The red line indicates the specMACS measurement time. Clouds are visible as very strong white backscatter signals, height given above ground level. (courtesy of M. Wiegner)

Measured radiances are converted to transmittances according to equation 2.11 using the ex-traterrestrial solar spectrum by Kurucz interpolated to the wavelengths sampled by specMACS. As we experience issues with the calibration of specMACS data (see sec. 3.1), calibrated radiances are multiplied by a factor of $t_{\text{int,cal}}/t_{\text{int,meas}}$, which accounts for the integration time of the calibration and of the measurements. Due to the different FOV of the two cameras, the VNIR data are averaged to the number of spatial pixels of the SWIR camera and then manually aligned to provide a best possible image matching.

An exemplary spectrum, averaged over 20 spatial and 20 temporal pixels, is shown in figure 5.13a for wavelengths of 467 - 917 nm and 1296 - 2419 nm (chosen due to calibration issues, see section 3.1). Even for this limited wavelength range, an offset seems to remain between the SWIR and the VNIR part (SWIR spectrum is too high around 1300 nm). In figure 5.13b, this spectrum is qualitatively compared to simulated spectra in the lookup table for the Baum-modified mixture with several optical thickness values and $r_{\text{eff}} = 25 \mu\text{m}$.

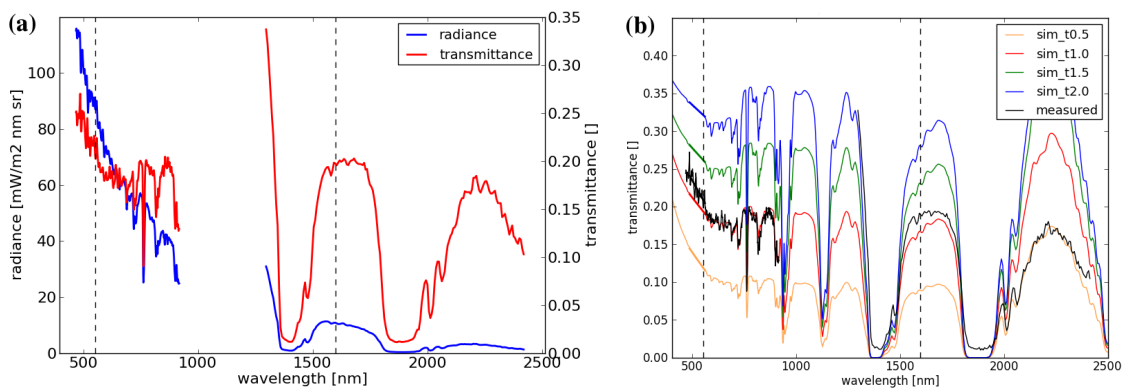


Figure 5.13: (a) Example of a calibrated radiance spectrum averaged over 20 x 20 pixel from 2012-06-15 14:30 UTC (MIM) and the corresponding spectral transmittance. (b) Comparison of this spectrum to simulations for $r_{\text{eff}} = 25 \mu\text{m}$, Baum-modified mixture, $\theta_0 = 44^\circ$, $\theta_v = 6^\circ$, and $\phi_{\text{rel}} = 0^\circ$.

This comparison shows that there are still issues in the spectral shape of measurements as no spectrum matches over the full spectral range (in this example the range 2000 - 2500 nm does not match). This could probably arise from the inaccurate calibration but also, of course, from the unknown habit mixture in the cloud and the (manually) chosen effective radius. Nevertheless, at least for the wavelengths used in the cloud retrieval (dashed black lines) there seems to be a comparable relation to the simulations.

In a very first application of the retrieval to measurements, cloud optical thickness and effective radius are retrieved for the first 50 lines of the dataset, marked as red box in figure 5.11a. The selected transmittance data are shown in figure 5.14a for a wavelength of 550 nm and in figure 5.14b for 1600 nm. The retrieval result for this dataset is illustrated in figure 5.15 assuming the Baum-modified habit mixture. The lookup table is chosen for an aerosol optical thickness of zero at 550 nm. The average AOD at 550 nm amounts to 0.1 on 15th June 2012 (Aeronet site at MIM, www.aeronet.gsfc.nasa.gov), which lies exactly inbetween the two simulated aerosol cases. As indicated in figure 5.15a, the retrieved optical thickness ranges from about 0.7 - 1.9 and resembles the features of measured transmittances at 550 nm fairly well. Figure 5.15b shows the retrieved effective radius which lies in a range from 19 μm to 52 μm , approximately.

As stated in section 5.1.3 the retrieval accuracy depends on scattering angle and is strongly decreased in the halo regions with scattering angles in the range of 17° - 27° and 42° - 50° . To interpret the retrieved values of this example with respect to this issue, data are plotted as function of scattering angle in figures 5.14 and 5.15. As can be seen in these figures the problematic scattering angle range of the 46° halo is included in the measurements, which could lead to artefacts in the retrieval over a wide range of the considered dataset. There seems to be a trend of overestimation of effective radius for scattering angles of 42° - 46° and a possible trend of underestimation for scattering angles of 46° - 49° . These trends, which are inversely and less intense visible in the optical thickness retrieval, are probably caused by the sensitivity of the halo position and magnitude to the habit mixture in the cloud. If the simulated habit mixture differs largely from the observed, especially large differences will occur in the halo region of the phasefunctions, which could lead to an offset in the interpolated lookup table compared to the measurements. Nevertheless, this example is shown to reveal the shortcomings of the retrieval method for these halo regions. Apart from these issues, the retrieved values lie in a reasonable range and reproduce the features of measured transmittances quite well.

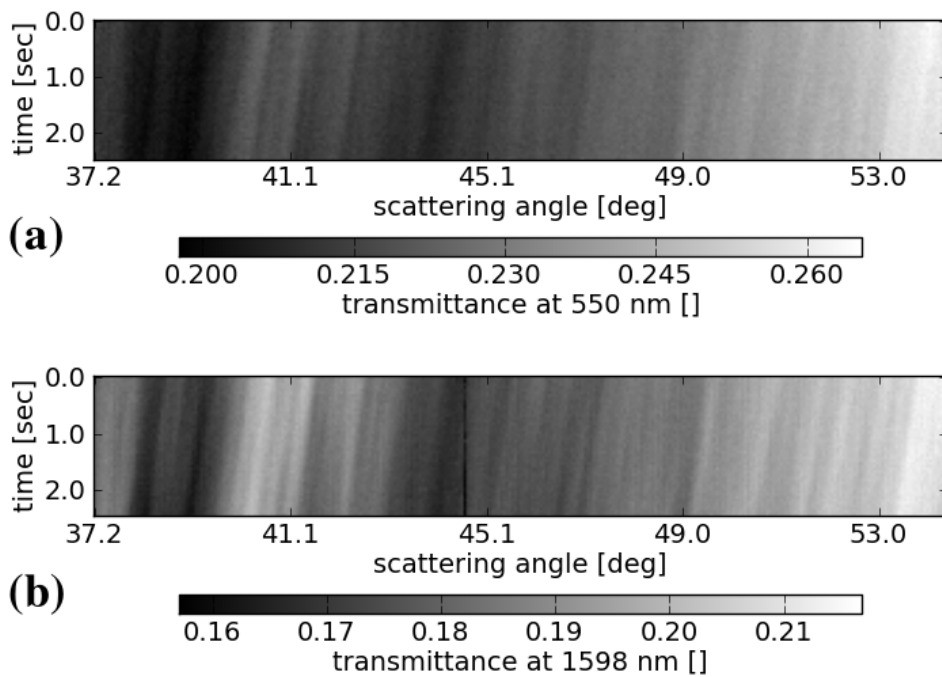


Figure 5.14: Measurement on 2012-06-15 14:30 UTC (MIM): (a) transmittance at a wavelength of 550 nm and (b) 1600 nm plotted against scattering angle (first 50 lines).

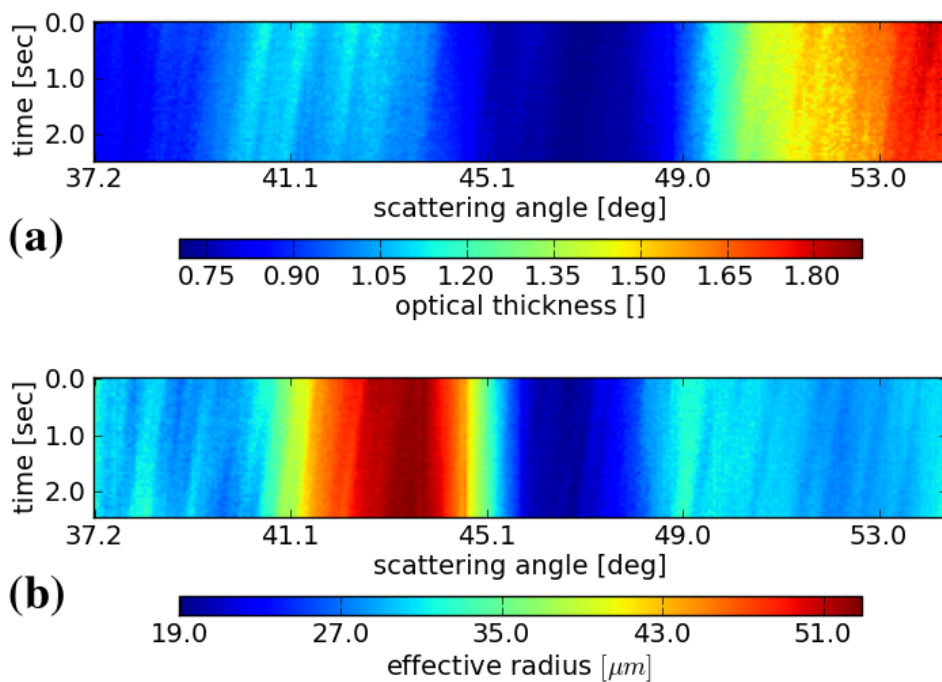


Figure 5.15: Retrieval for data from 2012-06-15 14:30 UTC (MIM): (a) retrieved optical thickness and (b) retrieved effective radius plotted against scattering angle (first 50 lines).

5.2.2 Measurements at UFS (Zugspitze)

During the measurement campaign ACRIDICON-Zugspitze (Aerosol, Cloud, Precipitation, and Radiation Interactions and Dynamics of Convective Cloud Systems) from 17th September until 5th October 2012 measurements were obtained with specMACS at the research station UFS (2650m a.s.l.), which is located close to the summit of Mount Zugspitze (geographical coordinates: 47.42° N, 10.98° E). In addition to measurements according to the actual aim of this campaign, it was possible to obtain several measurements of cirrus transmission. One example case obtained on 23rd September 14:40 UTC is chosen for analysis here.



Figure 5.16: Observed cirrus scene at UFS, 2012-09-23, 14:41:03 UTC. (courtesy of B. Reinhardt)

The observed cirrus cloud scene is illustrated in figure 5.16 which shows a camera picture taken at 14:41:03 UTC corresponding to $t = 52$ sec in the specMACS data. Beside the thin not quite homogeneous cirrus cloud an aircraft passes over the sensor inducing a fresh contrail. In figure 5.17 ceilometer data obtained at UFS are displayed to gain more information about the observed cloud conditions prevalent at the measurement time. A cloud bottom altitude of 9 - 10 km a.s.l. is estimated from the ceilometer data. This corresponds to a cloud bottom temperature of approximately -35°C (from radiosonde data, www.weather.uwyo.edu). Consequently, the observed cloud can be considered as ice cloud.

The advanced spectrometer setup used during the campaign is illustrated in figure 3.4. The sensor is zenith-looking ($\theta_v = 0.0^{\circ} \pm 8.5^{\circ}$) and its spatial line is positioned in the principal plane ($\phi_{\text{rel}} = 0^{\circ}, 180^{\circ}$) with an initial solar zenith angle of $\theta_0 = 66^{\circ}$. The integration time is set to 30 ms in the VNIR and 15 ms in the SWIR, and a frame rate of 4 Hz is chosen. The transmittances measured with specMACS are illustrated for a wavelength of 550 nm in figure 5.18a and for 1600 nm in figure 5.18b. They are calibrated and aligned with a recently set up algorithm by F. Ewald (pers. comm.) based on the calibration tool of SPECIM Ltd., Finland.

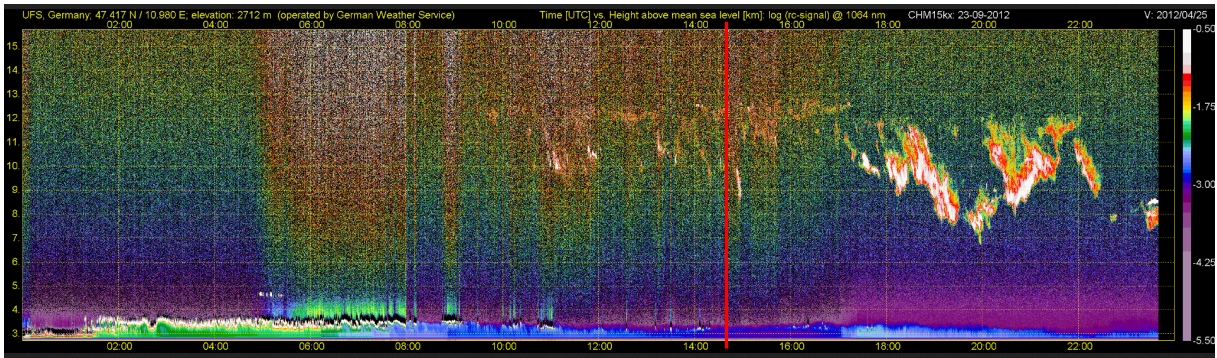


Figure 5.17: Time-height cross-section of attenuated backscatter on 2012-09-23 from ceilometer measurements at UFS. The red line indicates the specMACS measurement time. Clouds are visible as white very strong backscatter signals. Height is given above sea level. (courtesy of M. Wiegner)

In order to apply the retrieval algorithm to this dataset, a lookup table is calculated for the location of measurements and the initial solar zenith angle of 66° . In this tailored lookup table also spectra with optical thickness of 0.1 are included, as aerosol influence can be neglected at UFS and, therefore, even low cloud optical thickness is probably retrievable. As explained in equation 4.5 and 4.6, a lookuptable subset with $R_{LUT} < 0.2$ is chosen to calculate a weighted average for the retrieval of effective radius and optical thickness. In this retrieval example, a larger lookup table subset with a maximum distance of 0.3 to the measured point is considered if less than 2 points lie within a distance smaller than 0.2 in the searched lookup table. Pixels, for which even then less than 2 interpolation points would be found, are marked as invalid (white in the figure). The expansion of the lookup table subset can probably be justified due to the changing sun position during the measurement which is not accounted for in the current retrieval algorithm. Especially in the later part of the data, this leads to an increasing error in considered scattering angle and consequently to an increasing number of pixel with a lack of lookup table points for interpolation. Additionally, the habit mixture in concerned cloud pixels could deviate a lot from the assumed Baum-modified habit mixture and therefore cause the large distance of measured to simulated points. Also, there are still technical uncertainties evolving from the questionable calibration in particular for the SWIR spectrometer.

The retrieval results are presented in figure 5.19. The method for cloud phase determination (NIR-ratio) exclusively detects ice clouds in the measured scene apart from a single defective spatial pixel in the right figure part (marked in black). The retrieved optical thickness ranges from 0.1 to 4.5 as shown in figure 5.19a and the retrieved effective radius lies in a range of 5 - 55 μm as indicated in figure 5.19b. The contrail exhibits small effective radius values of about 15 μm , which agrees well with its recent development and an optical thickness larger than approximately 2.5 decreasing with time. The somewhat more opaque cirrus cloud appearing at a time of about 120 sec is characterized by an optical thickness larger than about 1.5 and effective radius values below about 20 μm . In summary, the applied retrieval produces quite reasonable values of optical thickness and effective radius. For a more precise interpretation the results have to be validated with, for example, airborne in situ measurements or satellite data which is a challenge for future work.

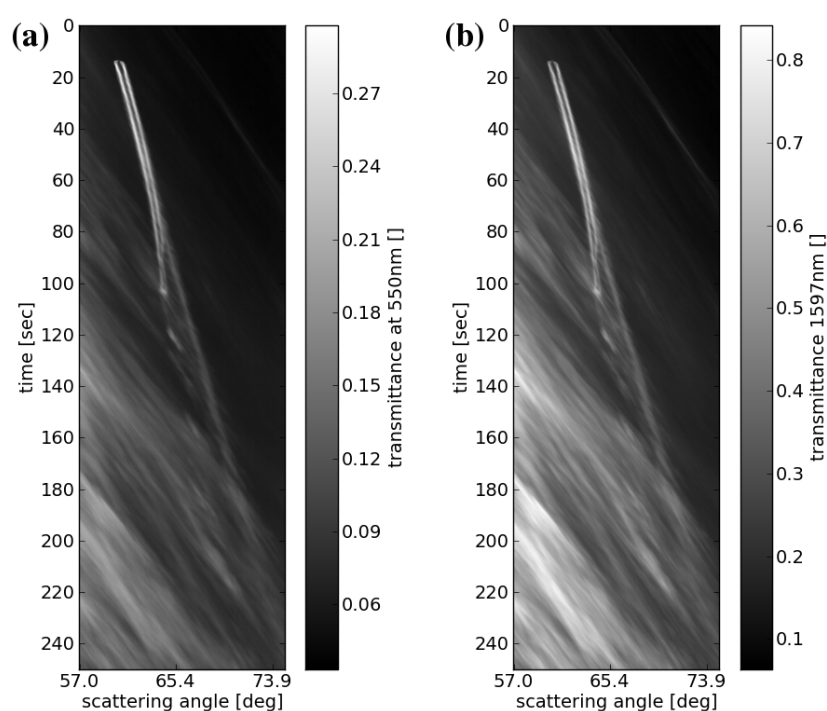


Figure 5.18: Transmittances measured with specMACS on 2012-09-23 at 14:40 UTC (UFS) for a wavelength of (a) 550 nm and (b) 1600 nm. Scattering angles are indicated at the x-axis corresponding to the spatial line of the spectrometers and the y-axis shows the development in time.

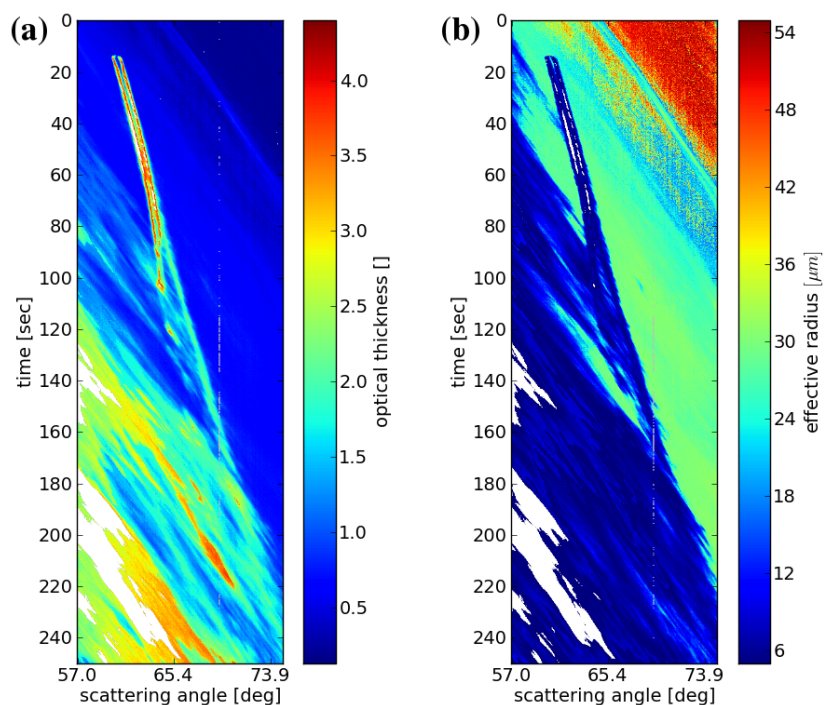


Figure 5.19: Cirrus cloud retrieval for the measurement obtained on 2012-09-23 at 14:40 UTC: (a) retrieved optical thickness and (b) retrieved effective radius (invalid pixel marked white and water phase pixel black).

Chapter 6

Discussion and outlook

Within the scope of this thesis, cirrus cloud transmittance was investigated and measured with the newly established hyperspectral imaging spectrometer specMACS. In this context, a method was developed to retrieve cloud properties, i.e. effective radius and optical thickness, of optically thin cirrus clouds from these ground-based measurements.

The applied spectrometer specMACS - part of the Munich Aerosol and Cloud Scanner - covers a continuous spectral range from 400 nm to 2500 nm in the combination of two sensors in the VNIR and SWIR spectral range. Each spectrometer contains a two-dimensional detector array with a spectral and a spatial dimension. The joint field of view of specMACS amounts to 18°. For this study the ground-based sensors were directed to the zenith with the spatial line along the principal plane. The first measurements with specMACS, presented in this study, were taken at the rooftop of the Meteorological Institute Munich and at the research station UFS at Mount Zugspitze during a measurement campaign in autumn 2012.

In order to evaluate the characteristics of ice cloud transmittance and to simulate specMACS measurements, extensive radiative transfer simulations were conducted with the radiative transfer library libRadtran (Mayer and Kylling, 2005). The radiative transfer equation was solved under the assumption of plane-parallel 1D radiative transfer applying a discrete ordinate solver. To simulate accurate transmittance spectra, a spectral albedo for each of the two measurement sites had to be taken into account, which was obtained by interpolation of the MODIS white sky albedo product using the ASTER spectral library.

The proposed retrieval is based on the approach by Nakajima and King (1990) to retrieve cloud properties from spaceborne reflectance measurements. This approach was adapted to ground-based remote sensing of cirrus cloud transmittances, which is complicated mainly due to the low optical thickness of ice clouds (usually smaller than 5) and the nonspherical, highly variable shape of ice cloud particles. In the retrieval a typical ice crystal habit mixture is assumed, based on the habit mixture by Baum et al. (2005a). The developed retrieval relies on a 3D lookup table composed of the transmittances at a visible (550 nm) and a shortwave infrared wavelength (1600 nm) as well as the spectral slope in the range 485 - 560 nm. This third dimension becomes necessary as the classic 2D Nakajima-King-like diagram shows wide ambiguous parts when applied to transmittance measurements. This ambiguity can be resolved

by using the information on optical thickness inherent to the visible spectral slope, which is associated to cloud color (high fraction of blue for optically thin clouds). The cloud phase is determined by the NIR-ratio method adapted from Martins et al. (2011), which exploits the difference in absorption of liquid and solid phase clouds observable in the ratio of transmittances at two shortwave infrared wavelengths.

In several sensitivity studies, the developed retrieval was applied to synthetic observations in order to reveal the inherent uncertainties. At first, uncertainties caused by the applied interpolation techniques were studied, both for the interpolation of optical thickness and effective radius within a lookup table and for the interpolation between lookup tables of different scattering angles. The involved uncertainties are quantified by applying the retrieval to about 30000 test cases with randomly chosen effective radius and optical thickness (within the lookup table value range), simulated for several solar zenith angles (25° - 57°), different possible viewing zenith angles, and two relative azimuth angles. The Baum-modified habit mixture is assumed in the simulations as well as in the retrieval. The test results show a bias of 0.05 and a root mean square error (RMSE) of 0.81 in the optical thickness retrieval and a bias of $-0.14 \mu\text{m}$ and a RMSE of $7.99 \mu\text{m}$ in the effective radius retrieval. While the bias values are negligible, the RMSE values are of the order of the lookup table resolution in r_{eff} and τ . The retrieval errors are above average for scattering angles close to the halo feature in the phase function (17° - 27° , 42° - 50°), which therefore should be excluded from possible applications.

Secondly, a large uncertainty is introduced into the retrieval due to the assumption of a specific ice particle habit mixture. In order to estimate this uncertainty, the retrieval was applied to the same test cases as mentioned above, but now they were simulated for each of the HEY parameterization habits (solid and hollow column, six-branch rosette, plate, droxtal, and roughened aggregate). This test reveals the maximum involved error due to the assumption of the Baum-modified habit mixture (additional to the interpolation errors above). The results for the optical thickness retrieval show a bias in the range of 0.2 - 1.6 and a RMSE of 1.8 - 3.9. For the effective radius retrieval, the bias ranges from $-10.0 \mu\text{m}$ to $-0.1 \mu\text{m}$ and the RMSE is in the range of 14 - 25 μm . Comparing these numbers to the ones for the interpolation error shown above emphasises the large additional uncertainty introduced by a “wrong” habit assumption. In a real cirrus cloud, hardly anytime a single habit will be present, which will most likely diminish the bias and probably lead to uncertainties comparable to the ones caused by the interpolation.

Thirdly, the sensitivity to aerosol introduces an uncertainty, which is significant, but smaller than the habit assumption uncertainty. Further minor uncertainties to be considered are caused by the instrument noise and the relative viewing angle determination.

In a next step, the proposed retrieval was applied to two measurements with specMACS, obtained at the Meteorological Institute in Munich and at the research station UFS on Mount Zugspitze. In the latter example, quite reasonable values of optical thickness (0.2 to 4.5) and effective radius (5 - 55 μm) were derived. In the former example, issues occurred for scattering angles in the halo region, as expected given the test results above. Generally, the retrieval results are smooth and reproduce measured transmittance features accurately.

To summarize, a method was developed to retrieve ice cloud effective radius and optical thickness from ground-based measurements with the spectrometer specMACS. It can be applied to optically thin clouds ($\tau = 0.2$ - 20) with effective particle size r_{eff} of 5 - 90 μm for scattering

angles of approximately $27^\circ < \Theta_{sca} < 42^\circ$ and $50^\circ < \Theta_{sca} < 75^\circ$ (excluding forward scattering peak and halo regions). The introduced method assumes a habit mixture derived from in-situ data as a realistic guess for the composition of ice particle shape. The ambiguity in the relation of optical thickness and transmittance was resolved by including the spectral slope in the visible spectral range in the retrieval method. Compared to McBride et al. (2011), lower optical thickness values can be derived with the method developed in this study, but a large error is introduced by the unknown ice particle shape in contrast to water clouds.

To improve the performance of the proposed retrieval, further investigation of the following issues would be necessary. The technique to obtain an interpolated lookup table for a certain solar and viewing geometry seems to produce smooth retrieval results if the two next θ_0 and four next θ_v are selected for interpolation. This could be analyzed in more detail, in order to improve interpolation accuracy and efficiency. Another topic would be the interpolation within a lookup table (weighted average), which is probably biased to regions of higher point density in the lookup table. To this end, the fixed threshold distance used to choose a subset of close points in the lookup table could be revisited. This implies re-considering the lookup table resolution in optical thickness and effective radius, in order to get more equally distributed points. Alternatively, the inhomogeneous distribution of lookup table points could be accounted for using density-adjusted weights in the weighted average. The minimum optical thickness, which can be retrieved applying the current lookup table, is confined to 0.2. It should be possible to extend the retrieval to even lower values of optical thickness with an extended lookup table, but the sensitivity to aerosol would grow significantly. Furthermore, uncertainties due to instrument noise could be diminished by considering an average over a small spatial area or a small range of wavelengths in the retrieval instead of single wavelength bands. As a basis for a correct retrieval, further efforts are currently made to provide an accurate calibration for specMACS.

Further measurements have to be analyzed to gain more detailed information about the retrieval quality, especially measurements from the field campaign at Mount Zugspitze. In addition, a method has to be found to validate the retrieval results. A possible validation method could be the intercomparison of the retrieval results with satellite retrievals, such as the newly developed cirrus cloud retrieval COCS (Kox et al., 2012, in preparation). COCS provides cirrus cloud top altitude and optical thickness in the range 0.01 - 3 for SEVIRI (MSG) images taken every 15 minutes with a spatial resolution of $3 \times 3 \text{ km}^2$ for the nadir pixel. Additional information for consistency checks can be provided by ground-based lidar and radar data obtained at UFS during the measurement campaign. Another possibility for validation is the comparison to airborne in-situ measurements with the research aircrafts Falcon or HALO (DLR).

A future exploitation of the full hyperspectral information content of specMACS measurements will possibly allow for the retrieval of ice crystal shape, which would eliminate a predominant source of uncertainty in the retrieval. To analyze the full spectral information, spectral matching methods could be applied such as proposed by Hirsch et al. (2012) for thin water clouds. In a PhD project starting in 2013, potential methods will be investigated to derive the ice particle habit and orientation from ground-based spectrometer, radar, and lidar observations. Information about particle habit would be extremely valuable for improving ice cloud remote sensing and for a better understanding of the radiative impact of ice clouds in the climate system.

Bibliography

- Aikio, M.: Hyperspectral prism-grating-prism imaging spectrograph, Technical Research Centre of Finland Heinola, Finland, 2001.
- Albrecht, B.: Aerosols, cloud microphysics, and fractional cloudiness., *Science* (New York, NY), 245, 1227, 1989.
- Anderson, G., Clough, S., Kneizys, F., Chetwynd, J., and Shettle, E.: AFGL atmospheric constituent profiles (0-120km), Hanscom AFB, MA: Optical Physics Division, Air Force Geophysics Laboratory,[1986]. AFGL-TR; 86-0110. US Air Force Geophysics Laboratory. Optical Physics Division., 1, 1986.
- Andrews, D.: An introduction to atmospheric physics, Cambridge University Press, 2010.
- Bailey, M. and Hallett, J.: Growth rates and habits of ice crystals between -20° and -70°C , *J. Atmos. Sci.*, 61, 514–544, 2004.
- Baldrige, A., Hook, S., Grove, C., and Rivera, G.: The ASTER spectral library version 2.0, *Remote Sensing of Environment*, 113, 711 – 715, 2009.
- Baran, A. J.: From the single-scattering properties of ice crystals to climate prediction: A way forward, *Atmospheric Research*, 112, 45 – 69, 2012.
- Barnard, J., Long, C., Kassianov, E., McFarlane, S., Comstock, J., Freer, M., and McFarquhar, G.: Development and evaluation of a simple algorithm to find cloud optical depth with emphasis on thin ice clouds, *The Open Atmospheric Science Journal*, 2, 46–55, 2008.
- Baum, B., Heymsfield, A., Yang, P., and Bedka, S.: Bulk scattering properties for the remote sensing of ice clouds. Part I: Microphysical data and models, *J. of Applied Meteorology*, 44, 1885–1895, 2005a.
- Baum, B., Yang, P., Heymsfield, A., Platnick, S., King, M., Hu, Y., and Bedka, S.: Bulk scattering properties for the remote sensing of ice clouds. Part II: Narrowband models, *J. of Applied Meteorology*, 44, 1896–1911, 2005b.
- Bohren, C. and Clothiaux, E.: Fundamentals of atmospheric radiation, Wiley-VCH, 2006.
- Broadley, S. L., Murray, B. J., Herbert, R. J., Atkinson, J. D., Dobbie, S., Malkin, T. L., Condliffe, E., and Neve, L.: Immersion mode heterogeneous ice nucleation by an illite rich

- powder representative of atmospheric mineral dust, *Atmospheric Chemistry and Physics*, 12, 287–307, 2012.
- Bugliaro, L., Mannstein, H., and Kox, S.: Ice Cloud Properties From Space, in: *Atmospheric Physics*, edited by Schumann, U., *Research Topics in Aerospace*, pp. 417–432, Springer Berlin Heidelberg, 2012.
- Buras, R., Dowling, T., and Emde, C.: New secondary-scattering correction in DISORT with increased efficiency for forward scattering, *Journal of Quantitative Spectroscopy and Radiative Transfer*, 112, 2028–2034, 2011.
- Burkhardt, U. and Kärcher, B.: Global radiative forcing from contrail cirrus, *Nature Climate Change*, 1, 54–58, 2011.
- Cantrell, W. and Heymsfield, A.: Production of ice in tropospheric clouds: A review, *Bulletin of the American Meteorological Society*, 86, 795–807, 2005.
- Chandrasekhar, S.: *Radiative Transfer*, Dover Books on Physics, Dover Publications, 1960.
- Comstock, J., d’Entremont, R., DeSlover, D., Mace, G., Matrosov, S., McFarlane, S., Minnis, P., Mitchell, D., Sassen, K., Shupe, M., et al.: An intercomparison of microphysical retrieval algorithms for upper-tropospheric ice clouds, *Bulletin of the American Meteorological Society*, 88, 191–204, 2007.
- DeMott, P. J., Cziczo, D. J., Prenni, A. J., Murphy, D. M., Kreidenweis, S. M., Thomson, D. S., Borys, R., and Rogers, D. C.: Measurements of the concentration and composition of nuclei for cirrus formation, *Proceedings of the National Academy of Sciences*, 100, 14 655–14 660, 2003.
- Dowling, D. R. and Radke, L. F.: A Summary of the Physical Properties of Cirrus Clouds., *J. of Applied Meteorology*, 29, 970–978, 1990.
- Ehrlich, A., Bierwirth, E., Wendisch, M., Gayet, J., Mioche, G., Lampert, A., and Heintzenberg, J.: Cloud phase identification of Arctic boundary-layer clouds from airborne spectral reflection measurements: test of three approaches, *Atmospheric Chemistry and Physics*, 8, 7493–7505, 2008.
- Eichler, H., Ehrlich, A., Wendisch, M., Mioche, G., Gayet, J.-F., Wirth, M., Emde, C., and Minikin, A.: Influence of ice crystal shape on retrieval of cirrus optical thickness and effective radius: A case study, *J. Geophys. Res.*, 114, D19 203, 2009.
- Eriksson, P., Buehler, S., Davis, C., Emde, C., and Lemke, O.: ARTS, the atmospheric radiative transfer simulator, version 2, *Journal of Quantitative Spectroscopy and Radiative Transfer*, 112, 1551–1558, 2011.
- Ewald, F., Bugliaro, L., Mannstein, H., and Mayer, B.: An improved cirrus detection algorithm MeCiDA2 for SEVIRI and its validation with MODIS, *Atmospheric Measurement Techniques Discussions*, 5, 5271–5311, 2012.

- Franklin, B.: Meteorological imaginations and conjectures, in: *Memoirs of the Literary and Philosophical Society of Manchester*, vol. 2, pp. 357–361, 1789.
- Gierens, K., Spichtinger, P., and Schumann, U.: Ice Supersaturation, in: *Atmospheric Physics*, edited by Schumann, U., *Research Topics in Aerospace*, pp. 135–150, Springer Berlin Heidelberg, 2012.
- Hansen, J. E. and Travis, L. D.: Light scattering in planetary atmospheres, *Space Science Reviews*, 16, 527–610, 1974.
- Hartmann, D., Ockert-Bell, M., and Michelsen, M.: The effect of cloud type on earth's energy balance: Global analysis, *Journal of Climate*, 5, 1992.
- Hegg, D. and Baker, M.: Nucleation in the atmosphere, *Reports on progress in Physics*, 72, 056 801, 2009.
- Hess, M., Koepke, P., and Schult, I.: Optical properties of aerosols and clouds: The software package OPAC, *Bulletin of the American meteorological society*, 79, 831–844, 1998.
- Heymsfield, A. and Iaquinta, J.: Cirrus crystal terminal velocities, *J. Atmos. Sci.*, 57, 916–938, 2000.
- Heymsfield, A. and Miloshevich, L.: Parameterizations for the cross-sectional area and extinction of cirrus and stratiform ice cloud particles, *J. Atmos. Sci.*, 60, 936–956, 2003.
- Heymsfield, A., Bansemer, A., Field, P., Durden, S., Stith, J., Dye, J., Hall, W., and Grainger, C.: Observations and parameterizations of particle size distributions in deep tropical cirrus and stratiform precipitating clouds: Results from in situ observations in TRMM field campaigns, *J. Atmos. Sci.*, 59, 3457–3491, 2002.
- Heymsfield, A. J. and Platt, C. M. R.: A Parameterization of the Particle Size Spectrum of Ice Clouds in Terms of the Ambient Temperature and the Ice Water Content., *J. Atmos. Sci.*, 41, 846–855, 1984.
- Hirsch, E., Agassi, E., and Koren, I.: Determination of optical and microphysical properties of thin warm clouds using ground based hyper-spectral analysis, *Atmos. Meas. Tech.*, 5, 851–871, 2012.
- IPCC: *Climate Change 2007: The Physical Science Basis. Contribution of Working Group I to the Fourth Assessment Report of the Intergovernmental Panel on Climate Change* [Solomon, S., Qin, D., Manning, M., Chen, Z., Marquis, M., Averyt, K.B., Tignor, M., and Miller H.L. (eds.)], Cambridge University Press, Cambridge, United Kingdom and New York, NY, USA, 2007.
- Kärcher, B.: Atmospheric Ice Formation Processes, in: *Atmospheric Physics*, edited by Schumann, U., *Research Topics in Aerospace*, pp. 151–167, Springer Berlin Heidelberg, 2012.
- Key, J., Yang, P., Baum, B., and Nasiri, S.: Parameterization of shortwave ice cloud optical properties for various particle habits, *J. Geophys. Res.*, 107, 2002.

- King, M., Platnick, S., Yang, P., Arnold, G., Gray, M., Riedi, J., Ackerman, S., and Liou, K.: Remote sensing of liquid water and ice cloud optical thickness and effective radius in the Arctic: Application of airborne multispectral MAS data, *Journal of Atmospheric and Oceanic Technology*, 21, 857–875, 2004.
- Kokhanovsky, A.: Optical properties of terrestrial clouds, *Earth-Science Reviews*, 64, 189–241, 2004.
- Kox, S., Mannstein, M., and Bugliario, L.: A novel neural network approach for the retrieval of cirrus clouds from SEVIRI exploiting CALIOP, *Atmos. Meas. Tech.*, 2012, in preparation.
- Krebs, W., Mannstein, H., Bugliario, L., and Mayer, B.: Technical note: A new day-and night-time Meteosat Second Generation Cirrus Detection Algorithm MeCiDA, *Atmospheric Chemistry and Physics*, 7, 6145–6159, 2007.
- Kurucz, R.: Synthetic infrared spectra, in: *Proceedings of the 154th Symposium of the International Astronomical Union (IAU)*; Tucson, Arizona, March 2-6, 1992, Kluwer, Acad., Norwell, MA, 1992.
- Lambrechts, A., Tack, K., and Pessolano, F.: Multispectral/Hyperspectral Imaging: CMOS takes hyperspectral imaging beyond the laboratory, *Laser Focus World*, 2011.
- Libbrecht, K.: The physics of snow crystals, *Reports on Progress in Physics*, 68, 855, 2005.
- Liou, K.: Influence of cirrus clouds on weather and climate processes: A global perspective, *Monthly Weather Review*, 114, 1167–1199, 1986.
- Liou, K. and Takano, Y.: Light scattering by nonspherical particles: remote sensing and climatic implications, *Atmospheric Research*, 31, 271–298, 1994.
- Litwiller, D.: CCD vs. CMOS, *Photonics Spectra*, 35, 154–158, 2001.
- Martins, J., Marshak, A., Remer, L., Rosenfeld, D., Kaufman, Y., Fernandez-Borda, R., Koren, I., Correia, A., Zubko, V., Artaxo, P., et al.: Remote sensing the vertical profile of cloud droplet effective radius, thermodynamic phase, and temperature, *Atmospheric Chemistry and Physics*, 11, 9485–9501, 2011.
- Maxwell, J.: A dynamical theory of the electromagnetic field, *Philosophical Transactions of the Royal Society of London*, 155, 459–512, 1865.
- Mayer, B.: Radiative transfer in the cloudy atmosphere, *European Physical Journal Conferences*, 1, 75–99, 2009.
- Mayer, B. and Kylling, A.: Technical note: The libRadtran software package for radiative transfer calculations - description and examples of use, *Atmospheric Chemistry and Physics*, 5, 1855–1877, 2005.
- Mayer, B., Kylling, A., Emde, C., Hamann, U., and Buras, R.: *libRadtran user's guide*, 2012.

- McBride, P. J., Schmidt, K. S., Pilewskie, P., Kittelman, A. S., and Wolfe, D. E.: A spectral method for retrieving cloud optical thickness and effective radius from surface-based transmittance measurements, *Atmospheric Chemistry and Physics*, 11, 7235–7252, 2011.
- McBride, P. J., Schmidt, K. S., Pilewskie, P., Walther, A., Heidinger, A., Wolfe, D., Fairall, C., and Lance, S.: CalNex cloud properties retrieved from a ship-based spectrometer and comparisons with satellite and aircraft retrieved cloud properties, *J. Geophys. Res.*, 117, D00V23, 2012.
- McFarquhar, M., G., and Heymsfield, A. J.: The Definition and Significance of an Effective Radius for Ice Clouds, *J. Atmos. Sci.*, 55, 2039–2052, 1998.
- Mie, G.: Beiträge zur Optik trüber Medien, speziell kolloidaler Metallösungen, *Annalen der Physik*, 330, 377–445, 1908.
- Mishchenko, M., Hovenier, J., and Travis, L.: Light scattering by nonspherical particles: theory, measurements, and applications, Academic Press, 1999.
- Nakajima, T. and King, M.: Determination of the optical thickness and effective particle radius of clouds from reflected solar radiation measurements. Part I: Theory, *J. Atmos. Sci.*, 47, 1878–1893, 1990.
- Petty, G.: A first course in atmospheric radiation, Sundog Publishing, 2006.
- Pierluissi, J. and Peng, G.: New molecular transmission band models for LOWTRAN, *Optical Engineering*, 24, 541–547, 1985.
- Pilewskie, P., Pommier, J., Bergstrom, R., Gore, W., Howard, S., Rabbette, M., Schmid, B., Hobbs, P., and Tsay, S.: Solar spectral radiative forcing during the southern African regional science initiative, *J. Geophys. Res.*, 108, 8486, 2003.
- Pruppacher, H. and Klett, J.: Microphysics of clouds and precipitation, Atmospheric and oceanographic sciences library, Vol. 18, Kluwer Academic Publishers, 1997.
- Rayleigh, L.: On the transmission of light through an atmosphere containing small particles in suspension, and on the origin of the blue of the sky, *Philosophical Magazine Series 5*, 47, 375–384, 1899.
- Ricchiazzi, P., Yang, S., Gautier, C., and Sowle, D.: SBDART: A research and teaching software tool for plane-parallel radiative transfer in the Earth's atmosphere, *Bulletin of the American Meteorological Society*, 79, 2101–2114, 1998.
- Rogers, R. and Yau, M.: A short course in cloud physics, International series in natural philosophy, Pergamon Press, 1989.
- Sassen, K., O’C Starr, D., and Uttal, T.: Mesoscale and microscale structure of cirrus clouds: Three case studies., *J. Atmos. Sci.*, 46, 371–396, 1989.

- Sassen, K., Wang, Z., and Liu, D.: Global distribution of cirrus clouds from CloudSat/Cloud-Aerosol lidar and infrared pathfinder satellite observations (CALIPSO) measurements, *J. Geophys. Res.*, 113, 2008.
- Schumann, U.: Formation, properties and climatic effects of contrails, *Comptes Rendus Physique*, 6, 549–565, 2005.
- Schumann, U., Mayer, B., Gierens, K., Unterstrasser, S., Jessberger, P., Petzold, A., Voigt, C., and Gayet, J.-F.: Effective Radius of Ice Particles in Cirrus and Contrails, *J. Atmos. Sci.*, 68, 300–321, 2011.
- Stamnes, K., Tsay, S.-C., Wiscombe, W., and Jayaweera, K.: Numerically stable algorithm for discrete-ordinate-method radiative transfer in multiple scattering and emitting layered media, *Appl. Opt.*, 27, 2502–2509, 1988.
- Stamnes, K., S.-C.Tsay, Wiscombe, W., and Laszlo, I.: DISORT, a General-Purpose Fortran Program for Discrete-Ordinate-Method Radiative Transfer in Scattering and Emitting Layered Media: Documentation of Methodology, Tech. rep., Dept. of Physics and Engineering Physics, Stevens Institute of Technology, Hoboken, NJ 07030, 2000.
- Stephens, G. L., Tsay, S.-C., Stackhouse, Jr., P. W., and Flatau, P. J.: The Relevance of the Microphysical and Radiative Properties of Cirrus Clouds to Climate and Climatic Feedback., *J. Atmos. Sci.*, 47, 1742–1754, 1990.
- Strahler, A., Muller, J., Lucht, W., Schaaf, C., Tsang, T., Gao, F., Li, X., Lewis, P., and Barnsley, M.: MODIS BRDF/albedo product: algorithm theoretical basis document version 5.0, MODIS documentation, 1999.
- Szyrmer, W., Tatarevic, A., and Kollias, P.: Ice clouds microphysical retrieval using 94-GHz Doppler radar observations: Basic relations within the retrieval framework, *J. Geophys. Res.*, 117, D14 203, 2012.
- Thomas, G. and Stamnes, K.: Radiative transfer in the atmosphere and ocean, Cambridge University Press, 2002.
- Twomey, S.: The influence of pollution on the shortwave albedo of clouds, *J. Atmos. Sci.*, 34, 1149–1152, 1977.
- Wallace, J. and Hobbs, P.: Atmospheric Science, Elsevier, 2006.
- Wang, Zhien, K. S.: Cirrus cloud microphysical property retrieval using lidar and radar measurements. part i: algorithm description and comparison with in situ data, *J. of Applied Meteorology*, 41, 218–229, 2002.
- Wiscombe, W.: Improved Mie scattering algorithms, *Appl. Opt.*, 19, 1505–1509, 1980.
- Wylie, D., Menzel, W., Woolf, H., and Strabala, K.: Four Years of Global Cirrus Cloud Statistics Using HIRS., *Journal of Climate*, 7, 1972–1986, 1994.
- Wyser, K.: The effective radius in ice clouds, *Journal of climate*, 11, 1793–1802, 1998.

- Yang, P. and Liou, K. N.: Finite-difference time domain method for light scattering by small ice crystals in three-dimensional space, *J. Opt. Soc. Am. A*, 13, 2072–2085, 1996a.
- Yang, P. and Liou, K. N.: Geometric-optics—integral-equation method for light scattering by nonspherical ice crystals, *Appl. Opt.*, 35, 6568–6584, 1996b.
- Yang, P., Liou, K., Wyser, K., and Mitchell, D.: Parameterization of the scattering and absorption properties of individual ice crystals, *J. Geophys. Res.*, 105, 4699–4718, 2000.
- Yang, P., Wei, H., Huang, H., Baum, B., Hu, Y., Kattawar, G., Mishchenko, M., and Fu, Q.: Scattering and absorption property database for nonspherical ice particles in the near-through far-infrared spectral region, *Appl. Opt.*, 44, 5512–5523, 2005.
- Zdunkowski, W., Trautmann, T., and Bott, A.: *Radiation in the Atmosphere: A Course in Theoretical Meteorology*, Cambridge University Press, 2007.
- Zinner, T., Marshak, A., Lang, S., Martins, J., and Mayer, B.: Remote sensing of cloud sides of deep convection: towards a three-dimensional retrieval of cloud particle size profiles, *Atmospheric Chemistry and Physics*, 8, 4741–4757, 2008.

Acknowledgements

Above all, I would like to thank my supervisors Dr. Tobias Zinner and Prof. Dr. Bernhard Mayer for providing the opportunity to accomplish this master thesis in such an inspiring research group. I am especially grateful to Tobias Zinner for his encouraging support and for all the valuable discussions over the entire course of this work. In particular, I would like to express my gratitude to Prof. Dr. Bernhard Mayer for his helpful suggestions and supportive advice in many questions during the last year.

Furthermore, I would like to thank Florian Ewald for his tireless work in establishing the spectrometer specMACS, for his cooperativeness, and for many fruitful discussions. Many thanks to Dr. Claudia Emde for providing an ice particle habit parameterization and giving active support in its application. I would also like to thank Bernhard Reinhardt for supplying his habit mixture parameterization and for the helpful discussions. Additionally, thanks to Linda Forster for many good conversations and an enjoyable working atmosphere.

Many thanks to all my friends who have supported me during the last year (and distracted me from work from time to time). Especially, I want to thank Frank for his patient listening and understanding. Finally, I am particularly grateful to my mother for her tireless encouragement and support in any occurring problem.

Declaration by candidate

I hereby declare that this thesis is my own work and effort and that it has not been submitted anywhere for any award. Where other sources of information have been used, they have been acknowledged.

Munich, December 5, 2012

Petra Hausmann